Tracing the Interstellar Medium using extinction and polarisation

Eirik Bratli

Thesis submitted for the degree of
Master in Master of Science in Astronomy
60 credits

Institute of Theoretical Astrophysics
Faculty of Mathematics and Natural Science

UNIVERSITY OF OSLO

Spring 2020

Tracing the Interstellar Medium using extinction and polarisation

Eirik Bratli

Tracing the Interstellar Medium using extinction and polarisation

http://www.duo.uio.no/

Printed: Reprosentralen, University of Oslo

Abstract

Cosmologists are now searching for the elusive B-mode Cosmic Microwave Background (CMB) polarisation signature, which theory states should come from primordial gravitational waves during inflation. The CMB entanglement with the galactic foreground emission increases the complexity of finding primordial B-modes. The removal of polarised foreground emission is one of the critical factors to achieve B-mode detection from gravitational waves. The physical nature of the galactic dust emission is essential to understand for the component separation of different signals to be accurate. Thermal dust emission is relevant to other fields in astronomy by extracting information about the grain composition, alignment with the galactic magnetic field, shape of the dust grains and the strength of the interstellar radiation field. Both extinction and polarisation of starlight combined with polarised thermal dust emission provide vital insight into the properties of galactic emission.

In this thesis, we are investigating the 3D dust distribution in the Milky Way using extinction estimates from Gaia Data Release 2 and Green et al. (2019). We calculate ten cumulative differential extinction maps from 0 to 3000 pc. We combine visual starlight polarisation (p_v, q_v, u_v) from RoboPol with submillimeter polarisation intensity (P_s, Q_s, U_s) from the 353 GHz band of Planck looking at correlation between submillimeter and visual polarisation. Further, we calculate the difference in polarisation angle, $\Delta\psi_{s/v}$, and the ratio, $R_{P/p}$, between submillimeter and visual polarisation. Then we use this knowledge to estimate the spectral index for thermal dust emission, β_d.

The extinction maps show structural differences over distance at all sightlines. We show there is not a linear correlation between extinction and dust and CO line emission. We calculate $R_{P/p} = 4.47 \pm 0.82$ MJy/sr, and the joint Pearson correlation coefficient between Q_s, U_s and q_v, u_v: $R = -0.963$ giving a best fit slope of $Q_s U_s$ versus $q_v u_v$ is -4.535 ± 0.444 MJy/sr. We found the spectral index to be 1.56 ± 0.01.

Acknowledgements

In this work, I will thank my girlfriend and family for always supporting me to achieve my goals and go for my dreams. The universe has always fascinated me, and I am humbled to finish a master degree in the field. The task of finishing my thesis would be much harder without them, especially considering the pandemic. Further, I will thank my supervisors Hans Kristian, Ingunn and Eirik for great help and an inspiring, fun, fascinating and frustrating thesis, and not destroying my interest in astronomy.

Second, a great thanks to the students at the Stellarcellar and Lillefy for making the student life easier and funnier, and especially Metin, for helpful discussions and just being there throughout the bachelor and master. Good co-students and friends are vital to get through the toughest courses and problems the professors throw at you from all directions.

Last, I will thank Gina Panopoulou for making my stay at Caltech fantastic, and the rest for the Pasiphae team for dedicating their time into my thesis. Having a thesis with results significant to professional scientists is motivating.

Preamble

From observations of microwave radiation of the entire sky, the Planck satellite has given cosmologists and astrophysicists vital knowledge of the Cosmic Microwave Background (CMB) radiation anisotropies and information of the early universe. Since the Planck detectors cover a wide range of frequencies, the data it provides also contain information about the conditions in the Milky Way both in intensity and polarisation. Several studies of the sky in the optical regime, like the Gaia satellite and ground-based telescopes, contain supplementary information of the conditions in the Milky Way, both on the emission of radiation and the polarisation. The polarisation of CMB can reveal information of the earliest moments of the universe but is hard to determine. The amplitude of the temperature fluctuation of the CMB is in the order of 10^{-5} K, while to get the full polarisation signal of CMB, measurements down to $< 10^{-9}$ K is needed.

To distinguish emission sources from each other is of great importance to get an accurate view of the CMB and extragalactic sources. Emission from the interstellar medium (ISM) is a large part of the data Planck has produced. In the high-frequency bands of Planck, the primary source of radiation comes from stars heating the dust particles, which re-emits thermal radiation. Even though thermal radiation from dust particles can describe the emission phenomenologically, it is challenging to reproduce the data by physically motivated models.

To understand the physics of the ISM is of great importance to improve the dust models. The properties of the ISM can inform astrophysicists about dust-formation in our galaxy, star formation and the strength of starlight. The dust grains in the ISM absorbs starlight in optical and ultraviolet frequencies and re-emits radiation in lower frequencies, like infrared, this process reddens the light. Observations of vast amounts of stars in the galaxy, at different frequencies, make scientists able to map the reddening of starlight and to trace the ISM structures. The dust grains can also polarise the starlight, because of asymmetric shape and alignment with the magnetic field of the Milky Way. By mapping the polarisation caused by the ISM, the magnetic field of the Milky Way can be traced, and improve the separation between CMB and dust emission.

In this thesis, we investigate starlight absorption in the ISM by tracing the extinction of starlight in 3D using the latest data release of the Gaia satellite and compare the extinction with emission from thermal dust and CO line intensity. From a pedagogical perspective, we create a Gibbs

sampler to learn more about how the intensity spectrum of thermal dust and synchrotron radiation affects the observed signal in the microwave sky using observation data of Planck. In the last part, we compare polarisation of starlight with CMB polarisation using stellar observation provided by RoboPol and look for correlations and what these means. From the correlation, we create a template converting starlight polarisation to polarisation similar to polarised thermal emission, which we use to estimate the spectral index in thermal dust models.

Contents

PART I

Introduction and Theory to the cosmos

Chapter 1

Cosmological History and properties of the Interstellar Medium

Through the history of humankind, people have gazed up at the night sky in wonder of those small bright stars and our place in the universe. With the creation of the telescope, humans could peer into the vast void of space and explore our neighbouring planets and later further out in the cosmos. The technological development over the last 400 years have been outstanding, bringing new knowledge every day to the curious mind. In this thesis, we will look into some of the properties the universe offer and explore them in more detail. This chapter brings a brief introduction of the history of the universe, the modern cosmological theory, and properties of the Interstellar Medium (ISM) affecting signals from cosmological sources and stars. The cosmological background sections are written by the help of Scott Dodelsons book "Modern Cosmology" (2003) and other sources where needed.

1.1 Cosmological History

In the early 20th century many scientists thought the universe was static, neither expanding nor contracting. However, some argued the universe could also evolve, like for example, George Lemaître. He theoretically discovered that an expanding universe could grow from a single point and gave rise to the Big Bang theory. The Big Bang theory states a primordial universe being infinitely dense, before starting to expand into the universe we see today. If a super-dense and super-hot point expands into a volume, the temperature within the expanding volume will decrease (Peebles et al. 1994). Let us call the volume for a universe from now. For a homogeneous and isotropic universe, i.e., a universe in which the cosmological principle[1]

[1]The cosmological principle states the universe to be homogeneous and isotropic. Such that an observer, regardless of the observation point, sees the universe as the same in every

is valid, the expected temperature is equal at every point in space. About 100 years ago, Edwin Hubble observed distant galaxies moving away from each other and us. By his observations, Hubble concluded the universe was expanding and for that reason must come from something smaller, strengthening the Big Bang theory. The discovery of the cosmic microwave background radiation (CMB) in 1964 gave evidence for the Big Bang model. The CMB is the first light in the universe coming from when free electrons decoupled from photons and bound with atomic nuclei (Dodelson, 2003), and supports the cosmological principle with the temperature of the CMB being equal all over within the range of $\mathcal{O}(10^{-5})$.

To go further into the evolution of such a universe, we can divide it into epochs. There has to be a short epoch at primordial times with an extreme expansion to describe the universe seen today, and this is the inflation. The Big Bang model induce some problems, for example, the horizon problem, that is solved by an inflationary epoch. The horizon problem says that on large scales, the universe is not causally connected but in thermal equilibrium, this is a problem since we observe causally disconnected parts of the universe being in thermal equilibrium which should be impossible (Guth, 1981). Alternatively said; imagine a cone, all points inside the cone at any time is causally connected, while all points not sharing the same cone are not causally connected (Dodelson, 2003). Figure 1.1 illustrate causality, with the red arrows being in thermal equilibrium but can only exchange information if they exist inside the cone. The photons from the last scattering did not share the same cone, i.e. they have not had time to connect causally but are in thermal equilibrium (Guth, 1981). There is no known physical process that can exchange information on such scales. Inflation solves the horizon problem because the rapid expansion breaks the causality between two points in space but keeps the thermal equilibrium. Scientists assume the universe was in thermal equilibrium before inflation, which means areas once were in thermal equilibrium no longer can exchange information but evolve equally (Guth, 1981).

In the inflationary expansion, quantum fluctuation[2] happened, giving variations in the density distribution. However, the expansion smoothed the fluctuations to be small and settle in space. Today, observations of temperature fluctuations in the CMB are the remnants of the quantum fluctuations, with areas having slightly higher and lower temperature than the surroundings. Inflation set the initial conditions of the astrophysical and cosmological parameters we observe today because of the quantum fluctuations and density fluctuations (Guth, 2007). Inflation is our best explanation of the early universe since the universe we observe today is in thermal equilibrium and fulfils the cosmological principle. After inflation, the universe became less dense and cold enough for atomic nucleons to form, but still too dense and hot for electrons to bound to the nucleons and form atoms. The period of nucleon formation is the so-called Big Bang Nucleosynthesis. Furthermore, the universe continued to expand, and

direction with a homogeneous matter distribution.

[2]Quantum fluctuation are energy differences in vacuum due to the uncertainty principle.

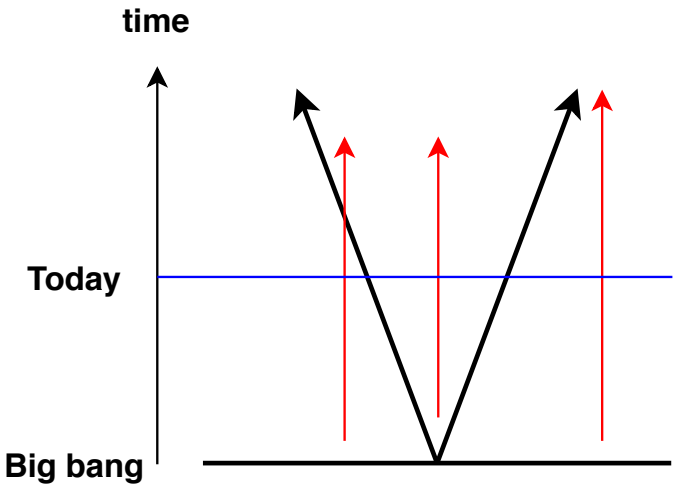

Figure 1.1: Illustration of causality. The red arrow inside the cone is only allowed to point in directions not crossing the cone boundaries. The red arrow outside have not had enough time to exchange information with the arrow in the cone, i.e. not causally connected. The red arrows are in thermal equilibrium since the same colour.

the density and the temperature decrease persist. At about 380 000 years after the Big Bang, the temperature had fallen enough for atomic nucleons and free electrons to recombine into hydrogen, helium and a small part lithium. This process stopped the Compton scattering between photons and free electrons, such that the photons could travel freely over vast distances with no interaction. These photons formed the CMB. We know this period as the recombination and sets the boundary of our observational universe since the photons from the last scattering is the CMB photons. Before recombination, the particles could not move freely for more than short distances such that the information from earlier times stops to exist. The last interaction a photon had, determines the information it carries, meaning, detection of events before recombination is today impossible, we can only predict them.

The time from the last scattering to the first stars where born is called the Dark Age. Then the universe comprise neutral hydrogen and some heavier atoms. The radiation of this era are the CMB photons from the last scattering and emission of neutral hydrogen (21 cm emission line) (Fialkov and Loeb, 2013). The gravitational pull of the massive halos of Dark Matter gathered atoms into clouds with increasing density, and this builds the foundation for stars and galaxies. Where the density becomes large enough for nuclear fusion to start, the first stars were born and began to shine in the hydrogen clouds. The light of the first stars ended the Dark Ages and started to re-ionise the surrounding hydrogen. The energetic photons

interact with neutral hydrogen, freeing electrons. During this process, the age of the universe is maximally 1 billion years after the Big Bang. The re-ionisation made the CMB photons scatter on the newly free electrons, which distort the CMB signal we observe today by an increase of the optical depth in the universe (Planck Collab. Int. XLVI, 2016). We set constraints on the initial conditions given by inflation from the observations of the CMB. The estimation of many of the initial conditions have high precision, but some remains. One of the central initial conditions still to estimate is the strength of gravitational waves from inflation. The hypothesised strength of the primordial gravitational waves imprint on the CMB is small. The optical depth to re-ionisation is another crucial parameter to constrain to high precision. Further, we will give a brief introduction of the model used to describe the universe and motivation of primordial gravitational waves and optical depth to re-ionisation.

1.1.1 Cosmological models and the Hubble parameter

Our best model for the universe today is described by General Relativity and the ΛCDM model (Planck Collab. VI, 2018). The name comes from the two main ingredients in the universe, Dark Energy and Dark Matter. The model describes an expanding universe dominated by Dark Energy, given as the Greek letter, Λ, also known as the cosmological constant, and Cold Dark Matter. Both entities are so far impossible to detect directly, only the movement and behaviour of galaxies and clusters of galaxies explains their presence. From observations of the CMB, the estimated energy content of the universe is about 69 % Dark Energy, 26 % Dark Matter, 5% regular matter and $\ll 1\%$ radiation (Planck Collab. VI, 2018). The amount of each component is crucial to the evolution of the universe and how we observe it today.

Observations show that the expansion of the universe is accelerating. When looking at how the universe expand today and to understand its history one looks to the content within. There are five main contents in the universe: dark energy (Λ), dark matter (m), baryons (b), photons (γ) and neutrinos (ν). There is a direct connection between these contents and the expansion of the universe. For a flat universe, the sum of the relative densities, Ω_x, of the listed contents are one,

$$\Omega_b + \Omega_m + \Omega_\gamma + \Omega_\nu + \Omega_\Lambda = 1. \tag{1.1}$$

All of the Ω_x are some of the astrophysical parameters initialised during inflation.

From General Relativity, the geometry of space-time depends on the energy-content within This means the expansion of the universe depends on the relative densities. The Hubble parameter, H, describes the expansion of the universe,

$$H(t) = \frac{\dot{a}(t)}{a(t)} = H_0\sqrt{(\Omega_b + \Omega_m)a(t)^{-3} + (\Omega_\gamma + \Omega_\nu)a(t)^{-4} + \Omega_\Lambda}, \tag{1.2}$$

where H_0 is the Hubble parameter today, $a(t)$ is the scale factor dependent on time and $\dot{a}(t)$ is the time derivative of a. Today the scale factor is unity and goes to zero when approaching the Big Bang. The relative densities are time-dependent, and from their dominance, scientists divide the history of the universe into epochs of radiation domination, matter domination and dark energy domination. As we know, today, the universe is dominated by dark energy, and this is the driving mechanism of the accelerating expansion of the universe. The present value, H_0, of the Hubble parameter, relates at what speed, v, does an object at a distance, d, move away from an observer, $v = H_0 d$.

There is currently a major discussion regarding the value of the Hubble parameter. The Planck Collaboration has so far the estimates with smallest uncertainties giving the value $H_0 = 67.4 \pm 0.5$ km/s/Mpc (Planck Collab. VI, 2018). Earlier similar surveys like the Wilkinson Microwave Anisotropy Probe (WMAP) find $H_0 = 69.32 \pm 0.80$ km/s/Mpc (Bennett et al. 2013). But local measurements of H_0, give different results. These types of measurements use distance ladders from standard candles, like Cepheid stars and Supernovae type 1a, to find the distance, d, needed to estimate H_0. By using Cepheid stars as distance ladder, the calculated H_0 is around 74 ± 1.4 km/s/Mpc (Dhawan et al. 2020). One similar method uses the tip of the Red Giant Branch stars instead of Cepheid stars in neighbouring galaxies to determine the distance to the objects. Using this method, Freedman et al. (2019, 2020) find $H_0 = 69.6 \pm 0.8$ ($\pm$ 1.1% stat.) $\pm$ 1.7 (2.4% sys.) km/s/Mpc and Yuan et al. (2019) find $H0 = 72.4 \pm 2.0$ km/s/Mpc. H_0 can also be estimated from gravitational lensing of Quasars, Wong et al. (2019) find $H_0 = 73.3^{+1.7}_{-1.8}$ km/s/Mpc. The different results say that either there is some unknown properties or physics of the universe not yet discovered or there are some errors in the local measurements, like for example the distance estimate.

1.1.2 Primordial gravitational waves

A precise model of the universe is important to estimate the initial conditions on cosmological parameters. From the theory of General relativity, we know the metric, $g_{\mu\nu}$, is a tensor[3]. The line element, described by the geometry of time and space, gives, $ds^2 = g_{\mu\nu} dx^\mu dx^\nu$,

$$ds^2 = dt^2 - d\mathbf{x}^2, \tag{1.3}$$

where dt and $d\mathbf{x}$ are infinitesimal changes in time and space. Perturbations are small variations in a field where the field globally is smooth, but locally the field is not smooth. Mathematically, we write perturbations of a quantity as,

$$x' = x + \delta x, \tag{1.4}$$

where x is the unperturbed quantity and δx, is the perturbation of the quantity. Including perturbation terms in the Friedmann-Lemaître-Robinson-Walker (FLRW) line element, used to deduce of the ΛCDM

[3]A tensor is a mathematical multi-linear object, and the metric describes the geometry and structure of space-time

model, predicts primordial gravitational waves, and give motivation to the study of the polarisation of the CMB (Kamionkowski and Kovetz, 2016). Expanding equation (1.4) into tensors, it reads $g'_{\mu\nu} = g_{\mu\nu} + h_{\mu\nu}$, where $g_{\mu\nu}$ is the unperturbed metric and $h_{\mu\nu}$ is the perturbation. Gravitational waves act as perturbations on the space part of $h_{\mu\nu}$. Writing the FLRW line element including spatial perturbation terms, it goes as,

$$ds^2 = a^2(\eta)[d\eta^2 - dx^2(1+h) - dy^2(1-h) + dz^2], \tag{1.5}$$

where η is the conformal time[4] and $h = h(\eta, \mathbf{x})$ is the tensor perturbation of the metric giving gravitational waves in z direction (Kamionkowski and Kovetz, 2016).

A way of probing the strength of the primordial gravitational waves is to calculate the tensor-to-scalar ratio, $r = P_T/P_R$, between the power spectra of tensor perturbations, P_T, and scalar perturbation, P_R, (Giovannini, 2017). Scalar perturbations are small variations in a scalar field which is a field where a number describe each point in space and time, e.g. a density field. The scalar perturbation of interest here is the comoving fluctuation in the curvature, R (Riotto, 2002). In a tensor field, each point has a tensor assigned to it. From this, tensor perturbations are small variations acting on the tensor field. The tensor-to-scalar ratio is not strongly constrained, calculations so far only give an upper limit of $r < 0.06$ (Planck X, 2018).

1.2 Extinction of light

In a static space of vacuum, light travels unaffected, and an observer sees the light as emitted. If the space contains light-absorbing matter, an observer sees the light different from the emitted. As starlight travels through a cloud of dust particles, the particles absorb or scatter some of the light (Martin, 2007). Reddening is the process of absorbed light being re-emitted at a lower frequency since the light shifts to the redder part of the electromagnetic spectrum. The calculation of starlight reddening is the difference between observed magnitude at two given frequency bands and the emitted magnitude at the same two frequency bands. It is common in astronomy to use blue, B (observed magnitude using a blue filter), and visual, V (observed magnitude using a yellow filter outside Earth atmosphere), frequency bands (Johnson and Morgan, 1953). We express reddening mathematically as,

$$E(B-V) = (B-V)_{observed} - (B-V)_{emitted}. \tag{1.6}$$

The emitted magnitude is usually not observed but estimated using the spectral class, surface temperature and metallicity of the star. The latter is how much iron per hydrogen there is in the star compared to the sun (Danielski et al. 2018).

[4]The conformal time is the time since Big Bang times the speed of light and describe the maximum distance a photon can have travelled since Big Bang. Therefor also known as the particle horizon.

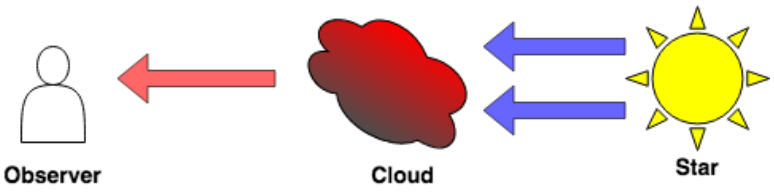

Figure 1.2: An illustration of extinction, where one of the the two blue arrows, representing the emitted starlight, is absorbed and reddened by the cloud when passing through.

Another way of describing the absorption of light is the extinction of light, A, which is the dimming of light when passing through a cloud. The ratio between the extinction of starlight and reddening, $R(V) = A(V)/E(B-V)$, is a useful property in conversion between extinction and reddening (Fitzpatrick and Massa, 1986). To find $R(V)$ from extinction data, we have the ratios, $(A_\lambda - A_V)/(A_B - A_V) \approx -A(V)/(A_B - A_V) = -R(V)$, where λ is a long wavelength giving no extinction (Krügel, 2009), and the difference in extinction of two passbands equals the reddening. $R(V)$ depends on the position in the galaxy; the spectral energy distribution of the star and the amount of reddening (Arenou, Grenon and Gómez, 1992). Figure 1.2 illustrates extinction of light, where the cloud absorbs parts of the emitted light from the star, thus the observer sees a modification of the starlight, with a decrease in magnitude and is reddened.

It is a tight connection between the extinction of light and the optical depth, τ_ν, of the cloud. The optical depth is measured along the path of the light ray from the source at $s = 0$ to a distance s and defined by,

$$\tau_\nu(s) = \int_0^s \alpha_\nu(r) dr, \tag{1.7}$$

where $\alpha_\nu(r)$ is the extinction coefficient defined as the distance derivative of $\tau_\nu(r)$ and varies with the composition and density of the dust cloud. The optical depth is how transparent a medium is, seen from the source, i.e. the information about how far a photon travels before scattering off or being absorbed by a massive particle[5]. Photons can not travel far into or penetrate an optically thick medium, where $\tau > 1$, while for an optically thin medium, $\tau < 1$, photons travels more easily (Rybicki and Lightman, 1979). The intensity I decrease exponentially with τ_ν,

$$I(\nu) = I_{0\nu} \exp(-\tau_\nu), \tag{1.8}$$

where I is the observed intensity, $I_{0\nu}$ is the emitted intensity and ν is the frequency, if $\tau \sim 0$, then $I_\nu \sim I_{0\nu}$. The change in intensity over distance is further connected to the change in optical depth over distance, s,

$$\frac{1}{I_{0\nu}} \frac{\mathrm{d}I_\nu}{\mathrm{d}s} = -\frac{\mathrm{d}\tau_\nu}{\mathrm{d}s} \exp(-\tau_\nu). \tag{1.9}$$

[5]A massive particle is a particle with a mass larger than zero.

The extinction is given as a constant times the line-of-sight integral over the mass extinction coefficient, κ_ν[6], times the dust density, ρ_{dust} (Drimmel, Cabrera-Lavers and López-Corredoira, 2003),

$$A_\nu(R) = 1.086\tau_\nu = 1.086 \int_0^R \kappa_\nu(r)\rho_{dust}(r)dr. \tag{1.10}$$

The constant 1.086 comes from the definition on extinction where, $A_\nu = m_\nu - m_0 = -2.5\log_{10}(I(\nu)/I_0)$, using equation (1.8) for I_ν and $m_\nu - m_0$ is the difference between observed and emitted magnitude (Kutner, 2003). τ depends on the properties of the cloud the light is passing through, like the density and size of the cloud and the absorption properties of the particles in the cloud to name some.

There are other ways of determining the extinction, which require less information on the cloud properties but require assumptions for at least one free parameter. For example, by using the magnitude of the star, this method requires the knowledge of both the observed magnitude (apparent magnitude) m, the emitted magnitude (absolute magnitude) M and the distance, d, to the star. It relates the magnitudes to each other through,

$$m - M = 5\log_{10}(d) - 5 + A_\nu, \tag{1.11}$$

where A_ν is the extinction at the bandpass (Arenou et al. 2018). In equation (1.11) there are two known parameters, d and m, and two unknown parameters, M and A_ν. We need knowledge of the temperature and metallicity of the star to estimate the absolute magnitude. Probing the dust distribution and in the Milky Way and the optical depth, both in the galaxy and to re-ionisation, require good extinction estimates.

1.3 Polarisation

In general, the wave nature of light is electric and magnetic fields oscillating perpendicular to each other in the plane of propagation. In a system of many light-waves, the sum of the oscillations covers every direction in the propagation plane. Equally distributed electric field strength in the plane of propagation gives unpolarised light. The polarisation effect comes from the electric field strength have a larger amplitude in one direction.

Considering only one photon, the magnetic field, $\mathbf{B}$, is related to the electric field, $\mathbf{E}$, through, $\mathbf{E} = -c\mathbf{k} \times \mathbf{B}$, where c is the speed of light and $\mathbf{k}$ is the unit vector in the direction of propagation, writing the electric field strength in complex form and considering only the real and physical part, then decomposing the electric field strength by two real unit vectors, $\mathbf{e}_1$ and $\mathbf{e}_2$, orthogonal to each other in the plane of propagation. By expressing the general form of the electric field strength as a function of time, t, and space, $\mathbf{r}$, we have,

$$\mathbf{E}(\mathrm{r}, t) = \sum_i^2 E_{i0}\mathbf{e}_i \cos(\mathbf{k}\cdot\mathbf{r} - \omega t + \phi_i), \tag{1.12}$$

[6]Note that $\alpha_\nu = \kappa_\nu\rho$.

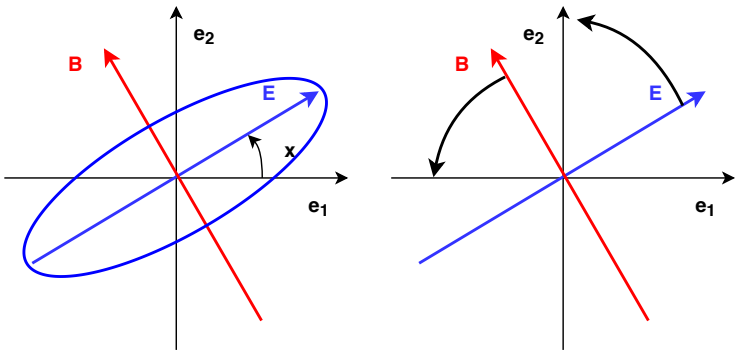

Figure 1.3: The left illustration shows linear polarisation for one photon (the blue arrow) and for an ensemble of photons (blue ellipse), where x is the polarisation angle. The right illustration show circular polarisation where the **E**-field rotates, the bold black arrows illustrate the rotation.

where ω is the frequency of the wave, and ϕ_i is the phase of each of the two orthogonal terms in (1.12)[7] (Leinaas, 2016).

Linear polarisation happens when the phase, $\cos\phi = \pm 1$, then the polarisation intensity is the sum of $E_{10}\mathbf{e}_1$ and $E_{20}\mathbf{e}_2$, and the direction of the polarisation is given as, $\psi = \arctan(E_{20}\mathbf{e}_2/E_{10}\mathbf{e}_1)$. If the two orthogonal components in equation (1.12) are out of phase with 90°, but the amplitude of the two terms are equal, $E_{10} = E_{20} = E_0/\sqrt{2}$, then the electric field will rotate and give circular polarisation (Leinaas, 2016). Figure 1.3, illustrates linear (left) and circular (right) polarisation where the blue arrow represents the **E**-field and the red arrow the **B**-field, the small arrow x from $\mathbf{e_1}$ to **E** is the polarisation angle, ψ, and the blue ellipse in the left illustration shows linear polarisation for an ensemble photons with the amplitude in the different directions. The bold black arrow, in the right figure, shows the rotation of the electromagnetic fields for circular polarisation. In an ensemble of photons, the product of the total intensity, I, and the fraction of linear polarisation, $p = P/I$, describes the polarisation intensity of light. The fraction of polarisation says how much the light is polarised, measured in per cent of the total intensity, so the total polarised intensity, P, divided by the total intensity (Panopoulou et al. 2019). If $p = 100\%$ the ellipse in the left illustration in figure 1.3 reduces to the blue arrow, while $p = 0\%$ gives a circle. For $p < 100\%$, the light is partially polarised, which means each of the photons' **E**-field point in different directions and amplitudes. It is common in astronomy to describe the polarisation through fractional polarisation.

We can decompose polarisation into the Stokes parameters Q and U for linear polarisation (Walker, 1954) and V for circular polarisation. The Stokes parameters, constructed by the product of I and p times spherical

[7]Note: only the relative phase, $\phi = \phi_1 - \phi_2$,is relevant in a physical sense.

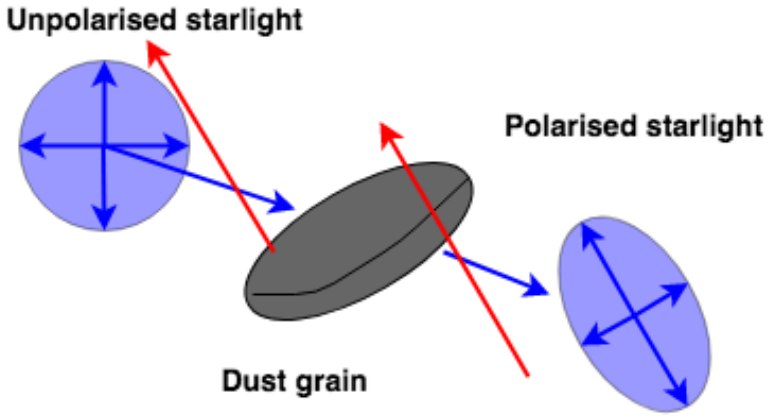

Figure 1.4: The illustration shows how dust grains can polarise starlight. The blue circle is the unpolarised light, the dark grey clump is the dust grain perpendicular to the magnetic field (red arrows), and the blue ellipse is the polarised light.

coordinate factors, provide a mathematical way of describing polarisation,

$$I = \sqrt{Q^2 + U^2 + V^2} \tag{1.13}$$
$$Q = Ip\cos(2\psi)\cos(2\chi) \tag{1.14}$$
$$U = Ip\sin(2\psi)\cos(2\chi) \tag{1.15}$$
$$V = Ip\sin(2\chi), \tag{1.16}$$

where ψ is the polarisation angle in the plane of propagation ($\mathbf{e}_1, \mathbf{e}_2$ plane for example) and χ is the angle between the propagation plane ($\mathbf{e}_1, \mathbf{e}_2$) and the direction of propagation ($\mathbf{k}$). For linear polarisation $\chi = 0°$ since the plane $(\mathbf{e}_1, \mathbf{e}_2)$ points in the same direction as $\mathbf{k}$, while for circular polarisation, the phase-shift give a non-zero χ. The factor 2 in front of the ψ comes from the symmetry of rotating the angles 180° and the 2 in front of χ is the symmetry of ellipse rotation by 90° (Walker, 1954). Q and U describe linear polarisation where there are difference in the magnitude in $\mathbf{e}_1, \mathbf{e}_2$ direction, Q goes along each of the two axis, while U goes on the diagonal. If the polarisation angle is close to 45° Q is close to zero and U is at a maximum. In particular, U rotated 45° shift the polarisation to Q. V describe the circular polarisation which is independent of ψ. From the Stokes parameters we can construct fractional Stokes parameters dividing by I giving q, u and v (Panopoulou, 2019).

In the next paragraph, we discuss the polarisation of starlight and describe it using Stokes parameters.

1.3.1 Starlight polarisation

In general, starlight is usually not polarised; however, when travelling through the ISM, it can be polarised by hitting dust grains. The polarisation of starlight is an effect of the alignment and shape of the dust grains

acting as a polarisation filter where the reduction in intensity decrease most parallel to the grain elongation. The magnetic field orientation in the ISM determines mainly the dust grain alignment, and this makes polarisation of starlight a good tracer of the distribution of dust (Martin, 2007). The illustration in figure 1.4 show the process of polarising starlight, the blue circle (unpolarised) and ellipse (polarised), with the dust grain (dark grey clump) perpendicular to the magnetic field shown in red arrows. The blue arrows show the amplitude in different directions and where the light goes. We usually report starlight polarisation in fractional polarisation p_v,

$$q_v = p_v \cos 2\psi_v \tag{1.17}$$

$$u_v = p_v \sin 2\psi_v, \tag{1.18}$$

where ψ_v is the polarisation angle for visual frequencies.

1.3.2 E and B modes

The polarisation components given by the Stokes parameters Q and U are elements of a symmetric-trace-free 2×2 tensor field, $P^{\mu\nu}$,

$$P^{\mu\nu} = \frac{1}{\sqrt{2}} \begin{bmatrix} Q & U \\ U & -Q \end{bmatrix}. \tag{1.19}$$

The tensor property comes from the dependency of observation direction, $\mathbf{k}$, and the axes, $\mathbf{e}_1, \mathbf{e}_2$, perpendicular to $\mathbf{k}$ (Gorski et al. 2010). By decomposing the polarisation tensor into a curl-free part and a divergence-free part, E-modes and B-modes are defined respectively, $\partial_\mu \partial_\nu \mathbf{P}^{\mu\nu} = \nabla^2 E$ and $\epsilon_{\mu\gamma} \partial_\nu \partial_\gamma \mathbf{P}^{\mu\nu} = \nabla^2 B$[8]. By rotating a pure E-mode 45° to the wave vector, $\mathbf{k}$, give a pure B-mode, this means the polarisation orientation varies while the strength is constant (Kamionkowski and Kovetz, 2016). Further, by transforming the Stokes parameters into spherical harmonics of the angular position, we find E- and B-modes. The calculation of the E- and B-mode power spectra uses two-point statistics on the temperature-polarisation map (Kamionkowski and Kovetz, 2016).

The generation of E-modes comes mainly from scalar perturbations and small contributions from tensor perturbations. The contribution of both scalar perturbations and tensor perturbations makes the probing of E-modes difficult since they are hard to separate. The scalar perturbations producing E-modes come from density fluctuations of matter. Only tensor perturbations generate B-modes. B-modes come from two astrophysical effects, the first one is gravitational lensing. Since the photons of the last scattering travels through a universe containing clumps of matter bending the light toward an observer which transforms the primordial E-modes into B-modes. The gravitational lensing becomes significant for small angular scales $\leq 2°$ (Krauss, Dodelson and Meyer, 2010). The second way is by gravitational waves from inflation, causing the matter density to fluctuate in a tensor field. A way of constraining the B-modes is to calculate the

[8]The symbols $\epsilon_{\mu\gamma}$ is the anti-symmetric tensor, ∂_μ is the partial derivative operator and ∇ is the gradient operator

tensor-to-scalar ratio, r. The tensor perturbations are small, no more than 10^{-9} K (Planck Collab. X, 2018).

Another critical parameter to estimate with high precision that affects the polarisation of the CMB is the optical depth to re-ionisation, τ, in the universe. τ measures how transparent a medium is. One can describe this parameter as the cosmological distance to when the first stars were born. As the first stars were born and began to re-ionise the universe, the transparency evolution after recombination fell more gradually off considering the expansion. The contributing effect of τ on polarisation is at large scales, and what we want to measure. The change in transparency affects the polarisation of the CMB since the re-ionisation freeing electrons from neutral hydrogen. The free electrons and the photons from the CMB interact through Compton scattering such that CMB photons get a new polarisation. τ affects the B-modes of CMB from the scattering between tensor-perturbations and re-ionisation, this connects the τ to the B-modes and r (Planck Collab. Int. XLVI, 2016).

Chapter 2

The Microwave Sky

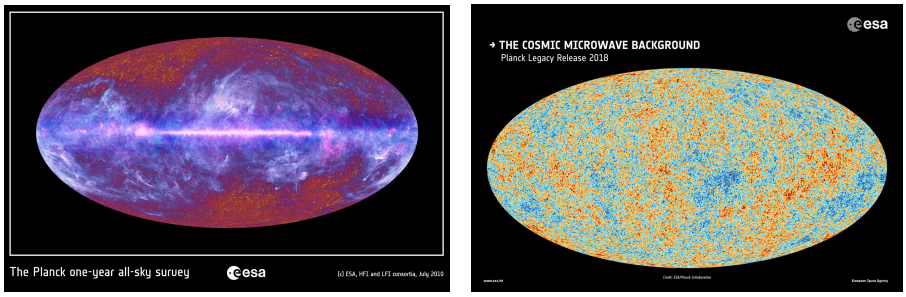

(a) All signal (b) CMB temperature

Figure 2.1: The full microwave sky containing all sources to the left at multi-frequency of Planck Collaboration, a combination of the nine frequency bands, to the right is the CMB temperature map. Pictures are from (Planck Collab. 2013) and (ESA and the Planck Collaboration, 2019).

Today we observe the first free photons in the universe as the CMB. The observations of the CMB shows the same temperature of 2.7255 K all over the sky with small fluctuations in magnitude, in order of $\mathcal{O}(10^{-5}\text{K})$ (Fixen, 2009), giving a perfect blackbody spectrum showing a universe in thermal equilibrium. Figure 2.1 show the full sky seen in microwave (left) and the CMB signal (right). The small temperature variations we observe in the CMB come from quantum fluctuations in the inflationary universe distributing matter unevenly. The inflation stretched the space and smoothed out these fluctuations to be small in amplitude (Guth, 2007). The observations of the blackbody spectrum, at all points in space, with temperature fluctuations too small to violate the homogeneity and isotropy, proves the cosmological principle (Guth, 2007). The reason this is important is by looking at the universe on large scales. The distance between two points in the early universe was too large for any information to exchange, and these two points are in thermal equilibrium.

The outline of this chapter is first with a description of the angular power spectrum of the CMB. In the second section, we discuss the different components emitting radiation in the microwave regime, and the third

section is discussing the polarisation of the CMB. In the end, we look at the future of the field.

2.1 The CMB Power Spectrum

From the photons of the last scattering, cosmologists get plenty of information. The angular power spectrum of the CMB temperature show the strength of variation and the angular separation in the sky as the observable, showing how much the temperature variation is over angular scales, from 90° to 0°. The angular power spectrum contains all information about the CMB, if the CMB is statistically isotropic and Gaussian distributed over the full sky (Planck Collab. XI, 2016). Through decomposing the temperature variation to spherical harmonics[1] using Fourier transformation, we obtain the power spectrum from the mean square of the Fourier coefficients a_{lm},

$$C_l = \frac{1}{2l+1} \sum_{m=-l}^{m} |a_{lm}|^2, \tag{2.1}$$

where $l = 1/\text{angle}$ is the angular separation node, and m is the order of the spherical harmonic (Hinshaw et al. 2003). The angular power spectrum gives scientists vital information on constraining the cosmological parameters, like the above mentioned relative densities Ω_x and H_0. Small deviations on these parameters give enormous impacts on the state of the universe, for example, when the occurrence of the last scattering happened (Umiltà et al., 2019).

2.2 The intensity Sky

The observed signal in the microwave regime contains a large amount of information. Much of this information comes from sources like distant galaxies, nebulae and stars, but hidden within the microwave signal lays the CMB, see figure 2.1 (Planck Collab. 2013) and (ESA and the Planck Collaboration, 2019). For us to observe the CMB clearly, we need to remove the signals coming from stars, galaxies and the ISM, to name some. These different signals are called foreground signals, or foregrounds, and the major contributor is the Milky Way galaxy. Observations of the Milky Way shows emission from synchrotron radiation, heated dust particles, free-free emission, spinning dust and CO line emission to name some. The foregrounds also contain signals from sources outside of the Milky Way, called extragalactic foregrounds (Planck Collab. XII, 2014).

A way of describing the energy of radiation from a source is through spectral energy distribution (SED), which is the energy as a function of frequency or wavelength. For example, a blackbody spectrum is the SED

[1]Spherical harmonics are orthogonal functions defined on the surface of a sphere.

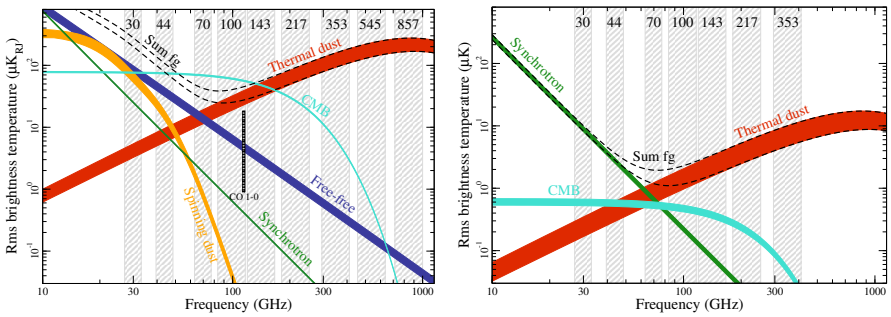

(a) (b)

Figure 2.2: The brightness temperature of different components as a function of frequency. The left plot shows the intensity of all the different foreground components. The right plot shows the intensity of the components of the polarised foreground. From (Planck Collab. X, 2016).

for radiation in thermal equilibrium and is defined mathematically as,

$$B_\nu(T) = \frac{2h\nu^3}{c^2} \frac{1}{\exp\left(\frac{h\nu}{k_B T}\right) - 1}, \tag{2.2}$$

where ν is the frequency, T is the temperature, h, k_B and c are the Planck constant, Boltzmann constant and the speed of light, respectively. The SED is used to find how much energy there is of a foreground at a given frequency. Each foreground has different SED, including the CMB signal which follows a blackbody spectrum. The different SEDs allow scientists to extract the CMB signal from the total signal by separating the SEDs from each other. The SED of the CMB is,

$$I_{CMB} = A_{CMB} \frac{x^2 e^x}{(e^x - 1)^2} \tag{2.3}$$

where $x = h\nu/k_B T$ as given in (Planck Collab. X, 2016). The different properties of each foreground need to be known to construct good SED models for scientists to model the foregrounds in a good way. In long-wavelength astronomy, it is common to express the intensity of the SED in brightness temperature, which is the temperature a blackbody spectrum needs to reproduce the observed intensity. Figure 2.2 show the root-mean-square brightness temperature as a function of frequency for different components in the microwave signal both for total intensity and for polarised intensity.

The following subsections describe several of the different foregrounds.

2.2.1 Synchrotron radiation

One type of foreground is synchrotron radiation, which is generated by relativistic electrons moving in spirals along magnetic field lines (Planck Collab. X, 2016). The SED of synchrotron radiation only depends on

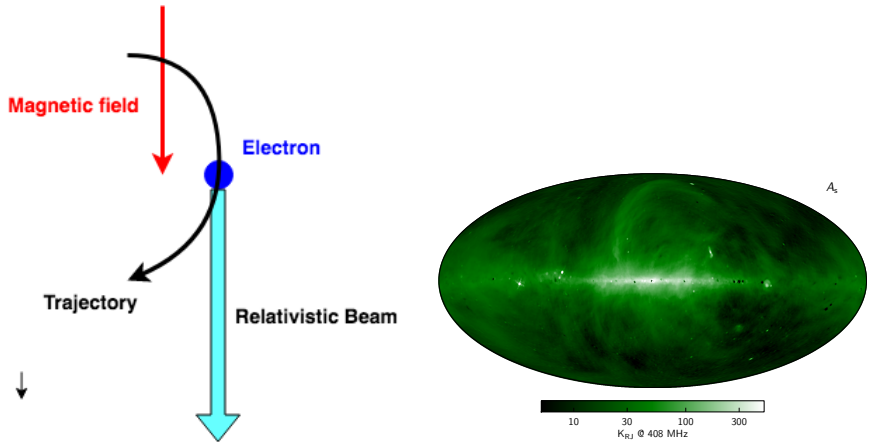

(a) Illustration of relativistic beaming (b) Synchrotron intensity

Figure 2.3: To the left, an illustration of synchrotron radiation and relativistic beaming as the arrow. Right, the intensity map of synchrotron radiation derived from joining observations at different frequencies (Planck Collab. X, 2016).

the energy distribution of the electron. For instance, the strength of the magnetic field the electron moving through changes the amplitude of the SED but not the frequency, which means the magnetic field strength only changes the amplitude of the energy. For a non-relativistic electron, the radiation an observer sees oscillates as the electron spirals around, giving a periodic frequency with maximum tangential on the direction of motion and minimum perpendicular to the direction of motion. For relativistic electrons giving synchrotron radiation, the radiation comes in sharp pulses through a beam pointing in the direction of motion of the spiralling electron. The beaming is caused by relativistic effects, stretching out the radiation in the direction of motion of the electron. The frequency of the radiation pulses only depends on the strength of the magnetic field. An observer only sees the synchrotron radiation when the radiation beam points toward the observer (Rybicki and Lightman, 1979). Figure 2.3a illustrates the beaming, where the light blue arrow is the relativistic beam emitted by the electron (blue dot) moving in the magnetic field. As a foreground, the emission of synchrotron radiation is dependent on the Galactic magnetic field strength and the distribution of cosmic-ray electrons. Figure 2.3 show the synchrotron radiation filling the sky. The intensity of the synchrotron radiation may be approximated by,

$$I_s = A_s \left(\frac{\nu_0}{\nu}\right)^{\beta_s}, \tag{2.4}$$

where A_s is the amplitude, dependent on the position in the sky, ν_0 is the reference frequency and β_s is a spectral index dependent on sky coordinates (Planck Collab. X, 2016). The spectral index carries information about the physical nature of the emission origin.

2.2.2 Thermal dust

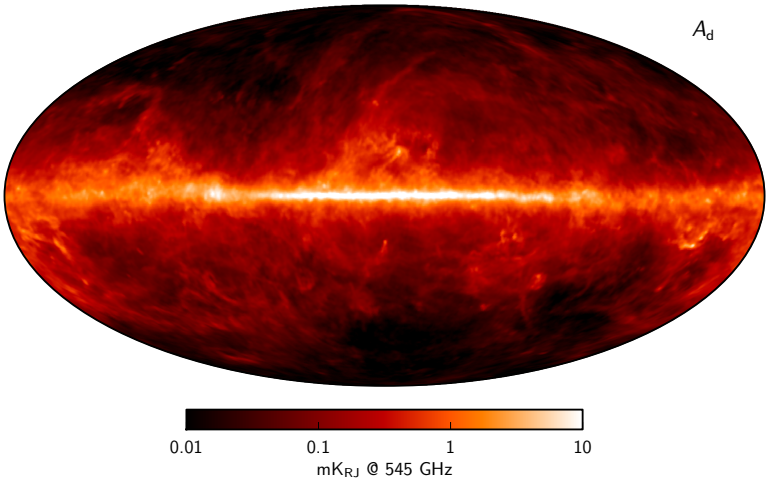

Figure 2.4: The dust amplitude from joining observations at different frequencies (Planck Collab. X, 2016).

The ISM contains dust, which made up of silicate and carbonaceous grains or a combination. These grains absorb ultra-violet and optical radiation which heats them. The heated dust grains radiate away the thermal energy gained in infrared and microwave radiation, thermal radiation, and therefore thermal dust. A modified blackbody model can describe empirically the intensity I of thermal dust emission at a given frequency ν, and we express it as a blackbody spectrum, $B_\nu(T_d)$, at the dust temperature, T_d, multiplied by a power law of frequency,

$$I_d(\nu) \propto \tau \nu^{\beta_d} B_\nu(T_d), \tag{2.5}$$

where β_d is the spectral index of the power-law (Planck Collab. XII, 2018). Equation (2.5) may be written on the form,

$$I_d(\nu, p) = A_d(p) \frac{e^{h\nu_{0,d}/k_B T_d(p)} - 1}{e^{h\nu/k_B T_d(p)} - 1} \left(\frac{\nu}{\nu_{0,d}}\right)^{\beta(p)+1}, \tag{2.6}$$

where $I_d(\nu, p)$ is the signal for the frequency ν at pixel p, $A_d(p)$ is the amplitude at pixel p, $\nu_{0,d}$ is a reference frequency, $T_d(p)$ is the brightness temperature from the dust emission in the current pixel, and $\beta(p)$ is the spectral index of the current pixel (Planck Collab. XII, 2014). This free parameter for the total dust intensity is varying between 1.3 and 1.8, with a mean of 1.55 over the full sky (Planck Collab. X, 2016). The model is dependent of the temperature of the dust grains, which may vary with the environment and population of the dust grains (Planck Collab. X, 2016), and the power law of the frequency. Since the dust distribution is more complex at high frequencies, the model Planck Collab. X (2016) uses a single component dust model which describes the thermal dust for frequencies up to 857 GHz, where the dust distribution description is easier than for example in a two-component dust model.

2.2.3 Free-free emission

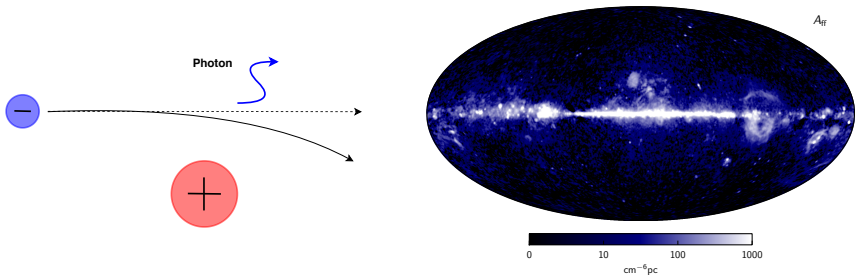

(a) Illustration of free-free interaction (b) Free-free intensity

Figure 2.5: (Left) An illustration of free-free interaction where the blue filled circle is a negatively charged particle, and the red-filled circle is a positively charged particle. The dashed line shows the original path of the blue particle, the curved line shows the path because of deceleration, and the zig-zag line represents the emitted photon. (Right) The free-free intensity derived from joining observations at different frequencies (Planck Collab. X, 2016).

When a free charged particle moves in the electric field of another particle of opposite charge, for example, an electron in the E-field of a proton, the free electron undergoes an acceleration perpendicular to the path of the free electron. The perpendicular acceleration changes the path of the free electron, producing a deceleration of the electron. The change in kinetic energy of the free-electron produces a photon and thus obtaining conservation of energy. The emitted radiation is called free-free or "Bremsstrahlung" from the braking of the free electron interacting with the free ion (Rutten, 1988). The right plot in figure 2.5 show the observed free-free emission over several frequency bands and in the left plot, we illustrate the free-free interaction. The right figure shows the free-free intensity observed by Planck, where we see that free-free emission is strong at low frequencies $\nu < 100$GHz (Planck Collab. X, 2016). One way of tracing the free-free emission is to look at the Hα optical line emission. Hα is the strongest emission line for neutral Hydrogen and comes from energy transition from energy state 3 to energy state 2 of an excited Hydrogen atom. The radio wavelength production of free-free emission and the optical Hα emission comes from the same ionised gas, meaning Hα traces the electron column density together with the electron temperature. Both Hα and free-free are proportional to the emission measure ($EM = \int n_e^2 dl$) such that the Hα intensity and free-free brightness temperature has a well-defined relationship. These properties determine the emission strength (Banday et al. 2003).

2.2.4 Anomalous Microwave Emission

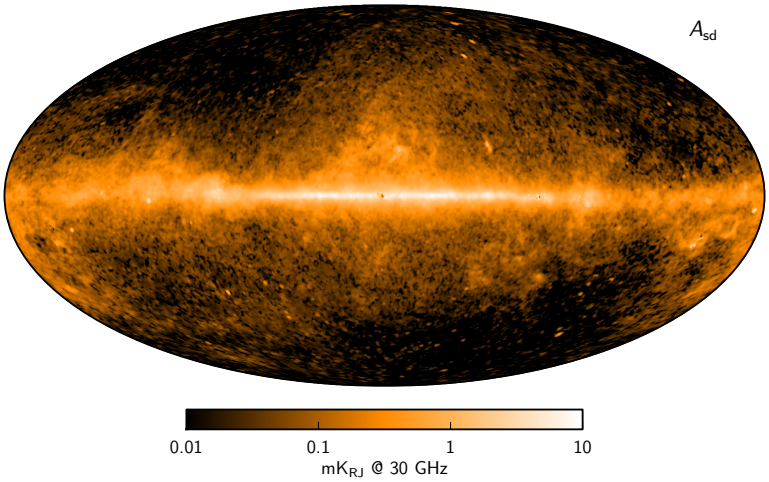

Figure 2.6: The intensity of the sum two spinning dust models derived from different observations used in Planck Collab. X (2016).

Early work on foreground subtraction showed an excess of galactic emission at low frequencies, between 10 to 50 GHz (Kogut et al., 1996; de Oliveira-Costa et al., 1997; Leitch et al., 1997). At low frequencies, 10 to 100 GHz, emission from only synchrotron and free-free can not explain the microwave signal, see figure 2.2a. This additional emission is called Anomalous Microwave Emission (AME) and is not fully understood, but there are some theories of spinning dust and alternative methods. The spinning dust model may be the most prominent since dust grains can move in space, they vibrate and rotate caused by collisions with for example atoms. The rotation will lead to microwave emission if the dust grains have an electric or magnetic dipole moment different from zero. The emission of spinning dust and thermal dust are tightly correlated (Draine and Lazarian, 1998). Even though the true nature of AME is not well understood, scientists can separate it from the other components of the foregrounds and the CMB in data analysis because of modelling based on phenomenological grounds. The spectral behaviour of AME are strong at low frequencies and falls rapidly off at $\nu > 50$GHz, fig. 2.2a, (Planck Collab. X, 2016).

2.2.5 CO line emission

Molecular emission lines are sharp peaks in the intensity as a function of frequency and originate from a transition of a high energy state, J, of the molecule to a lower energy state, $J' = J - 1$. These transitions make the molecule emit a photon with a specific energy equal to the energy difference of the high and the low energy state of the molecule.

The frequency of the emitted photon depends on the energy difference between the two energy states. Since Carbon Monoxide (CO) has an antisymmetry, it has an electric dipole moment and is rotating. Changes

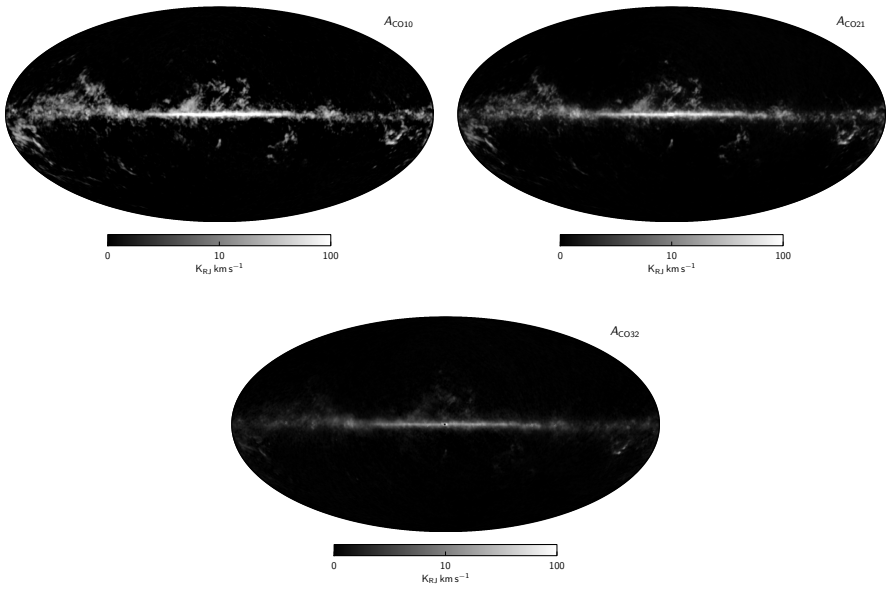

Figure 2.7: The three emission-lines of Carbon Monoxide observed by Planck, to the left, is for the lowest energy state $J = 1 \rightarrow 0$, in the middle $J = 2 \rightarrow 1$ and to the right $J = 3 \rightarrow 2$ (Planck Collab. X, 2016).

in the rotations can make the energy jumps J mentioned above, where J is the angular momentum quantum number (Planck Collab. XIII, 2014).

If a bandpass frequency range covers sharp emission lines, it is necessary to account for the line emission. Carbon Monoxide has line emissions in three of the Planck bandpasses, 100, 217 and 353 GHz (Planck, 2016). The first line, $J = 1 \rightarrow 0$, is at 115 GHz, the second line, $J = 2 \rightarrow 1$, at 230 GHz, and the third line, $J = 3 \rightarrow 2$, at 345 GHz. Since these emission lines are from discrete energy transitions in the molecule, it is easy to predict and correlate across frequencies. The location of CO molecules are in star-forming regions. These regions also contain thermal dust, which means CO and thermal dust traces each other (Planck Collab. XIII, 2014).

2.2.6 Zodiacal light emission

Zodiacal light is emission from dust particles inside the solar system. Most of the emission comes from the asteroid belt between Mars and Jupiter. Solar radiation heats the dust grains to a temperature of about 150 K. The heating makes the dust grains radiate thermally, similarly as the ISM dust grains, meaning the SED and frequency spectrum are similar as for ISM dust. A relevant feature of the Zodiacal light is it changes with time during a survey. For example, when Planck moves with the Earth around the Sun, the line of sight to the Zodiacal light changes. The modelling of this dynamic foreground must be time-dependent. For Planck, Zodiacal light is present in frequency bands from 70 GHz and higher (BeyondPlanck I, InPrep.).

2.2.7 Extragalactic foregrounds

Outside the Milky Way galaxy, extragalactic sources emits radiation in the microwave regime. Such signals are named extragalactic foregrounds, and we give a brief description of the three primary contributors in the CMB signal.

First is the Cosmic Infrared Background (CIB), which is thermal dust emission from many distant galaxies. Similar to the CMB, we approximate the CIB as a spatial field with a SED defined as the average of many independent SEDs from thermal dust. Each of the independent SEDs have a red-shift according to the distance to the galaxy.

The CIB affects the CMB observations in two ways. The first effect is the uncertainties of CIB monopole[2] sets a bias on the uncertainties of the High-Frequency bands zero-level[3]. The other effect of CIB on the CMB is the fluctuations of CIB around the galactic poles are more extensive than thermal dust fluctuations at the galactic poles (Planck Collab. X, 2016) and (BeyondPlanck I, InPrep.).

The next extragalactic foreground are compact radio sources, such as active galactic nuclei (AGN) giving highly polarised synchrotron radiation. Most AGNs are distant galaxies observed as point sources in CMB experiments and strewn in the sky. The synchrotron emission from AGNs are variable on timescales from days to years (BeyondPlanck I, InPrep.).

And the third and last extragalactic foreground source are the Sunyaev-Zeldovich effect, which is the effect of CMB photons scattering off hot electrons in galaxy clusters. The scattering gives CMB photons a slightly higher frequency. The hot electron clouds in galaxy clusters may have a bulk velocity, this bulk velocity gives the photons a Doppler shift conserving the blackbody spectrum but changes the temperature. (Planck Collab. X, 2016).

2.3 The Polarisation Sky

From the temperature field of the CMB, the extraction of information is comprehensive, and constraints on the astrophysical parameters are strong. However, the polarisation of the CMB is still a hot science case, where the ultimate goal is to detect gravitational-wave imprints from inflation and estimate the optical depth to re-ionisation. Since Compton scattering produce polarisation, it polarises the CMB photons to some degree. During Compton scattering, the intensity of the incoming photons are different in such a way that the outgoing intensity differs in the plane of propagation (Dodelson 2003). For the polarisation imprint in the CMB, the scattering cannot be too intensive because small distances between electrons causes thermal equality between the two electrons and the mean free path of the photons is short. For increasing distances between the electrons, the electron temperature will be a little different, and the scattering between

[2] A monopole is the first spherical harmonic, as it has one peak and no "anti-peak".

[3] Zero-level is the signal the detector observes by observing, for example, a grey wall. It is crucial to correct for the zero-level since it clarifies the quality of the detector pixels.

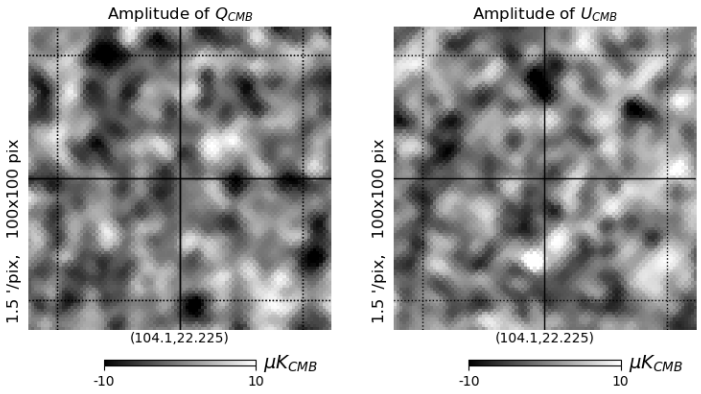

Figure 2.8: The polarisation of the CMB in a small part of the sky, produced from CMB polarisation data smoothed to 10 arcmin from Planck Collab. (2018). The left plot shows the Q polarisation, where the pattern is horizontal/vertical. The right plot shows the U polarisation where the pattern is diagonal instead. The zoom-in is to highlight the patterns of Q and U.

electrons and photons is less intensive which produce a net polarisation (Krauss, Dodelson and Meyer, 2010). Compton scattering does not start a rotation of the electric field of the electron and thus only produce linear polarisation, it is common to assume a negligible circular polarisation V. Figure 2.8 shows the amplitude of the CMB polarisation in a small part of the sky. The left plot shows the amplitude of the Q polarisation, and the right plot shows the amplitude of the U polarisation. In both plots, the vertical/horizontal pattern of Q and diagonal pattern of U comes forth and is similar to maps from Planck Collab. X, (2016).

2.3.1 Polarised foreground components

The significantly polarised foregrounds are the synchrotron radiation and thermal dust emission. In synchrotron radiation, relativistic electrons emits highly polarised radiation, at about $\sim$ 75% polarised, this means the contribution of polarised synchrotron radiation of the foreground is significant and make a big impact on the E- and B-modes. The Milky Way galaxy has a magnetic field which affects the polarisation of synchrotron radiation due to the charged particles accelerating in the magnetic field. Further, starlight polarisation is because of dust grains alignment to the surrounding magnetic field (Rybicki and Lightman, 1979; Planck Collab. X, 2016; Hensley, Zhang and Bock, 2020).

On polarisation of thermal dust, the dust grains must be aspherical and aligned. The galactic magnetic field produces alignment among the dust grains. If the grain is spherical, it will emit the same amount of radiation in every direction. Also, from a dust cloud with random distribution in

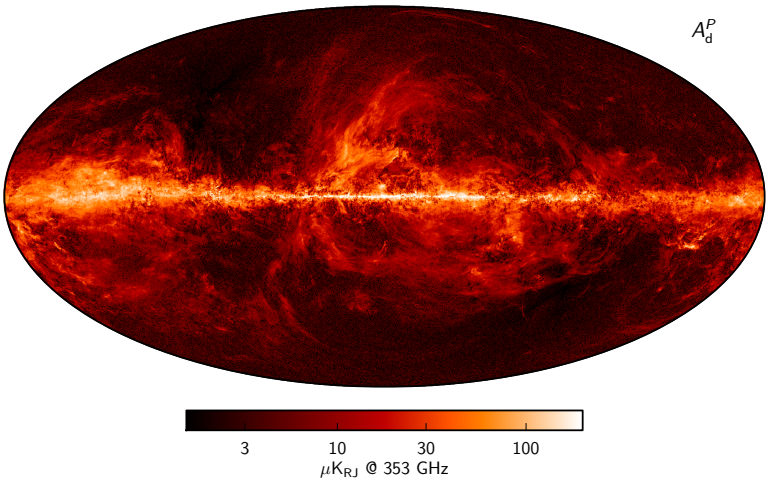

Figure 2.9: Polarisation amplitude of thermal dust at 353 GHz from Planck (Planck Collab. X, 2016).

grain orientation, the total emission has no net polarisation (Martin, 2007). Since observations of thermal dust emission intensity is around $\sim$ 10% polarised, the alignment of the dust grains are significant to some degree (Planck Collab. XII, 2018). Further, the alignment seems to be dependent on the composition of the dust grains, where silicates give robust polarisation, and carbonaceous grains radiates little polarisation (Martin, 2007). Figure 2.9 show the polarisation amplitude of thermal dust at 353 GHz (Planck Collab. X, 2016). Along the galactic disc, the amount of polarisation is much stronger than of the galactic disc. To the left in the map, a sizeable area contributes to plenty of polarisation. The galactic centre is in the middle of the map.

Martin (2007) states that both the polarisation of optical starlight and thermal dust emission depend on the shape of the aligned dust grains in the ISM. The polarisation of thermal dust emission is parallel to the elongation of the dust grains, while the starlight polarisation is due to differential extinction. We often model the shape of a dust grain as an ellipsoid with the three principal axes, $x_1 \leq x_2 \leq x_3$, and unit vectors, $\mathbf{x}_1, \mathbf{x}_2, \mathbf{x}_3$. The dust grains rotate about their short axis, $\mathbf{x}_1$, with an angular momentum, $\mathbf{J}$, which means, $\mathbf{J} \parallel \mathbf{x}_1$. Further, the angular momentum is parallel with the magnetic field, $\mathbf{B}$, in the ISM and, $\mathbf{x}_1 \parallel \mathbf{B}$ (Henslay, Zhang and Bock, 2019). A heated elongated dust grain emits more radiation along its long axis than the short axis. Thus the polarised emitted radiation is parallel to the elongation.

For starlight, the elongated dust grain absorbs more radiation along the long axis than the short axis, letting most light pass by along the short axis. Guillet et al. (2018) show that prolate shape produces more efficiently polarisation in optical than oblate dust grains. If grains are rapidly spinning about their spin-axis giving maximum momentum of inertia, and this axis is on average aligned with the surrounding magnetic field, an oblate grain shape give less momentum of inertia than a prolate particle.

Thus, the electric field vector of the thermal emission from the grains are perpendicular to the surrounding magnetic field. The electric field of the starlight polarisation is parallel to the surrounding magnetic field, which means the polarisation of starlight is orthogonal to the polarisation of thermal dust (Martin, 2007; Planck Collab. XII, 2018). Figure 1.4 illustrates the production of submillimeter and starlight polarisation.

A way of comparing polarisation from thermal emission and starlight is through the ratio,

$$R_{P/p} = \frac{P_s}{p_v}. \tag{2.7}$$

The polarisation ratio measures how efficient the grains are at producing polarised emission compared to polarising starlight in submillimeter and visual spectra. This ratio has the same units as the submillimeter polarisation. P_s depends on the shape and alignment of the dust grains, and p_v depends on the extinction. Furthermore, both properties depend on the column density of the ISM. The properties like the shape of the grains, the efficiency of the alignment and magnetic field orientation affects the polarisation in visual, p_v, and in submillimeter, P_S, in similar ways (Planck Collab. Int. XXI, 2015; Planck Collab. XII, 2018). $R_{P/p}$ also indicate information about the shape and porosity of the dust particles. Guillet et al. (2018) investigated how the elongation of silicate grains changes the ratio P_s/p_v for different porosity levels. Further, they show that for a given size, oblate grains polarise more than prolate grains and this difference is greater in the optical than in submillimeter, such that prolate grains give higher values of $R_{P/p}$.

2.3.2 CMB E and B modes

In CMB analysis, E and B modes are of importance, giving more information about the early universe. E-modes are polarisation induced from density perturbations increasing the Compton scattering between electrons and photons. B-modes are polarisation produced from primordial gravitational waves and gravitational lensing when photons are travelling through the curved space-time. The angular power spectrum shows the strength of E and B modes as a function of angular separation, similar as for the temperature. Figure 2.10 shows the power spectrum of temperature, and E- and B-modes. There are big differences in the amplitude of the different power spectra shown, with the strongest signal given by temperature in the red line, the green line is the angular power spectrum of E-modes, the dashed blue line is the B-mode power spectrum from gravitational lensing. The two solid blue lines represent the angular power spectrum of primordial gravitational waves for two different tensor-to-scalar ratios r (Krauss, Dodelson and Meyer, 2010).

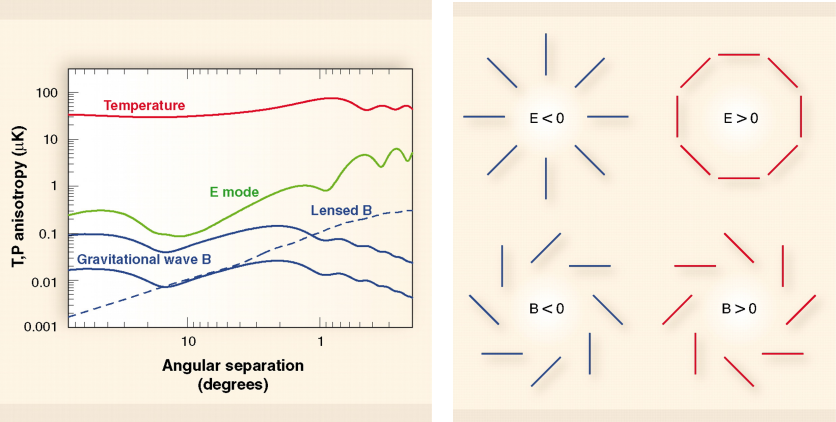

Figure 2.10: The left figure shows the angular power spectrum of temperature in the red line, E-modes in green line and B-modes from gravitational lensing as dashed blue line and from gravitational waves as solid blue lines (tensor-to-scalar ratio $r = 0.3$ and $r = 0.01$). The right figure shows a drawing of the appearance of E-modes and B-modes. The figures are from Krauss, Dodelson and Meyer (2010).

Table 2.1: The newest estimates of the tensor-to-scalar ratio r and the optical depth to re-ionisation, τ. The results are from (Planck Collab. X 2019)

Planck 2018 results	
r	< 0.056
τ	0.053 ± 0.009

2.4 The future of CMB analysis

The next goal within CMB analysis is the detection of primordial gravitational waves as a weak imprint on the polarisation of the CMB.

To get an undisturbed CMB signal, we must remove the foreground contributions in the data received from telescopes. The primordial gravitational waves are very faint, so to detect them, the foreground removal must be very accurate. The instruments used in CMB experiments have not been sensitive enough, together with the removal of foregrounds in component separation simulations. Table 2.2 lists the sensitivity of Planck (Planck Collab. I, 2011). To improve the foreground removal, both the sensitivity of the instruments and accuracy of the component separation must increase. In theory, the estimation of B-signal is nine orders of magnitude fainter than the CMB and three orders of magnitude fainter than the E-mode signal (Krauss, Dodelson and Meyer, 2010). The tensor-to-scalar ratio, r, is one of the important parameters to estimate in future experiments on CMB. The optical depth, τ, to re-ionisation is another important parameter giving a contribution to the polarisation of the CMB since the larger values of τ show more matter the CMB photons may scatter on.

Table 2.2: Instrumental sensitivity of Planck. The table consists of each bandpass [GHz] with beam size [arcminutes], white-noise sensitivity (WN sens.) [$\mu K_{RJ} s^{1/2}$], calibration uncertainty (cal. unc.) [%] and flux density of the faintest source (min flux) [mJy]. Data taken from Planck Collab. I (2011).

Bandpass	30	44	70	100	143	217	353	545	857
beam	32.65	27.92	13.01	9.37	7.04	4.68	4.43	3.80	3.67
WN sens.	143.4	164.7	134.7	17.3	8.6	6.8	5.5	4.9	2.1
cal. unc.	1	1	1	2	2	2	2	7	7
min flux	480	585	481	344	206	183	198	381	655

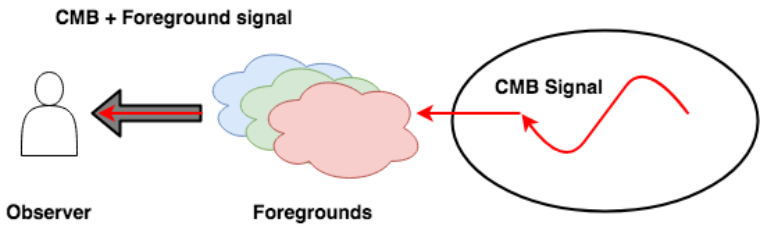

Figure 2.11: Illustration of the microwave signal, where the red arrow represents the CMB signal hidden inside the full observed signal, shown as the big grey arrow. The three clouds are different foregrounds.

Since the distribution of interstellar radiation influence the dust temperature, the 3D ISM structure becomes crucial in the analysis of foreground contamination in the CMB (Vergely et al., 2010). One of the main features of the ISM is it emits radiation at the same frequencies as of CMB, the illustration fig. 2.11 demonstrates this. Extinction of light in the ISM helps to understand and trace the properties of thermal dust. Correction for extinction is vital for astrophysical and cosmological studies of sources in the background of the ISM (Marshall et al. 2006). Since the CMB analysis is full-sky and at all distances, the modelling of the ISM as a foreground is crucial.

Chapter 3

Experiments

To constrain models of the ISM, data sets of the full sky covering a wide range of frequencies are essential. To map the extinction and polarisation caused by the ISM, we use observations at microwave and optical frequencies. Only a small part of the electromagnetic radiation hitting Earth atmosphere penetrates down to the ground, which means ground-based telescopes cover a small part of the electromagnetic spectrum hitting us. Furthermore, at least two ground-based telescopes are needed to cover the full sky, e.g. a telescope at the equator sees most of the sky but barely the sky-poles, while two telescopes located south and north of the equator can see both the sky-poles and the rest of the sky. Space telescopes, on the other hand, can cover the entire electromagnetic spectrum and full sky but are much more expensive. The different telescopes have distinct features on what they observe both on the instruments, like spectroscopy, photometry, polarimetry and astrometry, and spectral passbands. Combining the different features give information about the sources and help construct models of the ISM. This chapter describes the different experiments and studies used in this thesis, and the experiments considered are, Gaia, the surveys Green et al. (2019) used, Planck and RoboPol with Pasiphae.

3.1 The Gaia satellite

The Gaia satellite is a satellite operated by ESA on a mission to catalogue vast amount of stars in the Milky Way galaxy. The satellite observes the full sky. The second data release from Gaia (Gaia DR2) in 2018 gave information about stellar positions to almost 1.7 billion stars and objects and measured the parallax angle to 1.3 billion objects. Earlier stellar catalogues with parallax estimates are less precise due to the location of the Gaia Satellite at L2, meaning the position is 1 million kilometres further away from the sun. The parallax angle is the angle between the sun, the star and the observer, such that the larger orbit radius give larger and more accurate angles. The satellite measures the apparent magnitude of the star in three bandpass filters, G, G_{BP} and G_{RP}, where the G filter measurement are for every star in the catalogue, while the two other filters are on 1.3

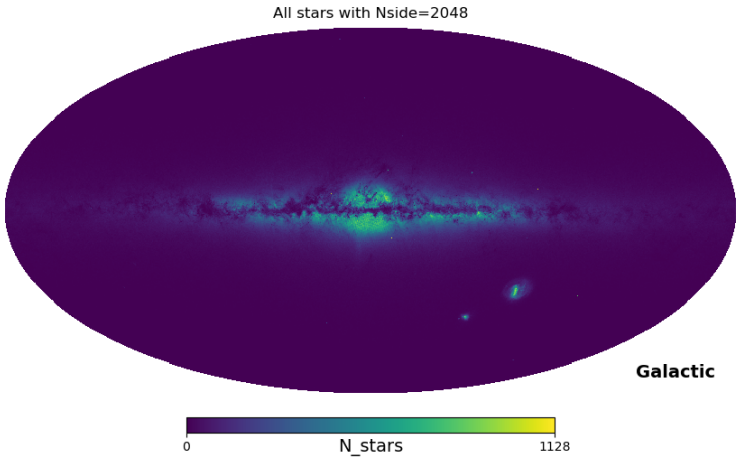

Figure 3.1: The full star map of Gaia DR2. In the middle, it shows the centre of the galaxy, and the Magellanic Clouds are visible down right in the map.

Table 3.1: The mean wavelength of the Gaia DR2 bandpasses, in nanometers.

filter	G	G_{BP}	G_{RP}
wavelength	673 ± 440	532 ± 253	797 ± 296

billion stars in the catalogue. Table 3.1 lists the mean bandpass wavelength with full-width-half-maximum. From the different stellar parameters, the science team working with Gaia are able the estimate other types of stellar parameters. One of these stellar parameters is the extinction estimate, A_G (Brown et al. 2018).

3.1.1 Gaia DR2 extinction estimate

In the Gaia DR2 catalogue, there are columns with information of estimated extinction A_G and reddening $E(BP - RP)$ with lower, 16th percentile, and upper, 84th percentile, uncertainties for both parameters. The Gaia team calculate the extinction estimate using the equation,

$$M = G - 5\log_{10} r + 5 - A_G, \tag{3.1}$$

where r is the inverse of the parallax to the object, M is the absolute magnitude, and G is the apparent magnitude (Andrae et al., 2018).

The method the Gaia Collaboration used to estimate extinction only gives positive extinction, meaning the uncertainty of the extinction estimate is not Gaussian distributed. The uncertainties are due to the estimation of extinction using only parallaxes and wide optical bandpasses. The calculation method of extinction they use causes the estimated A_G, of a star to be degenerate with the effective temperature[1] of the star (Andrae et al. 2018).

[1]Effective temperature is the temperature of a Blackbody spectrum emitting the same amount of radiation as the star observed.

Berry et al. (2012) show it is possible to break the degeneracy between reddening and intrinsic colour by adding photometric data from a much shorter wavelength, under the condition of low error in the apparent magnitude and constant extinction curve, a fixed R_V. Since intrinsic colour is proportional to the effective temperature, this may break the degeneracy between A_G and effective temperature.

From Andrae et al. (2018) we expect an extinction distribution according to an exponential distribution around the galactic plane. For high latitudes $|b| > 50$ deg they found the mean extinction to be 0.3 mag with a standard deviation of $\sqrt{\langle A_G^2 \rangle} = 0.46$mag. They argue, where the true extinction is zero for high latitude stars, the non-zero estimate of A_G is noise. We treat the standard deviation as a global uncertainty, applying on all extinction estimates of Gaia DR2. There is a factor 2 between the extinction estimate and the reddening estimate $E(BP - RP)$ both in magnitude and global uncertainty.

To estimate extinction with better uncertainties, one needs to include information given by other observations, or one may only include stars of one spectral type, like giant stars. The distribution of the vast number of stars in Gaia DR2 covers many spectral classes (Andrae et al. 2018). Andrae et al. (2018) points out, even though there are significant uncertainties in the estimated extinction, the estimations are not biased, and we can use the extinction estimation in ensembles, rather than by looking at a few stars. They test this ensemble theory by looking at stars at high galactic latitudes where the expected extinction is close to zero for close sources. The G-band of Gaia is a very broad bandpass observing at an optical wavelength around 550 nm. By including IR extinction data to increase the precision of the extinction estimation, the relevance to thermal dust emission will increase.

3.1.2 Extinction mapping

There are several ways of mapping the interstellar extinction. Previous studies have mapped the extinction through the galactic disc up to 8 kpc, within latitudes $|b| < 10^\circ$ or parts of the galactic disc. The galactic disc has more structures and clouds than the regions over and under the disc. These studies include both maps and line-of-sight profiles (Drimmel, Cabrera-Lavers and López-Corredoira, 2003; Marshall et al., 2006; Schultheis et al., 2014; Chen et al., 2018). The newest studies include all latitudes since ISM structures are within close distances, 100 to 300 pc, around the Solar System, known as the Local Bubble (Cox and Anderson, 1982). Most of these studied combine data from several catalogues of stellar data to get satisfying results. Gaia DR2 provides the most accurate stellar distance estimates so far, improving the mapping of ISM structures on the location of the clouds. The studies of Lallement et al. (2019), Green et al. (2019) and Leike and Enßlin (2019) use this new information to map the interstellar extinction to high precision. The method most of these studies use the differential extinction/reddening (units: mag per

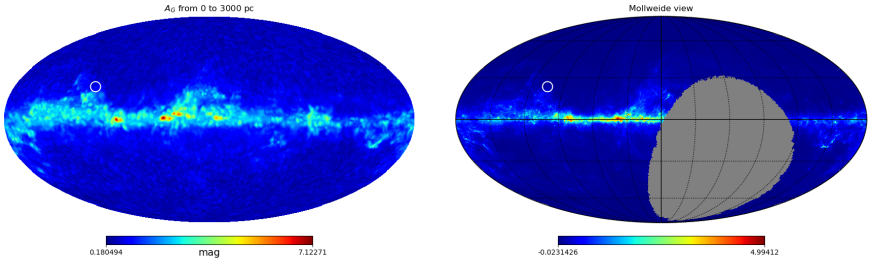

(a) $A_G(r = 3000)$ (b) $E(B - V)$

Figure 3.2: The left figure shows an extinction map, A_G, produced from Gaia data for stars up to 3000 pc. The right plot shows a reddening map, $E(B - V)$ [mag], up to infinity from Green et al. (2019). The white ring in both maps marks the observation area of RoboPol used in this thesis.

parsec) and integrate over distance. From the integration, we obtain line-of-sight profiles, together with maps showing where there is much extinction. Figure 3.2a show the extinction at 1500 pc produced from Gaia DR2 extinction estimates.

Zucker et al. (2019) uses a different method to get a line-of-sight extinction estimate, treating the dust clouds as screens, this means the line-of-sight extinction profile as a function of distance behaves as a step function. The method Zucker et al. (2019) use, gives the distance to the clouds along each sightline and can be extended to the number of clouds. Another approach is finding the number of clouds in a sightline using cloud velocities, under the assumption of different clouds have different velocities in each line of sight (Panopoulou et al., 2019).

3.2 Green et al. 2019 data

Green et al. (2019), from now Green19, provide a 3D map of stars containing position, distance and reddening of stars up to ∼60 kpc for three-quarters of the entire sky. They generate an input catalogue by combining photometry of Pan-STARRS 1 and 2MASS[2] and the distances from Gaia DR2 giving them 799 million sources. The extinction maps provided from Greens19 give good insight and reliability to the extinction maps created from Gaia DR2.

Figure 3.2b show the total reddening map produced by Green19, where the grey patch is the area of the sky not observed. And figure 3.2a show the total extinction up to 1500 pc from Gaia DR2. The data Green19 use are available at doi:10.7910/DVN/2EJ9TX for the maps and the catalogue of stellar parameters doi:10.7910/DVN/AV9GXO. Green19 provide a table for values of $R(V)$ to convert the reddening data to extinction; obtaining the

[2]This publication makes use of data products from the Two Micron All-Sky Survey, which is a joint project of the University of Massachusetts and the Infrared Processing and Analysis Center/California Institute of Technology, funded by the National Aeronautics and Space Administration and the National Science Foundation.

Table 3.2: The tabulated extinction vector $\vec{R}$ from (Green19). The first row is the name of the passbands of Pan-STARRS and 2MASS. The second row shows the mean transmission wavelengths, λ_T, of Pan-STARRS 1 and 2MASS in wavelength [μm]. The third row shows the values converting reddening to extinction which are unit-less.

	Pan-STARRS 1					2MASS		
filter	g	r	i	z	y	J	H	K_s
λ_T	0.481	0.617	0.752	0.866	0.962	1.25	1.65	2.16
$R(V)$	3.518	2.617	1.971	1.549	1.263	0.7927	0.469	0.3026

values from calculating, $R_V = (A_\infty - A_V)/E_{B-V}$, (Krügel, 2009) and by the ratio between reddening of the different passbands used in Green19.

3.2.1 Pan-STARRS 1

Panoramic-Survey Telescope And Rapid Response System is a 1.8m optical and near-infrared telescope at Hawaii. It maps stars at declination larger than $\delta \geq -30\,\text{deg}$, giving three-quarters of the total sky (Stubbs et al. 2010). The telescope has five filters, *grizy*, and table 3.2 lists their effective transmission wavelengths (Tonry et al. 2012).

3.2.2 2MASS - Two-Micron All-Sky Survey

This experiment comprises two telescopes, one in Arizona and one in Chile, observing in near-infrared. The telescopes have three filters, J, H and K_s, table 3.2 lists the mean transmission frequency of the bands. Green19 make use of the "high-reliability catalogue" to avoid contaminated sources. 2MASS is a full-sky survey and contain $\sim$ 500 million stars and galaxies (Skrutskie et al. 2006).

3.3 The Planck satellite

The European Space Agency (ESA) launched the Planck satellite in May 2009, and the satellite surveyed the sky from the second Lagrange point (L2) between 2009 and 2013. The satellite has 74 detectors observing at frequencies from $\sim$25 to $\sim$1000 GHz simultaneously. The angular resolution varies from $\sim$30 arc-minutes for low frequencies to $\sim$5 arc-minutes for high frequencies. There are two groups of detectors, Low-Frequency Instrument (LFI) observing at 30, 44 and 70 GHz and High-Frequency Instrument (HFI) observing at 100, 143, 217, 353, 545 and 857 GHz. Planck scanned the full sky twice per year with high sensitivity, angular resolution and frequency coverage (Planck Collab. I, 2011).

The main goal of the Planck satellite was to measure the spatial fluctuations of the temperature of the CMB at high accuracy given by fundamental astrophysical limits, and extract all information of the temperature fluctuation of the CMB and map the polarisation of the

CMB anisotropies. The Planck satellite also probed properties of the Milky Way and Extragalactic sources contaminating the CMB signal. The foreground information gives a good knowledge of inter-/extragalactic astrophysics (Planck Collab. I, 2011). The data produced by Planck have given astrophysicists highly accurate constraints on astrophysical and cosmological parameters.

In this analysis, we mainly use the official Planck data from press release 3, available at Planck Legacy Archive (PLA), http://pla.esac.esa.int/pla/#home.

3.4 RoboPol

The primary goal of RoboPol[3] is to measure the linear polarisation in optical for over 100 gamma-ray blazars to test models for jet-structures, composition, magnetic fields and emission mechanism. Further, the instrument measures the linear polarisation in optical of stars and thus trace the interstellar dust clouds. The instrument has an uncertainty below 0.1% in fractional linear polarisation and observing at a wavelength, $\lambda = 640.7$ nm, i.e. the R-band on the Johnson-Cusine photometric system for passbands (Bessell, 2005; King et al. 2014; Ramaprakash et al. 2019).

The RoboPol team have provided us with tomographic data containing polarisation data of 715 stars at $l \sim (103, 105)^\circ$ and $b \sim (21, 23)^\circ$ in galactic coordinates. In figure 3.2, we show the area of the sky the RoboPol data are from in a white circle on an extinction estimate map Gaia and reddening map from Green19. For visualisation purpose, the ring is larger than the area observed. RoboPol measures the starlight polarisation on the northern hemisphere, while the stellar polarisation data used by Planck Collab.XII (2018) from Berdyugin et al. (2014), provide a catalogue of polarisation data from stars at high galactic latitudes on both south and north cap.

3.4.1 Pasiphae

Pasiphae (Polar-Areas Stellar Imagine in Polarisation High Accuracy Experiment) is a research project focusing on the polarisation of stellar light from both the northern and southern hemisphere and away from the galactic disc. The goal of the mission is the make tomographic maps of the magnetic field of the Milky Way, by measuring the polarisation of millions of stars. The Pasiphae experiment uses the new developed WALOP instrument to measure the polarisation in optical at high accuracy. The observation will take place in the South African Astronomical Observatory in Sutherland, South Africa and at the Skinakas Observatory in Crete, Greece. In preparing the method and calibration of models, the Pasiphae team have been using the RoboPol polarimeter at the Skinakas Observatory.

As described in chapter 1, optical polarisation for stars with known distances can trace dust emitting polarised microwaves, and this is a good measure of making the magnetic field map between the stars, as long as the

[3] website (http://www.robopol.org/,2020)

stars are approximately on the same sightline. To get the distances to the stars, Pasiphae makes use of the distances measured by the Gaia mission. A map of the magnetic field in the Milky Way is vital to know, considering the removal of the polarisation foreground effects of the CMB, such map will also have a significant impact on other astrophysical research in the galaxy (Tassis, 2018).

In future work, the resulting observations of Pasiphae will provide starlight polarisation for regions of diffuse ISM, giving latitudes away from the galactic plane. The results will make a significant impact on the 3D modelling of the ISM around the galactic disc and map the magnetic field of the Milky Way at high precision.

In this thesis, we focus on the ISM, and what effects it has on photons travelling through it. Small particles of dust absorb photons and re-emits them at a lower frequency, so by looking at the absorption of stellar light from nearby stars ($r < 3$ kpc), we can make three-dimensional maps of the dust in the ISM. There are several ways to map the ISM from absorption, previous studies have combined astrometric data from the Gaia satellite with spectroscopic measures from 2MASS/APOGEE/Pan-STARRS/WISE experiments to simulate the dust distribution in our nearby interstellar neighbourhood (Drimmel et al., 2003; Marshall et al. 2006; Schultheis et al., 2014; Chen et al. 2013, 2018; Lallement et al., 2013, 2018, 2019; Green et al. 2018, 2019), while Leike and Enßlin (2019) only used the data from Gaia data release 2 (Gaia DR2). Gaia DR2 contains more than just the astrometric data of 1.69 billion stars. It also contains estimates of astrophysical properties like effective temperature, T_{eff}, line-of-sight extinction, A_G, and reddening, $E(BP - RP)$. The two later uses the photometric measures Gaia also provide (Brown et al., 2018).

Another feature of the ISM is its ability to polarise the light passing through it. The dust particles reduces the intensity according to the asymmetry and alignment of the dust grains, which polarise the photons. Studies of radiation from the ISM, show polarisation from both starlight and thermal emission from the dust particles. Polarisation is an active field in astrophysics giving information on the magnetic field of the Milky Way, mass distribution, star formation and extinction properties. In cosmology, the ISM contaminates the cosmological signal, such that much work goes into separating the cosmological signals from other sources.

Chapter 4

Statistics

Using the knowledge we have of the microwave sky and the ISM components behaviour together with the data received from telescopes, we may apply different statistical method to analyse the ISM. The Planck team uses Bayesian statistics to separate the different foreground components using methods involving Markov Chain Monte Carlo simulations. Each of the different foreground components depend on several parameters giving multidimensional equations to solve. In this chapter, we will describe the theory behind the methods used to solve complex problems such as component separation, including a short explanation of Bayesian statistics and Markov Chain Monte Carlo simulation, with a description of the Metropolis-Hastings algorithm and the Gibbs sampler.

4.1 Bayesian Statistics

Bayesian statistics contain three vital properties, the prior, the likelihood and the posterior. Bayes' theorem goes as,

$$P(x|y) = \frac{P(y|x)P(x)}{P(y)}, \tag{4.1}$$

where on the right-hand side, $P(x)$ is the prior, i.e. the knowledge we have of the parameters in the model, meaning what probability distribution describes the knowledge before observations. The next property, $P(y|x)$, is the likelihood-function, describing the probability of the data given the parameters. $P(y)$ is the evidence and is the probability of observing y. In general, the evidence is constant regarding the parameters and only considered when comparing models with different parameter-space. The left-hand side, $P(x|y)$, is the posterior distribution which is the combination of the prior and likelihood and describes the updated knowledge from observations and prior knowledge. Bayes theorem describes the probability of an event x occurring based on the prior knowledge of relevant information of x and y. Bayesian statistics give the probability of the null hypothesis from the samples and prior information. The parameters in the probability distributions are unknown, and therefore

random. Each parameter has an uncertainty reflecting the probability distribution $P(x, y)$ (van de Schoot et al. 2013).

In statistics, the marginal distribution is the integral over x for the distribution of $P(x, y)$. The integral reduces the distribution to a function of only y,

$$P(y) = \int P(x, y)dx. \tag{4.2}$$

The conditional distribution describes the probability of finding x given a specific value of y in the distribution of $P(x, y)$, which defines the conditional distribution as,

$$P(x|y) = \frac{P(x, y)}{\int P(x, y)dx} = \frac{P(x, y)}{P(y)}. \tag{4.3}$$

A marginal distribution from the priors can describe each parameter, and a conditional distribution gives the parameter distribution given the observations (van de Schoot et al. 2013). From the $P(x, y)$ and $P(y, x)$, which is equal, and using the conditional distribution definition, deducing Bayes' theorem is straightforward,

$$P(x, y) = P(y, x) \implies P(x|y)P(y) = P(y|x)P(x) \tag{4.4}$$

$$P(x|y) = \frac{P(y|x)P(x)}{P(y)}, \tag{4.5}$$

where $P(x|y)$ is the posterior distribution giving the probability of observing y if x is true. $P(y|x)$ is the probability of observing x if y is true and is the likelihood $\mathcal{L}(x)$, $P(x)$ is the probability of observing x. The evidence $P(y)$ is independent of x and act as a constant (Planck Collab. X, 2016), thus,

$$P(x|y) \propto \mathcal{L}(x)P(x). \tag{4.6}$$

Further, the handiness comes clear when setting x to contain multiple parameters forming a parameter vector and y to contain, for example, data received from measurements.

In many cases, we model the data, $\mathbf{d}$, as the sum of the actual signal, $\mathbf{s}$, and some noise, $\mathbf{n}$,

$$\mathbf{d} = \mathbf{s}(x) + \mathbf{n}, \tag{4.7}$$

with $\mathbf{s}(x)$ as the wanted quantity. We find an expression for the likelihood by flipping around the terms in equation (4.7) to get the noise term by it self, $\mathbf{n} = \mathbf{d} - \mathbf{s}(x)$. By assuming Gaussian distributed noise, we express the likelihood as a product of the data points, i,

$$\mathcal{L}(x) \propto \prod_i \exp\left\{-\frac{1}{2}((\mathbf{d_i} - \mathbf{s}_i(x))^T C_i^{-1}(\mathbf{d_i} - \mathbf{s}_i(x))\right\}, \tag{4.8}$$

where C is the covariance matrix from the noise. A general expression for the prior can be more difficult to enlist, but under an assumption of

Gaussian distributed signal with a covariance matrix C_S, a possible prior is:

$$P(\mathbf{a}) = \frac{1}{\sqrt{|C_S|}} \exp\left\{ -\frac{1}{2}\mathbf{a}^T C_S^{-1} \mathbf{a} \right\}, \tag{4.9}$$

where $\mathbf{a}$ is the amplitude of the signal.

In the next sections, we outline methods of using Bayesian statistics to solve complex problems.

4.2 Markov Chain Monte Carlo

Markov Chain Monte Carlo (MCMC) is a general way of simulating a stochastic process where the probability distribution is known up to a proportionality constant (Geyer, 1992). MCMC is a method used when the computational cost of brute force computation is high. For example, in computing complex integrals by drawing random numbers from the probability distribution describing the properties of the problem. A Markov Chain is a sequence of random numbers, X_i, generated from a transition probability only dependent on the current value of the random number; Let X_i be a randomly drawn number, if the transition probability, $P(i,j) = P(X_i \to X_{i+1})$, only depend on X_i,

$$P(i,j) = \Pr(X_{i+1} = x_j | X_i = x_i), \tag{4.10}$$

we have a Markov process. Thus the knowledge needed to get to the next state is only the current state of the random variable, and the transition probability is independent of the earlier random number, $X_{j<i}$ (Walsh, 2004). In a Markov Chain, the transition probability is, in general, not known. We can solve this problem by expressing the transition probability W as the product of two probabilities, the acceptance probability, A, of doing the proposed move from state i to state $i+1$ and the probability for making the transition, T, to state $i+1$ form state i (Hjort-Jensen, 2015). Expressing this mathematically as

$$W(i \to i+1) = T(i \to i+1)A(i \to i+1). \tag{4.11}$$

There are several ways of sampling in an MCMC environment. In natural science, researchers may encounter complex problems with many free parameters. For the simpler cases, straightforward calculations may work, but with increasing numbers of parameters the computational cost grows, such that alternative methods, using statistics, become more relevant. One of these alternative methods is the Metropolis-Hastings algorithm in the MCMC library. The algorithm is widely used in data science but has its limitations when the joint conditional distribution is unknown (Walsh, 2004). In this situation, the Gibbs sampler becomes relevant and use conditional distributions for each parameter, instead of the high dimensional joint-distribution. In the two next paragraphs, we outline the widely used sampling algorithms, Metropolis-Hastings algorithm and the Gibbs sampler.

4.2.1 The Metropolis Hastings algorithm

The Metropolis-Hastings algorithm is used when the probability distribution $p(x) = f(x)/K$ is complex, where K may be unknown, and $f(x)$ is a function of x describing the distribution. From our knowledge of MCMC, if the transition of moving from state x_i to state x_{i+1} is given by the probability distribution $T(x_i \rightarrow x_{i+1}) = t(x_i, x_{i+1})$, where $t(a, b) \neq t(b, a)$ is the proposal probability of moving from a to b. Then the algorithm goes as:

1. Initialise x_0 by drawing a sample to satisfy $f(x) > 0$.
2. Draw proposal parameter x^* from the proposal distribution $t(a, b)$ to make a move given the value of $a = x_0$.
3. Calculate the ratio between the probability distribution given proposal x^* and the current state, x_i,

$$\alpha = \frac{f(x^*)t(x^*, x_i)}{f(x_i)t(x_i, x^*)}. \tag{4.12}$$

4. If the move increases the density such that $\alpha > 1$, the proposal is accepted, $x_{i+1} = x^*$ and return to step 2. If the move decrease the density, $\alpha < 1$, then accept x^* with a probability α, else reject the proposal and use the current value $x_{i+1} = x_i$, then return to step 2.

The acceptance probability for a proposal is then,

$$\alpha = \min\left(\frac{f(x^*)t(x^*, x_i)}{f(x_i)t(x_i, x^*)}, 1\right). \tag{4.13}$$

It is normal not to store the first samples since the sampling has not converged yet; this is called the burn-in period (Walsh, 2004).

4.2.2 The Gibbs sampler

The Gibbs sampler is one of many sampling algorithms using random numbers to estimates complicated systems. This technique generates random variables from marginal distributions indirectly, with no calculation of densities. From the conditional distribution, marginal distributions may be derived using their definitions: $P(x|y) = P(x, y)/P(y)$[1] and $P(y) = \int P(x, y)dx$[2]. Bayesian statistics and likelihood calculations often relies on the Gibbs sampler to evaluate difficult calculations to get the posterior distributions. In a calculation of the multi-dimensional $f(x)$, the Gibbs sampler generate samples, $X_1, ..., X_m \sim f(x)$, only from the knowledge of the parameter, x. For a large enough sample, we calculate the mean, the variance and other properties of $f(x)$ to the desired accuracy. The usefulness of the Gibbs sampler increases as the number of variables increase, and this is because it allows us to replace a multi-dimensional function

[1] Conditional distribution
[2] Marginal distribution

by independent single-dimension random variables (Casella and George, 1992).

For example, to solve a complex three-dimensional problem $P(X, Y, Z)$ with the parameters X, Y, Z, with the distribution of $P(X, Y, Z)$ not known, the conditional distributions $P(X|Y, Z)$, $P(Y|X, Z)$ and $P(Z|X, Y)$ are often known. The iteration over each parameter is cyclic: $P(X|Y, Z)$, $P(Y|X, Z)$ and $P(Z|X, Y)$. Iterating i steps gives the sample points,

$$\begin{aligned} X_{i+1} &\sim P(x|Y_i, Z_i) \\ Y_{i+1} &\sim P(y|X_{i+1}, Z_i) \\ Z_{i+1} &\sim P(z|X_{i+1}, Y_{i+1}). \end{aligned} \tag{4.14}$$

The Gibbs-steps above means that while finding a value form the probability distribution of a parameter X_{i+1}, holding the other parameters fixed of the last iteration value, therefore in the estimation of Y_{i+1}, we use the $i + 1$ iteration of X and the ith iteration of Z is used (Casella and George, 1992).

In Metropolis-Hastings the transition probability between θ_{i+1} to θ_i is not symmetric, $T(\theta_{i+1}|\theta_i) \neq T(\theta_i|\theta_{i+1})$. The transition probability for x of the two parameters $\{x, y\}$, for the case of Gibbs sampling, is given as,

$$T(x_{i+1}|y_i) = P(x_{i+1}|y_i)\delta(y_{i+1} - y_i), \tag{4.15}$$

where δ is the Dirac-δ function. We calculate the acceptance probability α from equation (4.13) by inserting equation (4.15) and use,

$$f(x^*) = P(x_{i+1}|y_{i+1}), \qquad f(x_i) = P(x_i|y_i), \tag{4.16}$$

$$t(x^*, x_i) = T(x_i|y_{i+1}), \qquad t(x_i, x^*) = T(x_{i+1}|y_i). \tag{4.17}$$

The Dirac-δ functions transforms $y_{i+1} \to y_i$. Using the definition of the conditional distribution, eq. (4.3), give the final expression,

$$\alpha = \frac{P(x_{i+1}|y_i)P(y_i)P(x_i|y_i)}{P(x_i|y_i)P(y_i)P(x_{i+1}|y_i)} \equiv 1. \tag{4.18}$$

The last trick also helps with degenerate joint parameters, since the Gibbs sampler mismanages degenerate and correlated parameters. The relation in eq. (4.18), show the proposal is always accepted in Gibbs-sampling. By first sampling over y from its marginal distribution and then x from the corresponding conditional distribution, a joint sample may be accepted (BeyondPlanck I, InPrep).

PART II

The Method

Chapter 5

3D Extinction estimation from Gaia DR2

The ISM distribution surrounds us in every direction. Observations of radiation coming from inside and outside the ISM require knowledge of its properties. One feature of the ISM is its ability to absorb light from stars and other sources. As we know from chapter 1, mapping how the extinction of light depends on the structure and composition of the ISM is vital to estimate the optical depth to re-ionisation. To explore the extinction of light travelling through the ISM, we will outline how to make three-dimensional maps of extinction from the data provided by Gaia DR2. The first section discusses the inversion of parallax angles into physical distances, based on (Luri et al. (2018)). The second section outline creation of the extinction maps and handling uncertainties. In the third section, we discuss line-of-sight extinction and comparison with Green19 extinction estimate. Furthermore, the fourth section describes how to model extinction and compare with the intensity from the foreground components, thermal dust and CO line emission.

5.1 Distance estimation

To estimate the distance to the stars in Gaia DR2, we transform the parallax angle, ϖ, to distance, r, by inverting the parallax angle, given in milli-arcseconds,

$$r = \frac{1}{\varpi_{true}}. \tag{5.1}$$

This distance is the correct distance to the star if the parallax angle is the true parallax angle, ϖ_{true}. However, we need to handle the conversion of the parallax angle with care, e.g. some parallax angles in Gaia DR2 are negative, which leads to negative distances. Negative distances are unphysical and removed from our analysis, most of these are quasars with a parallax angle close to zero where the uncertainty in the measurement gives a negative number (Luri et al. 2018). Including the systematic

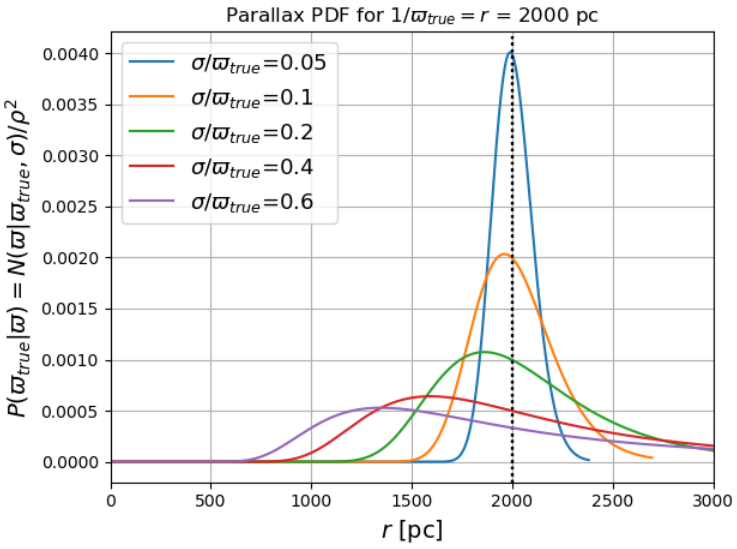

Figure 5.1: The PDF for parallax plotted as a function of distance r for different uncertainties. The dotted black line is the true distance, $r = 1/\varpi_{true}$. The curves are the estimated distance to the stars following equation (5.3).

measurement errors described by a Gaussian probability distribution around the true parallax, the observed parallax is then,

$$p(\varpi|\varpi_{true}) = \frac{1}{\sqrt{2\pi}\sigma_\varpi} \exp\left\{\left[-\frac{(\varpi - \varpi_{true})^2}{2\sigma_\varpi^2}\right]\right\}, \tag{5.2}$$

where ϖ is the observed parallax, and σ_ϖ is the uncertainty of the observed parallax. Then we estimate a probability distribution function (PDF) for the estimated distance $d = 1/\varpi$ from equation (5.2) (Luri et al. 2018), where,

$$\begin{aligned} p(d|\varpi_{true}) &= p(\varpi = 1/d|\varpi_{true}) \cdot \left|\frac{\mathrm{d}\varpi}{\mathrm{d}d}\right| \\ &= \frac{1}{\sigma_\varpi d^2\sqrt{2\pi}} \exp\left\{\left[-\frac{(1/d - \varpi_{true})^2}{2\sigma_\varpi^2}\right]\right\}. \end{aligned} \tag{5.3}$$

The PDF of the observed distance is anti-symmetric since the denominator is proportional to d^{-2}, eq. (5.3), and for a growing fractional uncertainty, the most probable observed distance shifts to smaller distances. Large fractional uncertainties highly underestimated the observed distance, which is far from the true distance. When estimating the parallax, large uncertainties can cause negative parallaxes, and thus negative distances. We use this estimation to set a limit on the fractional uncertainty in the parallax angle, σ_ϖ/ϖ. In figure 5.1 we see how the probability distribution function in (5.3) behave for different uncertainties. The estimated distance from Gaia DR2 represents the peak of the curve in figure 5.1. It is clear from figure 5.1 the measured parallax angles underestimate the distance. From the calibration of the telescope aboard Gaia, there is a zero-point correction

on the parallax estimates. Even when correcting for the known zero-point of -0.029 mas, Gaia DR2 underestimates the distance to the stars (Luri et al. 2018). Using the information provided in Luri et al. (2018) and figure 5.1, the more considerable fractional uncertainties increase the difference between estimated distance and the actual distance. Estimation of the correct distance to a star would rely on, for example, sampling algorithms.

5.1.1 Inversion of parallax angle and star selection

Since distances from parallaxes often give large uncertainties, we only use stars with a positive parallax angle, $\varpi > 0$, and fractional parallax, $\sigma_\varpi/\varpi < 0.2$, to have the most correct distance estimates. The limit on fraction parallax is to use stars with good distance estimates but still have a large sample of data. To estimate the distance, d, to the stars from Gaia DR2 parallax angles, ϖ, we invert the angles and correcting for zero-point,

$$d = \frac{1}{(\varpi - zp)}, \tag{5.4}$$

where $zp = -0.029$ mas is the zero-point of the parallax angles measured in milli-arcseconds. The inversion of parallax angles underestimates the distance since there are errors to the observed parallax angle, giving an anti-symmetry to the distribution defining the observed parallax when converted to distance (Luri et al. 2018). From figure 5.1 it is clear we limit the star selection from fractional uncertainties to be below, $\sigma_\varpi/\varpi < 0.2$, following the usage of (Lallement et at. 2019).

To select the stars, we follow the star selection of Lallement et al. (2019), the star must have an extinction allocated to it and choosing stars with magnitude in the G band of $G < 18$, this is to avoid background subtraction since faint stars may blend more into the background. The selection gives $\sim$ 64 million stars to work with, where $\sim$ 60 million stars are within 3000 pc.

5.2 Map making

There are multiple ways of creating maps of the galactic extinction from dust particles. One way is to use the pixel coordinates of the stars at different distances using distance intervals. Then find which stars a pixel, p, contains at the current distance interval, and evaluate the mean extinction, $\langle A \rangle_G$, in the pixel,

$$\langle A_G(p,d) \rangle = \frac{1}{N^\star} \sum_i^{N^\star} A_G^i(p,d), \tag{5.5}$$

where $N^\star$ is the number of stars in the pixel of the distance interval, d. Figure 5.2 illustrate this idea for pixel i at distance interval j, where the stars of pixel i, j is located in volume i, j. We evaluate the stars in the volumes given by the pixel size and distance interval j. Another way is to look at the angular sectors of the sky and divide each sector into boxes over

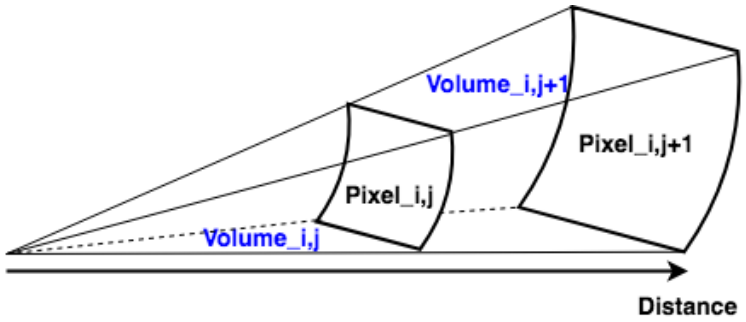

Figure 5.2: Illustration on how pixel size change with distance. The subscript, i, is the pixel number, and, j, the distance interval.

distance, then calculate the mean extinction in each sector. A third way is to create cubes in Euclidian coordinates of a given size and then calculate the mean extinction in each cube. We use the first method described in this paragraph.

We work in galactic HEALPix coordinates (Gorski et al. 2010), where the galactic plane defines the equator of the sky maps when mapping the positions of the stars. Gaia DR2 provides the galactic coordinates, longitude and latitude, and the equatorial coordinates, right ascension and declination for the position coordinates. In HEALPix coordinates the latitudes starts at the north pole and increase southwards, $\theta \in [0, \pi]$, while the IAU standards goes out from the equator with, $\theta_{IAU} \in [-\pi/2, \pi/2]$, and increase toward the north. The conversion between the two is, $\theta = \pi/2 - \theta_{IAU}$.

We divide the stars into 31 bins of size 100 pc, from 0 pc to 3000 pc and one for star over 3000 pc. For each pixel, we evaluate the mean extinction of the stars in the different distance intervals, with $N_{side} = 128$. For bins, without stars, the estimated means are sett to zero. We calculate the mean distance of the stars in the bins similarly as extinction. To reduce noise, we smooth each map layer to two degrees, see appendix A.3. Then the differential extinction is calculated between the bins by subtracting bin j from bin $j+1$,

$$\Delta A_G^i = \begin{cases} \langle A_G \rangle^{j+1} - \langle A_G \rangle^j \\ 0, \qquad\qquad \text{for } \langle A_G \rangle^j > \langle A_G \rangle^{j+1}, \end{cases} \tag{5.6}$$

where $N_i = N_j - 1$. The differential extinction show where new structures in the ISM forms. From Lallement et al. (2019), the main contribution of differential extinction is up to $\sim$ 2000 pc, with some extensions in different directions. We calculate the cumulative extinction over a distance range from ΔA_G, and sum up the differential extinction for every 300th pc up to 3000 pc. The integration goes as,

$$A_G(a \to b) = \sum_{i=a}^{b} \Delta A_G^i, \tag{5.7}$$

where a and b as the distance bins the integration goes over, when summing

over ΔA_G^i. This gives ten maps, in addition, we make one map for the total extinction.

5.2.1 Uncertainties

So far, we have not considered the uncertainties of the map values in the calculation. To make a good line-of-sight model for extinction, we included the uncertainties in the modelling.

We calculate the uncertainties of the extinction in each bin by describing the data in each bin as the function, $U(A_{G,i}) = A_{G,i}$, where i is the stars in the bin. The error of the extinction in a bin is (Ku, 1966),

$$\sigma_U = \sqrt{\sum_i^N \left(\frac{\partial U}{\partial A_{G,i}} \sigma_{A_{G,i}} \right)^2}, \tag{5.8}$$

where $\sigma_{A_{G,i}}$ is the extinction error of each extinction estimate and N is the numbers of stars in a bin. Since we defined $U(A_{G,i}) = A_{G,i}$ we are left with,

$$\sigma_U = \sqrt{\sum_i^N \left(\frac{1}{N} \sigma_{A_{G,i}} \right)^2} = \frac{1}{N} \sqrt{\sum_i^N \sigma_{A_{G,i}}^2}. \tag{5.9}$$

Since the extinction estimate from Gaia DR2 comes with upper and lower percentiles, we calculate the σ_U for both percentiles.

5.3 Line-of-sight extinction

Line-of-sight extinction is how much extinction there is as a function of distance for a sightline, $A_G(r)$. The extinction in a line-of-sight can not decrease with increasing distance, because the further away the source is, the more dust there is in the line-of-sight. However, the additional amount of dust can be close to zero in the sightline, keeping the extinction as a function of distance constant. We want to make a model describing the extinction in each sightline, giving $A_G(r) \rightarrow A_G(r)_{\theta,\phi}$. Here θ and ϕ is the latitude and longitude giving the direction of the sightline. The extinction model, as a function of distance, should monotonously increase.

We find the extinction in a sightline by dividing the stars into distance intervals and then calculate the mean extinction and distance in each distance bin. We use sightlines of size 5×5 degrees for the number of stars in each bin to be high and reduce noise. Figure 5.3 show the line-of-sight extinction for eight longitudes, $l = \{45, 90, 135, 180, 225, 270, 315, 360\}^\circ$, with each plot show five different latitudes, $b = \{10, 45, 90, 135, 170\}^\circ$ in HEALPix coordinates. From the plots in figure 5.3, we see the data points at high latitudes, $b = \{10, 45, 135, 170\}$, are consistently around 0.3 mag and below the global uncertainty of 0.46 mag up to distances of 2000 pc. This follows the conclusion Andrae et al. (2018) regarding extinction at high latitudes, which is pure noise. The high latitude points show the noise in the extinction estimate by the irregular behaviour in amplitude while for larger distances the data points are spreading out.

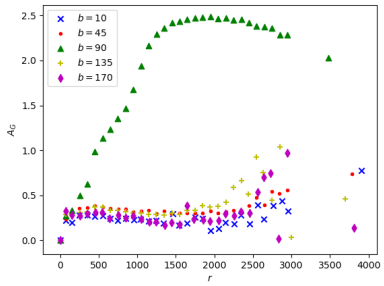

(a) Longitude 45°

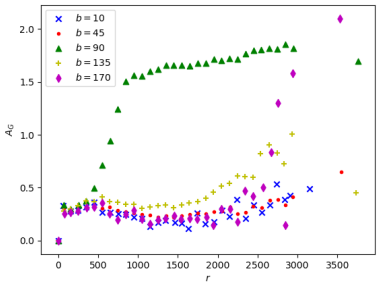

(b) Longitude 90°

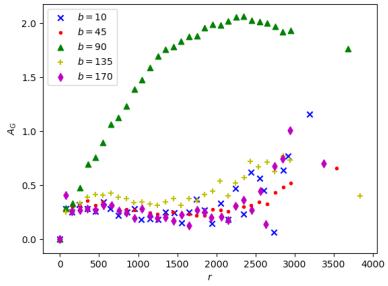

(c) Longitude 135°

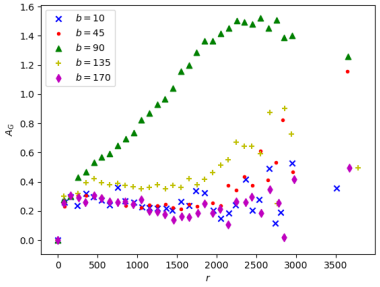

(d) Longitude 180°

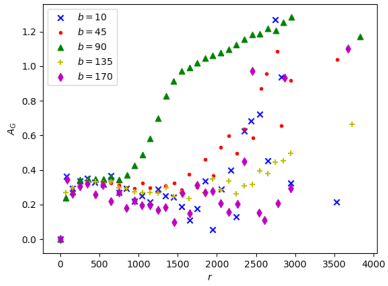

(e) Longitude 225°

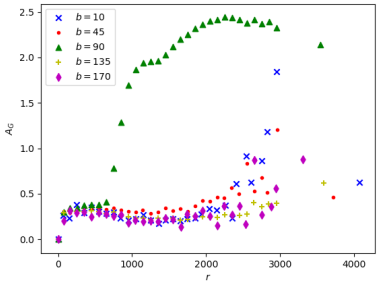

(f) Longitude 270°

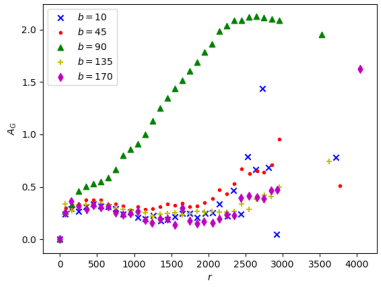

(g) Longitude 315°

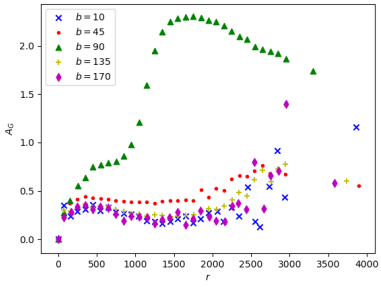

(h) Longitude 360°

Figure 5.3: The mean extinction $\langle A \rangle_G$ per distance bin for different sightlines using Gaia DR2 values. Each plot is for different longitudinal direction for every 45°. The colour code and marker code is for the different latitudinal direction of $b = \{10, 45, 90, 135, 170\}^\circ$ where 90° degrees is the galactic plane. Each sight line is of 5×5 degrees.

Table 5.1: List of the line-of-sight coordinates, in HEALPix and IAU (in parentheses) convention, used when comparing extinction estimates from Gaia DR2 and Green19.

l [$\circ$]	45	90	135	180	225
b [$\circ$]	70 (-20)	70 (-20)	70 (-20)	70 (-20)	70 (-20)
b [$\circ$]	90 (0)	90 (0)	90 (0)	90 (0)	90 (0)
b [$\circ$]	110 (20)	110 (20)	110 (20)	110 (20)	110 (20)

5.3.1 Comparing with Green19

To check for consistency with similar studies, we compare the extinction estimates from Gaia DR2 with the results of Green19. Their maps are for celestial latitudes larger than $b_{cel} > -30^{\circ}$. We will focus on the comparison for the celestial northern hemisphere, using sightlines with galactic HEALPix coordinates. Table 5.1 lists the coordinates. We avoid the centre of the Galaxy, since the missing values from the Green19 maps affect the large sightlines, see figure 3.2b. Following their procedure in calculating the median of the given reddening samples provided in their map file, we find the line-of-sight reddening and convert the reddening to extinction following equation 5 in Green19,

$$\vec{A}_V(E) = \vec{R}(V)E(B-V), \tag{5.10}$$

where the values of $\vec{R}$ are given in table 1 of Green19 and here in table 3.2.

Now that we have established methods for creating maps and line-of-sight profiles of extinction estimates, we will further create a model for the extinction estimates as a function of distance. Then we compare our extinction model with thermal dust and CO line emission.

5.4 Modelling extinction

To model the extinction in a sightline, we need a function of distance to describe it. By looking at the plots in figure 5.3, we tried to fit polynomials to the points, but they diverged at large distances, thus a power-law according to, $f(x) = a + bx^c$, fit better to most sightlines in general, where a, b and c are free parameters. SciPy has a function `curve_fit`, which is suitable for this task (Virtanen et al. 2020). We use a low resolution, $N_{side} = 16$ since the computation time of the power-law estimation is high. We fit this power law to the line-of-sight extinction profiles of A_G to make interpolated maps of the extinction at every distance up to R_{max}. The computation of line-of-sight extinction is similar to the interpolated extinction maps, together with the mean distance of the stars. The data points range from $r = 0$ to $r = R_{max}$. As default we set $R_{max} = 3$ kpc, since the extinction estimates of Gaia DR2 for $R_{max} > 3$ kpc are less good, the data points differ a lot even at high latitudes. The extinction should flatten

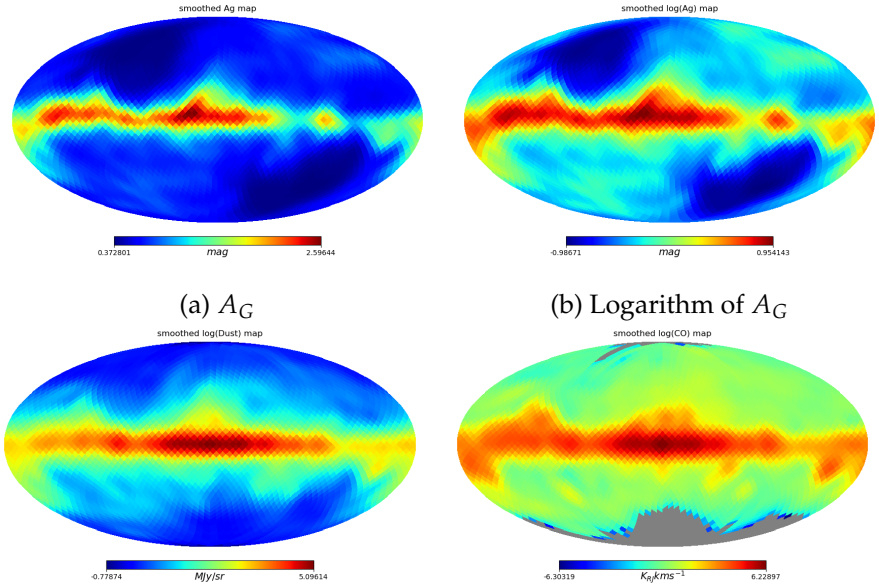

(a) A_G

(b) Logarithm of A_G

(c) Logarithm of dust intensity

(d) Logarithm of CO intensity

Figure 5.4: (5.4a)Interpolated extinction map of A_G up to distance $r = 3000$ pc. (5.4b) The logarithm of interpolated A_G. (5.4c) The dust map of Planck on logarithmic scale. (5.4d) CO line emission of Planck seen at logarithmic scale. All the maps have resolution, $N_{side} = 16$ and smoothed to FWHM$= 10^\circ$.

out when reaching low-density areas since no more dust is contributing to the extinction of light.

5.4.1 Comparing with dust and CO maps of Planck

From the adapted extinction functions, we make maps using the interpolated extinction values at a distance of 3000 pc from the sun and compare with the 857 GHz Planck dust map (Planck Collaboration). We choose these components from the foregrounds since thermal dust emission and extinction of starlight may come from the same particles (Martin, 2007; Planck Collab. XI, 2014), and CO line emission because it is strong in the same regions as dust emission (Planck Collab. XIII, 2014).

In the comparison, we first make sure the maps have the same N_{side}, in this case, $N_{side} = 16$, then smooth the maps to 10° resolution. The smoothing reduces the noise by taking the average over more data points. The low N_{side} resolution is because of time cost in the computation of the interpolated extinction map. The computation time is $\sim 1/10$ second per pixel and the total computation time increase by a factor four for each N_{side} level. In figure 5.4 shows the smoothed maps, with the two upper maps showing the interpolation of $A_G(r \leq 3000\text{pc})$ both on linear (5.4a) and logarithmic (5.4b) scale, while the two lower plots show the dust intensity (5.4c) and CO line intensity (5.4d) on a logarithmic scale. To see how correlated the two pair of maps are, we calculate the Pearson correlation

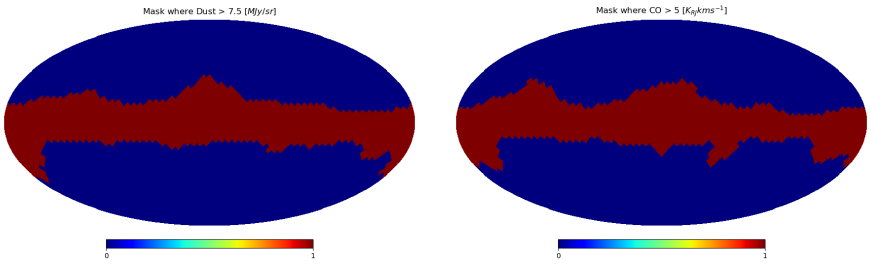

(a) Where dust $> y_{lim} = 7.5$ MJy/sr (b) Where CO $> y_{lim} = 5\mathrm{K_{RJ}km/s}$

Figure 5.5: The areas of the sky where $y > y_{max}$ in dark red for dust (left) and CO (right).

coefficients using NumPy's `corrcoef` (Oliphant, 2006) function between A_G and dust, and A_G and CO.

We investigate the relationship between extinction and the two component-maps further by first create scatter plots of the component maps, both thermal dust and CO, with the extinction map to visualise how correlated they are, and then fit a line to the data points. We use Numpy's `polyfit` function to find the best fit line, which use a least-squares method to estimate the best fit line (Oliphant, 2006). The data points distribution in the scatter plots are in a way such that two lines describe the relationship between the extinction and the components in a satisfying way. With one line for the lower values of the components and one line for the upper values of the components. We describe this model as,

$$f(x) = \begin{cases} b_1 + a_1 x, & \text{if} y \leq y_{lim} \\ b_2 + a_2 x, & \text{if} y > y_{lim}, \end{cases} \tag{5.11}$$

where $f(x)$ is the line describing the data points, b_i is the zeroth-order coefficients of the polynomial, a_i is the first-order coefficients, y is the data point values in the scatterplot and y_{lim} is the value giving model 1 or 2. We use the value $y_{lim} = 7.5$ for thermal dust and $y_{lim} = 5$ for CO. We need the a_i coefficients to scale the extinction to the components since we want to find the residuals of the two maps.

$$r = M_{comp} - \alpha M_{A_G}, \tag{5.12}$$

where $\alpha = \{a_1, a_2\}$ and the subscript, $comp$, denotes either dust or CO. By including the two-line model into the maps, we compare the maps using equation 5.12, giving residual maps between A_G and the two components. Figure 5.5 show the areas in the sky where $y > y_{lim}$ in dark red for dust, to the left, and CO, to the right. We see the red areas cover the galactic plane since this is where the emission is most energetic.

Chapter 6

Comparison of visual and submillimeter polarisation from Robopol and Planck 353 GHz map

Optical starlight polarisation is a product of extinction of light when a beam hits aspherical dust grains in the ISM, removing more light parallel to the long axis than on the short axis of the grain. On the other hand, polarised thermal emission from heated dust particles emits more radiation on the long axis. Combining observations of both optical and infrared radiation provides a robust tracer on the ISM and magnetic field distribution in the galaxy. In this chapter, we outline our analysis of polarisation data from RoboPol and Planck. The analysis includes treatment of polarisation data like coordinate transformations, possible biases and robustness, then look at the correlation between optical and submillimeter polarisation. We also look into the line-of-sight extinction estimates in the observation area of RoboPol. Further, we use this knowledge to estimate the spectral index of polarised dust emission.

The data we use in the analysis is for a limited part of the sky. From the RoboPol experiment, we have polarisation data within a $1.5^\circ \times 1.5^\circ$ area in the sky coming in equatorial coordinates. From Panopoulou et al. (2019) there should be a cloud around 360 pc, and the stars at closer distances are not significantly polarised or intrinsically polarised. We remove these stars from the data set together with stars with strange polarisation angle. Since polarisation is coordinate dependent, we start with the transformation from celestial to galactic coordinates. Together with the polarisation maps provided by the Planck team, we can look for correlations in the area RoboPol observed. Further, we look for similarities with the results of Planck Collab. XII, 2018 where they found good correlations using star data of Berduygin et al. (2014). In their work, they used 1505 stars covering the full the sky at $b_{IAU} > 30^\circ$ in the northern hemisphere and $b_{IAU} < -59^\circ$ in the southern hemisphere. They found a ratio between P and p_v to be

$R_{P/p} = 5.42 \pm 0.05$MJy/sr, this is consistent with the earlier work of Planck Collab. Int. XXI, (2015) which used star from different catalogues giving $R_{P/p_v} = 5.4 \pm 0.5$MJy/sr. We compare the starlight polarisation with the 353 GHz frequency map of Planck Collaboration[1]. We describe how to debias polarisation data from different distances and resolutions. Then we estimate the spectral index of a modified blackbody from the thermal dust model.

6.1 Coordinate transformation of starlight polarisation

The data from RoboPol comes in celestial coordinates while we work in galactic coordinates, and thus we rotate the stellar coordinates into galactic. The package `Astropy.coordinates` provide tools for rotation of the positioning of the stars in the sky (Astropy Community, 2020). Since polarisation angles are defined relative to the meridians and depends on the polar axis of the coordinate system, we rotate the polarisation angles manually (Hutsemékers, 1998). Rotation of the star position does not rotate the polarisation into the new coordinate system. In the conversion from celestial coordinates to galactic coordinates, we need to consider the north galactic pole, ngp, as a reference pole in celestial coordinates. We compute the rotation, using equation 16 in Hutsemékers, (1998),

$$\tan\left(\theta - \theta_{gal}\right) = \frac{\sin\left(\alpha_{ngp} - \alpha\right)}{\tan\delta_{ngp}\cos\delta - \sin\delta\cos\left(\alpha_{ngp} - \alpha\right)}, \tag{6.1}$$

where θ_{gal} is the polarisation angle in the new (galactic) coordinate frame, θ is the polarisation angle in the equatorial coordinate frame and α, δ is the right ascension and declination angles of the objects. The coordinates to the north galactic pole in equatorial coordinates is $\alpha_{ngp} = 122.932^\circ$ and $\delta_{ngp} = 27.128^\circ$. The next step to solve (6.1) is to use the two-argument arctangents function and then solve for $\theta_G = \arctan 2(X, Y)$ where X is the nominator and Y is the denominator in (6.1).

To convert the fractional polarisation from equatorial to galactic coordinates, we use only one rotation of the Stokes parameters between the two reference frames. First, we define $a = 2(\theta - \theta_{gal})$ given from (6.1), then compute,

$$q_{gal} = q\cos a - u\sin a, \tag{6.2}$$

$$u_{gal} = q\sin a + u\cos a, \tag{6.3}$$

where q, u are in equatorial coordinates, and q_{gal}, u_{gal} are in the IAU convention. In a HEALPix system the coordinate vector points from observer to the source while in an IAU system the coordinate vector points from the source to the observer in a right-handed system (Gorski et al.

[1]The Planck maps are found at the Planck Legacy Archive: http://pla.esac.esa.int/pla/#home

2010). Thus, we multiply u_{gal} by -1, since we work in HEALPix convention. The uncertainties of q and u must also be rotated to galactic coordinates. We calculate the uncertainties of q_{gal} and u_{gal} using the relations,

$$\sigma_{q_{gal}} = \sqrt{\sigma_p^2 \sin^2(2\theta_{gal}) + 4p^2\sigma_{\theta_{gal}}^2 \cos^2(2\theta_{gal})}, \tag{6.4}$$

$$\sigma_{u_{gal}} = \sqrt{\sigma_p^2 \cos^2(2\theta_{gal}) + 4p^2\sigma_{\theta_{gal}}^2 \sin^2(2\theta_{gal})}, \tag{6.5}$$

which can be derived from the length of changes in the fractional Stokes parameters, $|\delta q| = |\delta p \sin(2\theta)|$ and $|\delta u| = |\delta p \sin(2\theta)|$.

We check if the conversion to galactic coordinates is correct by computing the ratio between the polarisation angles from the Planck's Stokes parameters Q_s, U_s, and the starlight polarisation fractions $q_{gal} = q_v, u_{gal} = u_v$. The subscript denotes "submillimeter" for s and "visual" for v. The ratio is,

$$\Delta\psi_{s/v} = \arctan\left[(U_s q_v - Q_s u_v), -(Q_s q_v + U_s u_v)\right]. \tag{6.6}$$

In the ideal case, $\Delta\psi_{s/v} = 0$, giving $\psi_s \perp \psi_v$ (Martin, 2007). In this case, and when computing equation (6.1), we use numerically the `arctan2` function in NumPy to get the right quadrant (Oliphant, 2006).

6.2 Correlation

To better understand the connection between polarisation of stellar light and the polarisation observed in the Planck 353 GHz map, we compare the stellar polarisation data of RoboPol with the 353 GHz frequency map of Planck Collab. (2015). And further with polarisation maps from the data processing schemes NPIPE 353 GHz map (Thomessen, 2019, BeyondPlanck, InPrep.) and Sroll2 353 GHz map (Planck Collab. III 2018). The way we did this is by first localise where on the sky the tomography data are on a full-sky map since it is covering about three square degrees on the northern hemisphere. Then find which pixels represent this area of the sky in galactic HEALPix coordinates. For each pixel containing data, we compute the weighted mean of the polarisation in each non-empty pixels,

$$\langle p \rangle = \frac{\sum pw}{\sum w}, \qquad \text{where } w = \frac{1}{\sigma_p}, \tag{6.7}$$

where w is the weights computed from the uncertainties, and similar for q and u. The weighted error in the mean is,

$$\sigma^2_{\langle p \rangle} = \frac{n}{(n-1)(\sum w)^2}\left[A + B + C\right], \tag{6.8}$$

$$A = \sum (wp - \bar{w}\langle p \rangle)^2, \tag{6.9}$$

$$B = -2\langle p \rangle \sum [(w - \bar{w})(wp - \bar{w}\langle p \rangle)], \tag{6.10}$$

$$C = \langle p \rangle^2 \sum (w - \bar{w})^2, \tag{6.11}$$

where $\bar{w}$ is the mean of the weights (Gatz and Smith, 1995).

By storing the non-empty pixels, we apply the same pixels to the 353GHz map and only use these pixels in further analysis. Since there is noise in the maps, we smooth to a resolution of 10 arc-minutes, see appendix A.3 for the smoothing method. This smoothing makes the polarisation pattern come forth in the maps.

We compare the two maps by calculating the Pearson correlation coefficient and the ratio between P_s and p_v. The correlation between the two maps is easiest to find by making a scatter plot between the two maps data points and simultaneously calculate the Pearson correlation coefficients of the comparing maps. We use the `corrcoef` function of NumPy to calculate the correlation (Oliphant, 2006).

For the ratio, eq. (2.7) described in section 2.3.1, we calculate the mean of the ratio and the standard deviation of the P_s/p_v map, in units of MJy/sr. Such that,

$$\left\langle R_{P/p} \right\rangle = \left\langle \frac{\sqrt{Q_s^2 + U_s^2}}{\sqrt{q_v^2 + u_v^2}} \right\rangle, \tag{6.12}$$

and using NumPy's functions `mean` and `std` for the mean value and standard deviation (Oliphant, 2006).

6.2.1 Goodness of fit

For further consistency check we, compute a linear fit, $y = ax + b$, by minimising a χ^2 test on the joint data $(Q_s, U_s), (q_v, u_v)$ and on each of the Stokes parameters individually Q_s vs q_v and U_s vs. u_v. These methods estimates the slope of the scatter plots and describe the same property as the ratio $R_{P/p}$. The calculation of the minimised χ^2 follow the method given in Planck Collab. Int. (2015),

$$\chi^2(a,b) = \sum_i^{N_{obs}} V(a,b) M(a,b)^{-1} V(a,b)^T, \tag{6.13}$$

where N_{obs} is the numbers of observations. We give the vector and matrix, V and M as,

$$V_{P/p}(a,b) = [Q_s - aq_v - b, U_s - au_v - b], \tag{6.14}$$

and,

$$M_{P/p}(a,b) = \begin{bmatrix} C_{QQ} + a^2\sigma_q^2 & C_{QU} \\ C_{QU} & C_{UU} + a^2\sigma_u^2 \end{bmatrix}. \tag{6.15}$$

The matrix elements of M is given by the covariance matrix elements of C_{ij} from Planck and uncertainties of the stellar data given as σ_i for $i = \{q, u\}$. The covariance matrix element C_{QU}, C_{QQ} and C_{UU} of the full maps of Planck, is then,

$$C_{QU} = \sigma_Q \sigma_U, \tag{6.16}$$

$$C_{QQ} = \sigma_Q^2, \tag{6.17}$$

$$C_{UU} = \sigma_U^2. \tag{6.18}$$

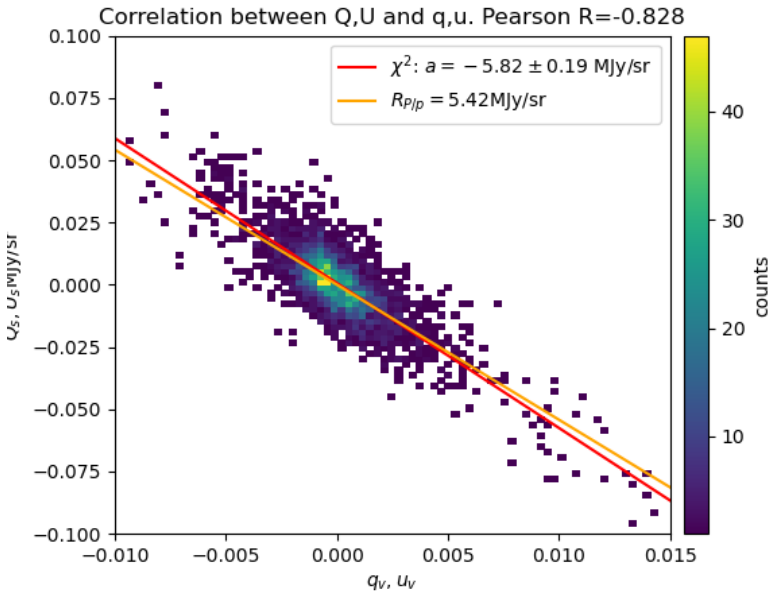

Figure 6.1: Biased reproduction of figure 23a in Planck Collab. XII (2018). The primary features are still visible with a maximum count at (0,0). The red line represents the best fit line using linear regression and the green line using the best fit of χ^2-test. The reduces $\chi^2/n = 0.013$ causing an over-fit to the green line. We have not included error bars since they are highly biased.

To compute the χ^2, we invert the matrix M numerically in Python using the NumPy function `linalg.inv`. Since the elements in M are arrays and M has the shape (2,n,2), we calculate the inverse of M^T, giving shape (2,2,n), and then transpose back, $((M^T)^{-1})^T$ (Oliphant, 2006). Further, we use the fmin_powell minimisation function provided by the SciPy package to compute the minimised χ^2 and get the parameters a, b, based on Powell's method (Virtanen, 2019). To check if our calculations are correct, we try to reproduce figure 23a in Planck Collab. XII (2018), using the 10 arcmin smoothed IQU map of Planck together with the stellar polarisation data provided by Berduygin (2014). We only use stars with distances greater than 200 pc to remove intrinsically polarised stars and with $\Delta\psi_{s/v} < 45°$.

6.3 Debiasing polarisation data

In this section, we describe biasing effects on the polarisation data and how to correct for the bias. Figure 6.1 show my reproduction of figure 23a in Planck Collab. XII (2018), we see a 2D histogram with the density of data points. Further, we see the slopes of the minimised χ^2 and linear regression are steeper than 5.42MJy/sr. Meaning our reproduction is biased. A possible bias here is the averaging of the polarisation values in each pixel, for pixels containing several stars with different distances shifts the mean

polarisation either to the left or right depending on the variance of the contributions of different stars.

From Planck Collab. XII (2018) there are mainly two things to do when debiasing polarisation. Planck observations project polarisation onto a 2D screen with imprints covering all distances up to far outside the galaxy while the starlight polarisation is the distance to the star and thus within our stellar neighbourhood. The difference in distance causes a bias when comparing the two polarisation sources. To correct for this, one can transform the starlight polarisation too far away by multiplying by a correction factor, $R^{\infty/\star}$, given by the extinctions to the star and up to a distance where there is no more additional extinction,

$$R^{\infty/\star} = \frac{E(B-V)^{\infty}}{E(B-V)^{\star}} = \frac{A_V^{\infty}}{A_V^{\star}}, \tag{6.19}$$

where the numerator is the reddening of a source infinitely far away, and the denominator is the reddening of the star. For stars above a certain distance away, this ratio goes to unity. This give,

$$q_v^{\infty} = q_v R^{\infty/\star}, \tag{6.20}$$

$$u_v^{\infty} = u_v R^{\infty/\star}, \tag{6.21}$$

and similarly for their uncertainties, $\sigma_{q_v}, \sigma_{u_v}$. This correction factor is assuming a uniform ISM distribution.

We correct for extinction on the starlight polarisation by multiplying q_v and u_v by equation 6.19, under the assumption on uniform dust distribution between the star and the background. From the reddening map of Green19, we produce a map with 153 sightlines within the RoboPol region. Since there is a considerable variation in extinction at distances less than 1000 pc, we interpolate the extinction map to get more data-points. Then we assign each sightline to the stellar polarisation data such that each star gets an extinction value. Because of the limited number of sightlines, this only gives an approximation of the stellar extinction value.

6.3.1 Line of sight extinction in RoboPol sky-area

To get a deeper understanding of where the polarisation happens, we create line-of-sight extinction profiles for the RoboPol area. The extinction profiles is interesting because of the connection between starlight polarisation and extinction and give knowledge of correcting polarisation data by extinction. Since the latitude of RoboPol data is above the galactic disc and the primary structures of the galaxy, as shown in figure 3.2a, the estimated $\langle A_G \rangle$ from Gaia DR2 will be too noisy, such that we use the estimated extinction from Green19. We create the extinction profiles as described in section 5.3 and calculate the line-of-sight extinction in the same part of the sky as RoboPol observe. We set the boundaries of the area to be $l = 104.102^{\circ} \pm 0.75^{\circ}, b = 22.225^{\circ} \pm 0.75^{\circ}$ and divide the area into four squared subsections. In contrast, from the previous line-of-sight extinction profiles, we use narrower sightlines to look for variations in the area. Each

sight line has a side-length of 0.75°.

A second correction factor goes on the beam since the observing beam of the telescope is much larger than a point source. This means the polarisation of Planck is depolarised from the averaging in the beam and correct the bias by multiplying with, $\sqrt{1 + \delta p^2_{beam}/p^2}$, where $\delta p^2_{beam} \approx 63.9 \langle S \times p \rangle^2_\omega$ and S is the polarisation angle dispersion function. The same factor applies to the uncertainties and Q, U and their uncertainties (Planck Collab. XII, 2018). Since we smooth the stellar polarisation data to the same resolution as the smoothing of the Planck data, ten arcminutes, we neglect the beam depolarisation.

The linear polarisations P_s and p_v are biased parameters since they are strictly positive, $p = \sqrt{q^2 + u^2} > 0$. A way of correct this bias is to apply a modified asymptotic (MAS) estimator (Plaszczynski et al. 2014),

$$p_0 = p - \sigma_p^2 \frac{1 - e^{-p^2/\sigma_p^2}}{2\sigma}, \tag{6.22}$$

where p_0 is the corrected polarisation and σ_p is the uncertainty of p,

$$p = \sqrt{\frac{q^2\sigma_q^2 + u^2\sigma_u^2}{q^2 + u^2}}. \tag{6.23}$$

The bias in p_v and P_s affects all properties involving them, such as the uncertainties σ_q and σ_u. The bias becomes significant for small signal-to-noise ratios. We correct p_v and P_s using the MAS estimator.

6.3.2 Robustness of correlation in the polarisation data

Systematic effects on the calibration of the polarimeters used in the surveys may bias the data. We add rotations from 0° to 90° to the polarisation angle when computing the Stokes parameters to check for systematics. If the correlation coefficient is best at no rotation, the calibration is robust. A rotation of 90 degrees should reproduce the Stokes parameters with an opposite sign, e.g. $Q(+0^\circ) = -Q(+90^\circ)$, the notation $+n^\circ$ notes the rotation. Figure 7.13, show the behaviour of rotating the optical polarisation up to 90°.

6.4 The spectral index in the thermal dust model

From our establishment of the correlation between starlight polarisation and polarised dust emission, we can explore physical properties in the current dust model. One of the free parameters in the modified blackbody model describing the SED of thermal dust is the spectral index, β_d, given in equation 2.6. Studies focusing on polarised foreground emission have found the spectral index to be $\beta_d^P = 1.59 \pm 0.02$ (Planck Collab. XVII, 2014), and the newer result of Planck Collab. XI (2018) $\beta_d^P = 1.53 \pm 0.02$ for large parts of the sky. To constrain the value of β_d in a smaller part

of the sky using a different approach with stellar polarisation will help to constrain the complexity of the ISM. We investigate the spectral index from a template using visual polarisation data and calculate the spectral index for polarised thermal dust. To estimate the spectral index, we need to compare different frequency bands using the passbands 143, 217 and 353 GHz of Planck. The polarisation maps from Planck are the polarisation from all sources, which must be corrected for to get the polarisation of thermal dust. Both CMB and thermal dust are significantly polarised at frequencies higher than 100 GHz, which means we need to subtract the CMB polarisation map, M_{CMB}, from the total polarisation, M_{tot}, $M_d = M_{tot} - M_{CMB}$. The polarisation of the CMB highly biases the 143 and 217 GHz polarisation maps. Furthermore, the CMB also give contributions to the 353 GHz maps.

We create a template with $N_{side} = 2048$ to calculate the spectral index of a modified blackbody model, as described in equation (2.5). The template should use starlight polarisation to estimate the intensity of submillimeter polarisation. From Planck Collab. Int. XXI (2015) we have,

$$D^{pol} = \begin{cases} -R_{P/p} q_v = Q_{temp}, & \text{for } pol = Q \\ -R_{P/p} u_v = U_{temp}, & \text{for } pol = U. \end{cases} \tag{6.24}$$

The orthogonality between submillimeter and visual polarisation gives the extra minus sign, e.g. $\sin(x + \pi) = -\sin x$, for $x = 2\psi_v$ and $x + \pi = 2\psi_s$. We use equation (6.24) as the template. Further, we calculate the residuals between the observation data for three frequencies, 143, 217 and 353 GHz, M_ν^{pol}, and the template in 353 GHz, D^{pol}, using,

$$\min(g(\alpha)) = \min \sum \frac{(M_\nu^{pol} - \alpha D^{pol})^2}{|M_\nu^{pol}|^2}, \tag{6.25}$$

where the minimising factor α is of further importance, and the superscript pol stands for the Stokes parameters. We compute the template in the 353 GHz bandpass, and set this frequency as reference, ν_0. Using the minimising factors $\alpha_{\nu_i}^Q$ and $\alpha_{\nu_i}^U$ and the bandpass frequencies, $\nu = \{143, 217, 353\}$ GHz, we calculate the spectral index of dust SED. We describe the SED of dust as a power law of frequency as described thoroughly in equation (2.5). The following paragraphs describe more in detail the derivation steps, first for a power law, then for the model given in equation (2.5).

By following a similar approach as Fuskeland et al. (2018), using thermal dust instead of synchrotron radiation, we derive an expression for the spectral index of the simple form, $S_\nu \propto \nu^\beta$. Further, we use the notation $\alpha_i = \alpha_{\nu_i}^{pol}$. Assuming a perfect minimisation times the template D^{pol} equals an amplitude A the relative frequency $(\nu/\nu_0)^\beta$, we have,

$$\alpha_\nu \times D^{pol} = A \left(\frac{\nu}{\nu_0} \right)^\beta, \tag{6.26}$$

for $\nu = \{143, 217, 353\}$ GHz. Then rearrange such that the template and amplitude A are on the same side,

$$\frac{D^{pol}}{A} = \frac{1}{\alpha_\nu} \left(\frac{\nu}{\nu_0} \right)^\beta, \tag{6.27}$$

since the left-hand side is independent of frequency band, the following relation is valid,

$$\frac{1}{\alpha_{353}} \left(\frac{\nu_{353}}{\nu_0} \right)^\beta = \frac{1}{\alpha_{217}} \left(\frac{\nu_{217}}{\nu_0} \right)^\beta = \frac{1}{\alpha_{143}} \left(\frac{\nu_{143}}{\nu_0} \right)^\beta. \tag{6.28}$$

From this relation, we get an expression for β, by taking the logarithm and solve for β. To convert between K_{CMB} and K_{RJ} units, we use the a2t-factor,

$$g(x)|_{T=T_{CMB}} = (e^x - 1)^2 / x^2 e^x, \tag{6.29}$$

where $T_{CMB} = 2.7255$ K and x is the same as in eq. (2.3). We divide α by equation (6.29) defining, $a = \alpha / g(x)$, and gives,

$$\beta = \frac{\log a_\nu / a_{353})}{\log (\nu / 353)}, \qquad \nu = \{143, 217, 353\}. \tag{6.30}$$

We get for this power-law using Stokes U polarisation, $\beta = [1.46, 1.15]$ between the bands.

By multiplying the initial relationship eq. (6.26) with $(e_0^x - 1)/(e^x - 1)$ and extending the power-law to $\nu^{\beta+1}$, we get a modified blackbody model,

$$\alpha_\nu \times D = A \left(\frac{\nu}{\nu_0} \right)^{\beta+1} \frac{e^{x_0} - 1}{e^{x_\nu} - 1}, \tag{6.31}$$

with $x = h\nu / k_B T$. The temperature in the exponential factor is the dust temperature, $T_d = 19.6$ K (Planck Collab. XI 2014). When further divide by equation (6.29), we get a new expression for a_i,

$$a_\nu = \alpha_\nu (e^{x_\nu} - 1) / g(x_\nu). \tag{6.32}$$

By following the same derivation described above, we express the spectral index, β, as,

$$\beta = \frac{\log (a_\nu / a_{353})}{\nu / 353} - 1. \tag{6.33}$$

We compute the spectral index for each Stokes parameter, giving a subscript on β corresponding to the Stokes parameter.

We calculate the uncertainties of the different β by varying the Stokes parameters Q_s, U_s and q_v, u_v around their observation values. We first define $Q = \mathcal{N}(Q_s^{obs}, \sigma_{Q_s})$ and $Q = \mathcal{N}(U_s^{obs}, \sigma_{U_s})$ and draw thousand samples from these distributions. For each draw, we calculate the minimising factor α from equation 6.25 for each frequency map and Stokes parameter and calculate the spectral indices for Q and U polarisation. We calculate the standard deviation from the collection of spectral indices.

PART III

The Results

Chapter 7

Results of extinction and polarisation analysis

From the established methods described in the previous chapters, we present the results in the same order. First, we show the extinction maps of Gaia DR2 together and line-of-sight extinction profiles comparing Gaia DR2 with Green19 extinction estimates. Then a comparison between modelled extinction estimates and the ISM components, thermal dust and CO. In the second part, we present the results of comparing starlight polarisation with submillimeter polarisation of Planck. In the end, we show the spectral index of polarised dust emission calculated from polarisation in optical. We give a more thorough discussion of the results in chapter 9

7.1 Gaia Extinction estimation

In this section, we first show the integrated differential extinction maps, both the total map and ten maps covering the extinction at different distances. Second, we look at the line-of-sight extinction profiles for sightlines around the galactic plane comparing extinction data from Gaia DR2 and Green19. Lastly, we compare the modelled extinction estimate to thermal dust intensity and CO line intensity.

From the extinction estimates and the calculated differential extinction, we plot the cumulative differential extinction from 0 to 3000 pc, shown in figure 7.1. Toward the galactic centre in the middle of the map, regions with much extinction appears. In the left part of the map, a large fan is visible. The fan is known as the Fan region and is one of the most dominant polarisation structures in the full sky polarisation maps, and long thought to be at close distance, $d < 500$ pc (Hill et al. 2017). In the right part of the plot, there are two noticeable structures, one smaller cloud in the mid-right part and a broader part most right. The latter is an extension to the wide fan in the left part of the 2D plot. One notice that above, and below the galactic disc, there is little extinction. To investigate at what distances the location of ISM structures is, we need maps covering smaller distance intervals. The next maps show extinction from distance intervals covering

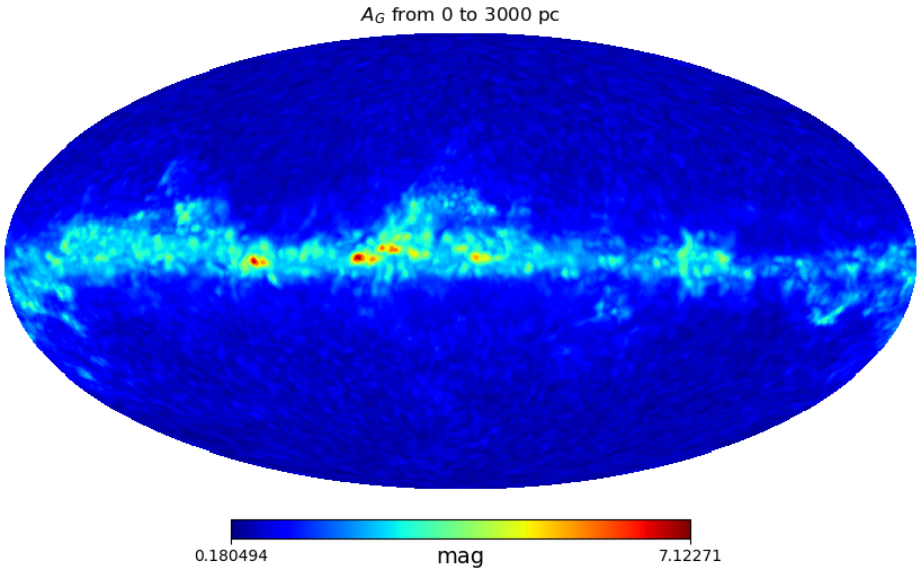

Figure 7.1: Cumulative A_G from 0 to 3000 pc, smoothed to 2 degrees. Structures from every distance is visible, with strong extinction areas in the middle toward the galactic centre and left in the map.

300 pc each up to 3000 pc. We neglect the extinction estimates at distances over 3000 pc since they are weak.

Figure 7.2 show the cumulative differential extinction over distance bins of size 300 pc. In the first map, 7.2a, we see structure toward the galactic centre and in the opposite direction, left in the map. The map visualises the global noise from Gaia DR2 extinction data of the close stars at all latitudes in light blue. When continuing to map 7.2b, the left structure stretches out to the right and higher latitudes while fewer clouds appear toward the galactic centre. We also see a strong pattern in the right part of the map, which is the Orion nebulae. In the next map from 600 to 900 pc, 7.2c, the location of extinction structures are along the centre of the galactic disc because at high latitudes we are outside the galactic disc. The fan left in the plot still get contributions. At 90 degrees to the right, a strong extinction structure appear. In map 7.2d, new structures occur toward the galactic centre. While the other structures fade away, the mid structure continues into the next map from 1200 to 1500 pc. At distances from 1500 to 2100 pc, map 7.2f and 7.2g, the maps contain more noise due to lower amplitude of A_G, but clear structures along the galactic plane materialise from map to map. The three last maps, 7.2h, 7.2i and 7.2j, show an increase in the maximum of extinction amplitude on the new structures emerging, which reduce the visible noise in the maps. The global noise of the extinction estimates of Gaia DR2 explains the noise at high latitudes in the large distance maps and the noise in the closest map. Because of the global noise, low extinction estimates, $A_G < 0.5$ mag, are highly uncertain, according to Andrae et al. (2018).

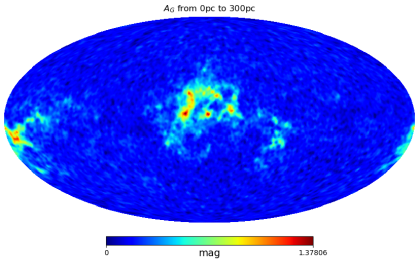

(a) ΔA_G from 0 to 300 pc

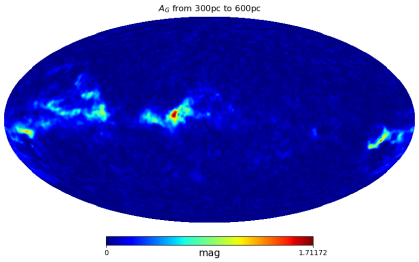

(b) ΔA_G from 300 to 600 pc

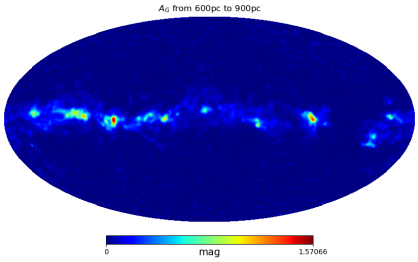

(c) ΔA_G from 600 to 900 pc

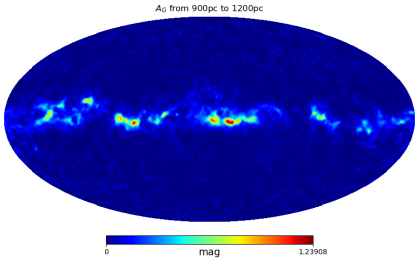

(d) ΔA_G from 900 to 1200 pc

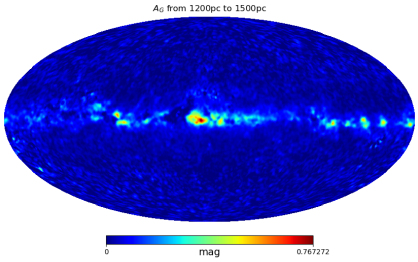

(e) ΔA_G from 1200 to 1500 pc

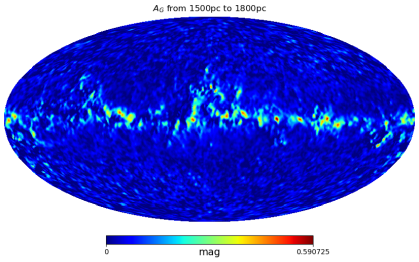

(f) ΔA_G from 1500 to 1800 pc

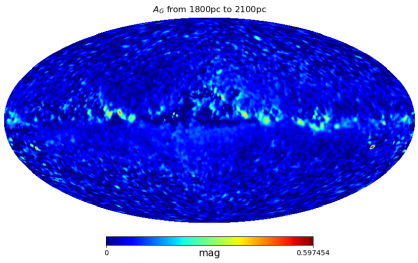

(g) ΔA_G from 1800 to 2100 pc

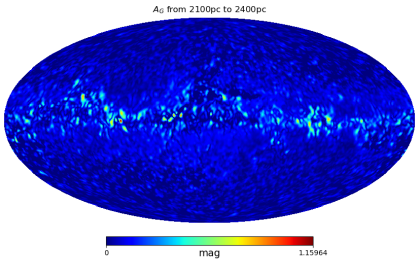

(h) ΔA_G from 2100 to 2400 pc

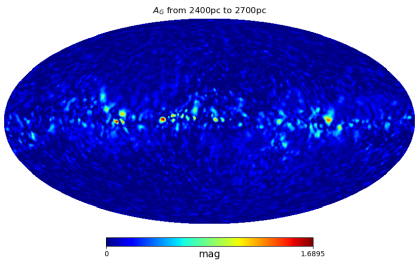

(i) ΔA_G from 2400 to 2700 pc

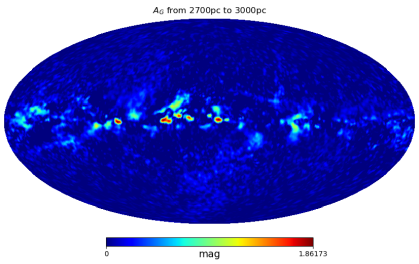

(j) ΔA_G from 2700 to 3000 pc

Figure 7.2: Sky maps of the estimated cumulative differential extinction A_G over ten distance intervals of 300 pc, from 0 pc to 3000 pc. The extinction in each pixel is the mean extinction of the stars in the current pixel at the current distance interval.

7.1.1 Comparing Gaia line-of-sight extinction with Green19

To verify the extinction estimates of Gaia, we compare the sightline profiles to the extinction estimates from Green19. Since Green19 provide reddening, we convert the reddening to extinction using table 3.2. Pan-STARRS' r-band is closest to the mean frequency of the G-band of Gaia DR2 and gives the best conversion from reddening to extinction similar to A_G when comparing with the magnitude of A_G. The conversion goes as $A_r = R(r)E = 2.617E$, and we use this relation when comparing extinction estimates of Gaia DR2 and Green19 in line-of-sight profiles. In figure 7.3, we see the line-of-sight extinction for three latitude angles around the galactic plane, $b = (70, 90, 110)^\circ$ for five different longitude angles, $l = (45, 90, 135, 180, 225)^\circ$. The solid lines are the line-of-sight extinction from Green19, and the points are the estimates of Gaia. There seems to be some connection between the two, but since we find the extinction of Green19 by multiplying with the conversion factor from table 3.2 there might be some difference. Figure 7.3f show the sightlines, marked as red circles, in the total extinction map (rotated 135 degrees to the right), used in the line-of-sight plots. The red circles are a little bigger than the sightline of 5sr with the coordinate angels located in the middle of the circle.

From our established maps and profiles showing structures of light-absorbing materials in the galaxy up to 3000 pc, it is time to look for connections between extinction and components of the ISM. We compare the extinction estimates with thermal dust emission the CO line emission.

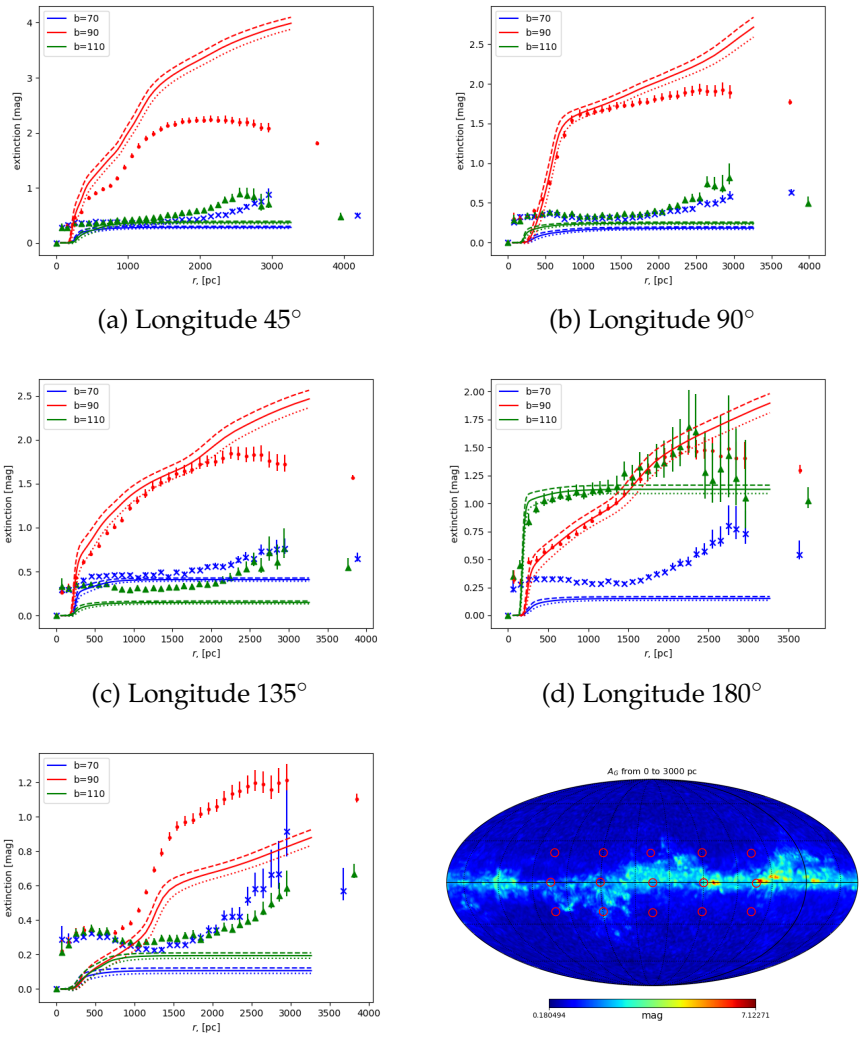

(a) Longitude 45°

(b) Longitude 90°

(c) Longitude 135°

(d) Longitude 180°

(e) Longitude 225°

(f) Marked map of the sightlines

Figure 7.3: The figures show line-of-sight extinction from Gaia estimates and Green19. The dots, with error bars, are the Gaia estimates, and the lines are the extinction estimates from Green19, where the solid line is the median value and the dashed lines are the 1σ error. The different colours correspond to different declination, $b = \{70, 90, 110\}^\circ$, counted from the north pole. Each figure represents one longitudinal direction, in steps of 45 degrees, $l = \{45, 90, 135, 180, 225\}$ degrees. The last plot (down right) show the total extinction map, rotated 135 degrees to the right, with the sightlines marked as red circles.

7.1.2 Comparing Gaia extinction estimate with 857 GHz dust intensity

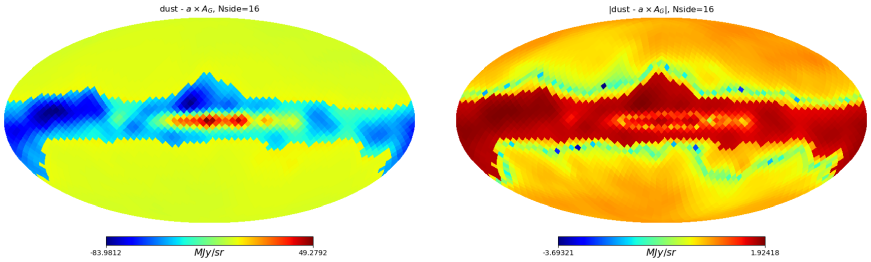

(a) Residual map of dust vs. A_G (b) Logarithm of absolute residuals

Figure 7.4: Residual map between dust and extinction, A_G, using a two-component residual model. The galactic disc is visible with strong negative values and positive values at the galactic centre. The large yellow parts of the galactic disc have values closer to zero. The positive values show where dust emission is strongest and negative values where A_G is strongest. The right plot shows the logarithm of the absolute value of the residuals, to highlight the areas of the galactic disc.

In the comparison between the interpolated extinction maps produced from the estimates of $A_G(r \leq 3000\text{pc})$ and the 857 GHz dust map of Planck using a two-component residual model, we get residual plots shown in figure 7.4. The left figure shows the residuals on a linear scale while the right plot show on a logarithmic scale with a resolution of $N_{side} = 16$ and smoothed to 10 degrees. We use the absolute values in the logarithmic plot to show variations on smaller scales and negative values. The Pearson correlation coefficient is $R = 0.81$ between the two maps. Figure 7.5, Show the correlation where we use three lines to fit the points, the black line gives the best-fit all points, and the green line for low dust values and the red line is the fit for the high dust values. Since the data points spread out for high values of A_G, we use two lines to fit the scatters. The minimising factors in the residual calculation are, $(a_0, a_1, a_2) = (38.266, 5.903, 49.63)[\text{MJy/sr/mag}]$. Where a_0 is for the full data sets, a_1 is for the lower part of the dust intensity ($y_{lim} \leq 7.5$ MJy/sr) and a_2 is for the higher values of the dust intensity. The figures show large variations in the difference between dust intensity and extinction in the galactic plane.

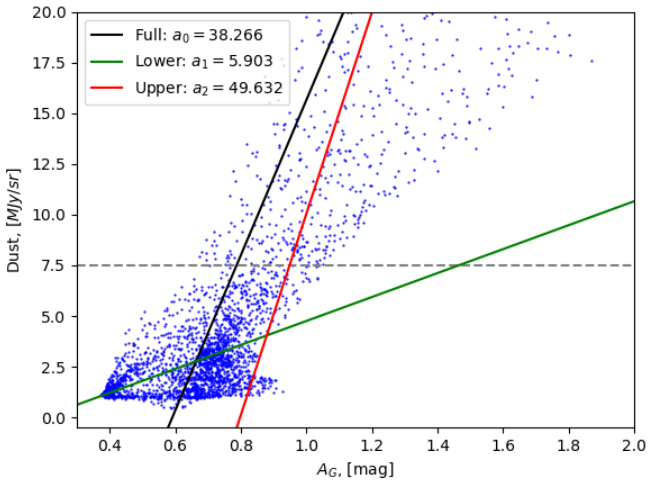

Figure 7.5: Correlation plot between A_G and dust smoothed to 10°. The red line is the best linear fit for values above $y_{lim} = 7.5$ for dust (dashed grey line), the green lines are for pixel values above y_{lim}, and the black line is for the full sets of data. The best-fit parameters for the slopes are for full, lower, upper lines: $a_0, a_1, a_2 = \{38.255, 5.903, 49.632\}$.

7.1.3 Comparing Gaia extinction estimate with CO intensity

Figure 7.6 shows the residuals when comparing CO line emission from Planck with the interpolated extinction model. The left plot is on linear scaling, and the right plot is on logarithmic scaling over absolute residuals. The Pearson correlations coefficient is $R = 0.71$ between the two comparing maps. The minimising factors are $(a_0, a_1, a_2) = (70.703, 3.708, 106.51)[\mathrm{K_{RJ}km/s/mag}]$, where a_0 is for all the data points, a_1 is for the lower part of the CO intensity ($y_{lim} \leq 5\mathrm{K_{RJ}km/s}$) and a_2 is for the higher values of the CO intensity. Figure 7.7 shows the correlation where the black line shows the best-fit line for all data, the red line is for the best-fit of high CO values and the green line is the best-fit for low values of the CO intensity. There are large variations in the difference between CO line emission intensity and extinction in the galactic plane, as seen in figure 7.6.

In the figures 7.5 and 7.7, we have zoomed in on the primary group of data points, such that the highest values disappear from the figures, and the fitted lines seem less good. For example, in figure 7.7, the line for the values above y_{lim} get contributions from data points not seen.

In the following section, we outline the results of the polarisation analysis between optical and submillimeter polarisation.

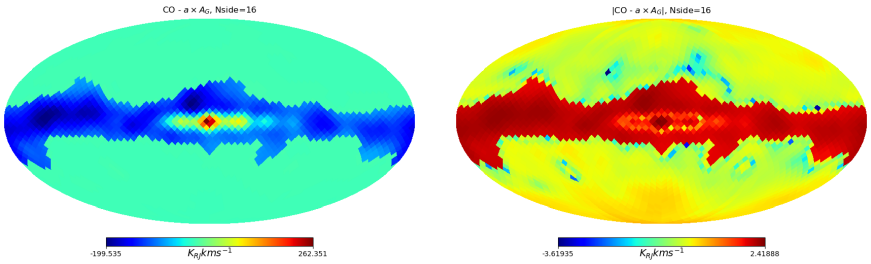

(a) Residual map of CO vs A_G (b) Logarithm of absolute residuals

Figure 7.6: Residual maps of CO and extinction, A_G, using a two-component residual model. The large green areas are off the galactic disc and have values close to zero, while the blue belt is the galactic disc with negative values. At the galactic centre, the values are positive. The positive values show where CO emission is stronger than A_G, while negative values show where A_G is strongest. The right plot shows the absolute value of the residuals on a logarithmic scale.

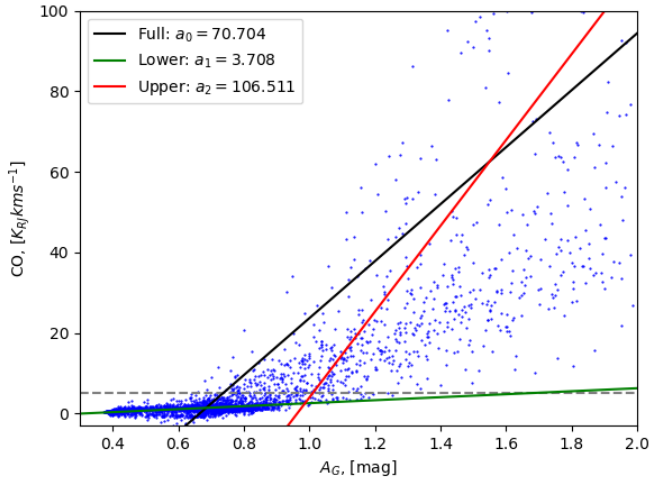

Figure 7.7: Correlation plot between A_G and CO, smoothed to 10°. The red line is the best linear fit for values above $y_{lim} = 5$ for CO (dashed grey lines), the green lines are for pixel values above y_{lim}, and the black line is for the full sets of data. The best-fit parameters for the slopes are for full, lower, upper lines: $a_0, a_1, a_2 = \{70.704, 3.708, 106.511\}$.

7.2 Polarisation comparison between optical and microwave data from RoboPol and Planck

In this section, we present the results from the analysis between visual and submillimeter polarisation in the following structure. First, we show the polarisation maps for the area in interest. Then, we show and list the correlation results both using RoboPol data together with PLA map, Npipe map and Sroll map, and the comparison with the data Planck Collab. XII (2018) used. Next, we show the line-of-sight extinction profile of the RoboPol observation area. At the end, we give the estimated spectral index of polarised thermal dust. Planck produce polarisation maps of both Q and U Stokes parameters, and thus we use both. In figure 7.8, we zooming in on the region of the sky RoboPol observe with resolution, $N_{side} = 256$ for both Q and U Stokes parameters. In these maps, we include all pixels to show the full structures.

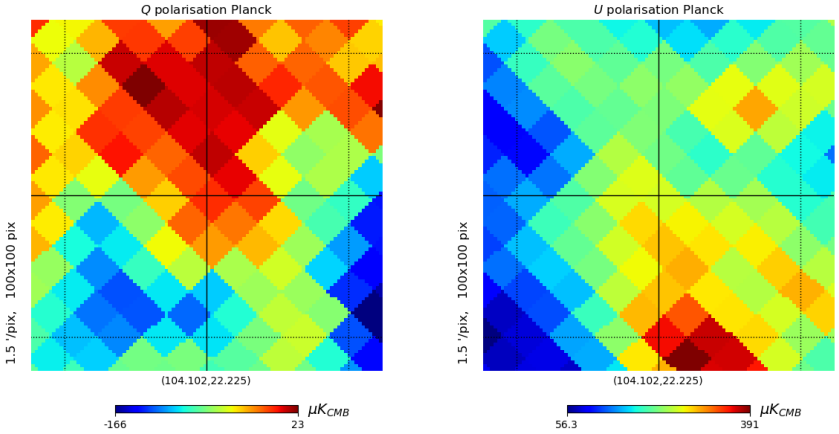

(a) Q (b) U

Figure 7.8: Polarisation from Planck in the observation area of RoboPol. The left plot shows the Q Stokes parameter and the right plot shows the U Stokes parameter. The maps have resolution $N_{side} = 256$. The larger diamond squares are the HEALPix pixels. The vertical labels describe the pixels of the cutout (Hunter, 2007) and the angular size of the cutout pixels, not the HEALPix pixels.

Focusing on the pixels given by the star coordinate, we compare polarisation intensity maps of RoboPols, q_v, u_v, and Plancks, Q_s, U_s, Stokes parameters. The maps shown in figure 7.9 are in gnomonic projection, where the grey areas are pixels without observed stars. In the upper row, we show the Planck polarisation maps in the pixels covering the RoboPol observation sky area. The lower row shows the fractional polarisation of RoboPol. The grey pixels are pixels without stellar data. The maps show both Stokes parameters are anti-correlated with the fractional Stokes parameters of the stellar data. Where the RoboPol maps are blue, the Planck maps are orange/red, and vice versa.

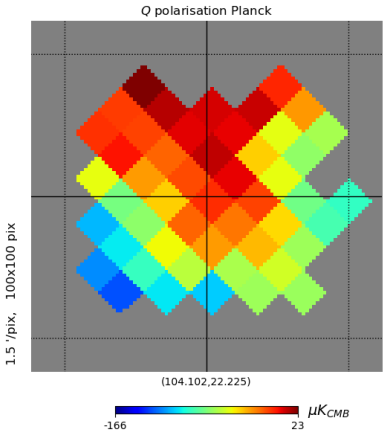

(a) Planck Q_s

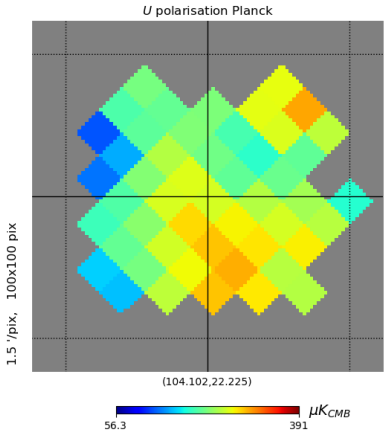

(b) Planck U_s

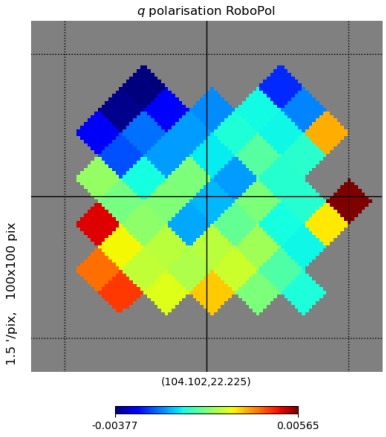

(c) RoboPol q_v

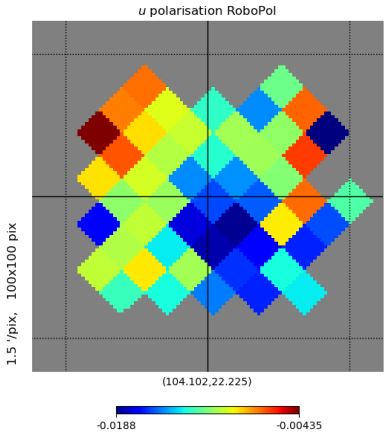

(d) RoboPol u_v

Figure 7.9: Polarisation maps covering the pixels RoboPol observe at $N_{side} = 256$. Upper left is the fractional polarisation q_v of RoboPol, upper right is u_v of RoboPol. Lower left is Planck Q polarisation and lower right is Planck U polarisation. The structures are anti-correlated to each other. The grey areas are pixels with no stellar data.

In the making of the correlations, we computed the difference in the mean polarisation angles between Planck and RoboPol to be at $\Delta\psi_{s/v} = -3.391^\circ \pm 0.517^\circ$ for $N_{side} = 256$. This is consistent with Martin, (2007) and the results of Planck Collab XII (2018), $\Delta\psi_{s/v} = -3.1^\circ$, and Skalidis and Pelgrims (2019), $\Delta\psi_{s/v} = -2^\circ$. We do not show their uncertainty because of the different smoothing resolution. When comparing the Stokes parameters from Planck with the fractional polarisation of RoboPol, we see an anti-correlation between Q_s and q_v, U_s and u_v and in the joint correlation. Figure 7.10 show this for $N_{sides} = 256$, where U_s, u_v is in blue and Q_s, u_v is in black, the colour scheme is the same for both the scatter points and line fits. The scatter points of U_s, u_v are negative on the x-axis since the fractional u_v parameter of RoboPol provides negative numbers in HEALPix convention, and the distribution of scatters points for Q is around zero on both axes. The red line shows the joint line fit of Q_s, U_s and q_v, u_v, and the orange line show the slope of the $-R_{P/p} = 5.42$ MJy/sr line from Planck Collab. XII (2018). Looking at only Q_s, q_v, the slope is $a_{Q,q} = -4.665 \pm 0.611$ MJy/sr with a Pearson correlation coefficient $R_{Qq} = -0.763$ and a best-fit from $\chi^2/dof = 0.599$. Considering U_s, u_v, the slope is $a_{U,u} = -2.485 \pm 1.123$ MJy/sr with a Pearson correlation coefficient $R_{Uu} = -0.715$. The estimated χ^2/dof for U_s, U_v is 0.811. The results for the joint distribution $Q_s U_s$ versus $q_v u_v$ give a Pearson correlation coefficient of $R = -0.963$ and reduced $\chi^2 = 1.995$. The best-fit line to the joint data points is $a_{QU,qu} = -4.535 \pm 0.444$ MJy/sr. We calculated the mean of the polarisation ratio to be $R_{P/p} = 4.47 \pm 0.82$. According to the result of Guillet et al. (2018), the value of $R_{P/p}$ indicate the dust grains have a prolate shape. Table 7.1 lists the results of NPIPE and Sroll, together with the main results. The results using NPIPE is biased since we use the covariance matrix of PLA since we do not have the covariance matrix of NPIPE.

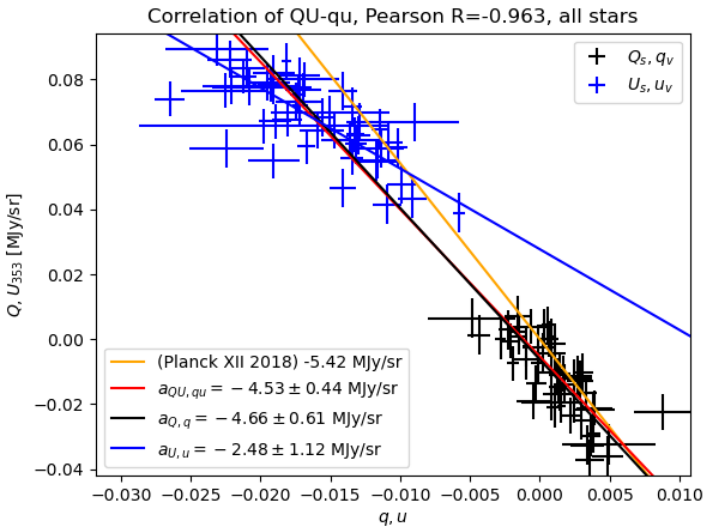

Figure 7.10: Correlation plot between the Stokes parameters of Planck, Q, U, and the fractional Stokes parameters of RoboPol, q_v, u_v. The blue line is the best-fit line using a χ^2 test to minimise $ax + b$ to the blue data points representing U_s, u_v polarisation. The black line and points represent the best-fit line and data for Q_s, q_v polarisation. The red line is the best-fit line to the joint data points of Q_s, U_s and q_v, u_v. The orange line is the result from Planck Collab. XII (2018).

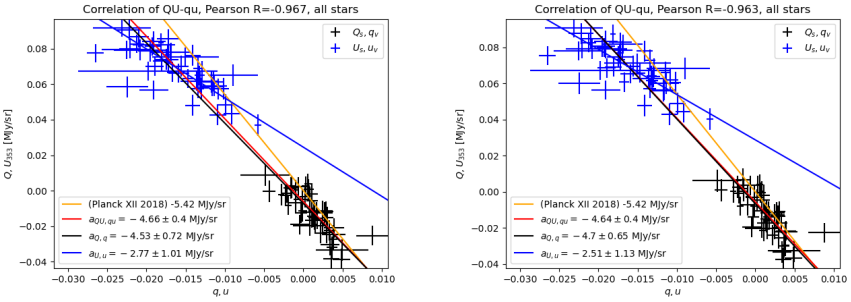

(a) NPIPE data (b) Sroll data

Figure 7.11: Correlation plot between the Stokes parameters, Q, U, of NPIPE (left) and Sroll (right) against fractional Stokes parameters, q_v, u_v, of RoboPol. The blue scatters and the best-fit line represents U, u_v-correlation, the black scatters and the best-fit line represents Q, q_v-correlation, the red line is the joint correlation best-fit line and the orange line is the -5.42MJy/sr result of Planck Collab. XII (2018).

Table 7.1: List of best-fit parameters, for $y = ax + b$, between Q_s, U_s and q_v, u_v from a reduced χ^2 test. The degrees of freedom for $N_{side} = 256$ is, $dof = 98$. In the fifth and sixth column, the Pearson correlation coefficient and the reduced χ^2. Line two and three show the results for Q_s vs. q_v and U_s vs. u_v individually. The lower part is our reproduction best-fit results of Planck Collab. XII (2018).

	a [MJysr^{-1}]	b [MJysr^{-1}]	Pearson	χ^2/dof
Joint	-4.535 ± 0.444	-0.005 ± 0.002	-0.963	1.995
Q_s vs. q_v	-4.665 ± 0.611	-0.006 ± 0.003	-0.763	0.599
U_s vs. u_v	-2.485 ± 1.123	-0.028 ± 0.013	-0.715	0.811
NPIPE 353 GHz data, PLA file for uncertainty				
Joint	-4.658 ± 0.401	-0.007 ± 0.003	-0.967	1.712
Q_s vs. q_v	-4.527 ± 0.722	-0.007 ± 0.003	-0.789	0.529
U_s vs. u_v	-2.77 ± 1.01	-0.025 ± 0.011	-0.761	0.69
Sroll 353 GHz data				
Joint	-4.643 ± 0.401	-0.006 ± 0.003	-0.963	2.033
Q_s vs. q_v	-4.698 ± 0.653	-0.007 ± 0.003	-0.765	0.597
U_s vs. u_v	-2.508 ± 1.127	-0.029 ± 0.013	-0.717	0.814
Planck Collab. XII (2018) reproduction				
Joint	-5.815 ± 0.192	6.493e$-4 \pm$ 3.06e-4	-0.828	0.808

In table 7.1, we summarise the results from the correlation analysis for the joint correlation, the individual correlations of the Stokes parameters and the biased reproduction of Planck Collab. XII (2018). Further, we list the results when using the 353 GHz map of NPIPE and Sroll in table 7.1. The result of the three different data processing maps show consistent results, where the results using NPIPE and Sroll have a little steeper best-fit slope than the official Planck data.

Next, we compare the results using RoboPol data with our reproduction of Planck Collab. XII (2018). In figure 7.12, the left column show correlation plot without (top fig. 7.12a) and with (bottom fig. 7.12c) error bars, and the right column show 2D histograms with the point density of RoboPol correlation (top fig. 7.12b) and Planck Collab. XII (2018) biased reproduction (bottom fig. 7.12d). All of the plots contain the same best-fit lines for the joint polarisation of RoboPol versus Planck data in solid black line, Planck Collab. XII (2018) reproduction in dashed black line and the result from Planck Collab. XII (2018) as the orange line. The slope of the Planck reproduction is $a_{pl} = -5.82 \pm 0.19$ MJy/sr, which steeper than the slope, -5.42 ± 0.05 MJy/sr, listed in the article (Planck Collab. XII, 2018). Further, the slope with the RoboPol data are more gradual than the two other lines, i.e. $a_{RoboPol} = -4.53 \pm 0.45$ MJy/sr. Since we have not debiased the data completely, there are some deviations, like a steeper slope of the best-fit line of our reproduction of Planck Collab. XII (2018). In figure 6.1, the fitted line is steeper than the resulting line $-R_{P/p} = -5.42 \pm 0.05$ MJy/sr, this may result from not debiasing the data.

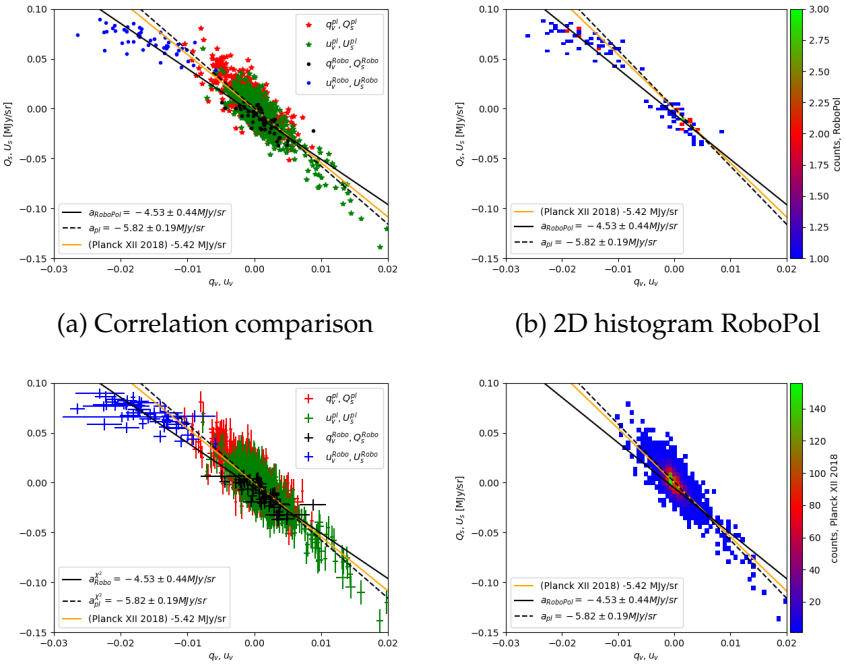

(a) Correlation comparison

(b) 2D histogram RoboPol

(c) Correlation with error bars

(d) 2D histogram Planck XII (2018)

Figure 7.12: Comparing the correlation plot between the Stokes parameters of Planck, Q_s, Us, and the fractional Stokes parameters of RoboPol, q_v, u_v with the data used in Planck Collab. XII (2018). The lines represent the best-fit lines: the orange line is the results from Planck Collab. XII (2018), the solid black line represents the best-fit line from χ^2-test for Q_s, U_s and q_v, u_v of RoboPol and Planck. Moreover, the dashed black line is the best-fit line for Q_s, U_s and q_v, u_v from Planck Collab. XII (2018). In the left column, the black Q_s, q_v and blue U_s, u_v scatter points represents the RoboPol comparison and red and green represents the data Planck Collab. XII (2018) used. The top figure show only scatter point and the bottom show with error bars. In the right column, the plots show 2D histograms of the point density with the RoboPol data to the top and Planck reproduction to the bottom. The axes cover the same ranges.

7.2.1 Robustness of correlation

We check rotational effects on the stellar polarisation data by adding a deviation to the polarisation angle. Figure 7.13 show the effect of rotating $\delta = \{15, 30, 45, 60, 75, 90\}$ degrees. The upper row is for rotation up to 45° and the lower row from 60° $\rightarrow$ 90°. At 45° rotation the values of $u_v = q_v$, and at 90° rotation $q_v(+90°) = -q_v$ and $u_v(+90°) = -u_v$, which show consistency with theory. Further, we check how a shift in the polarisation

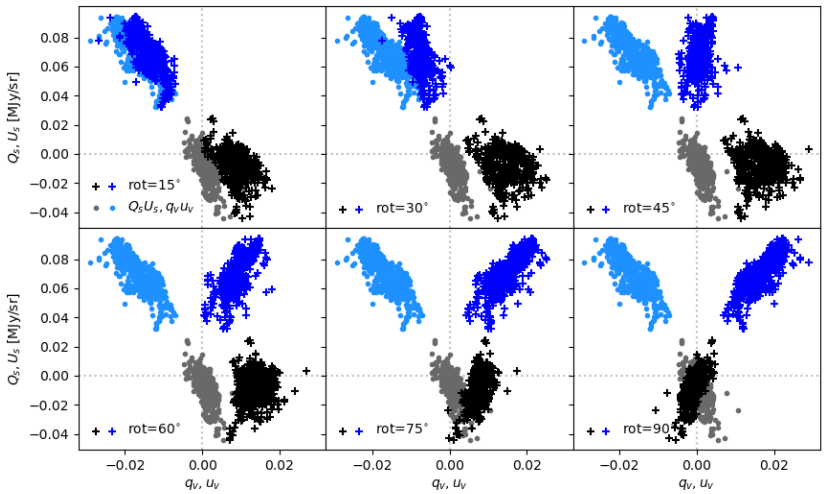

Figure 7.13: Correlation plots of rotating the polarisation angle for RoboPol data. We have rotated each plot an additional 15 degrees along the rows. The Blue and black + signs are the rotated data, and the light blue and grey scatters are the original data.

angle affects the correlation coefficients. Figure 7.14, show the behaviour of correlation as a function of rotation, the best-fit is shifted five degrees from zero, with only a small improvement of the correlation, 0.002 better. Figure 7.14 shows that the calibration of the polarisation detector of RoboPol is proper. Doing the same rotation test on Planck data give the same effect and results.

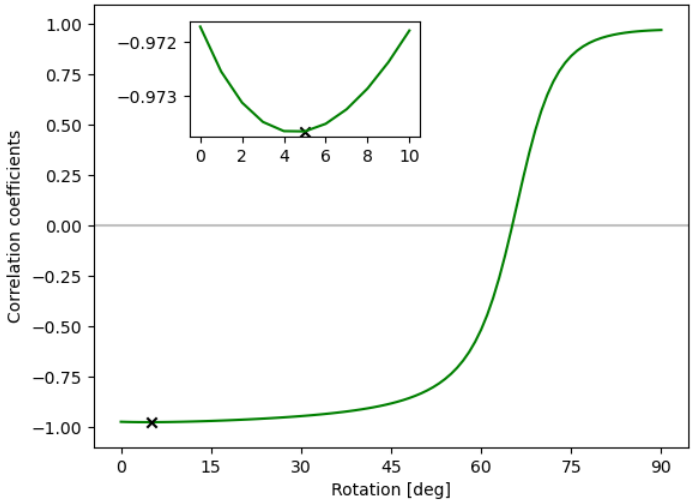

Figure 7.14: The Pearson correlation coefficients as a function of rotation angle. The inset shows the area around the best correlation coefficient at a five-degree rotation. The black cross show the best-fit.

7.2.2 Line of sight extinction in RoboPol data sky area.

Further, we make line-of-sight extinction profile for the area the tomography data of RoboPol comes from, $(l = 104.102^\circ, b = 22.225^\circ) \pm 0.75^\circ$. From Andrae et al. (2018) we know the extinction estimates of Gaia are not good, especially for low magnitude in extinction, and thus, we use the extinction data provided by Green19. In figure 7.15, we see the line-of-sight extinction profile in the observation area of the RoboPol. Our four sightlines show clear extinction patterns up to 1000 pc, with a steep increase from 300 to 400 pc. From the profiles, the amount of extinction is constant from 1000 pc and beyond. The green and black lines have a little lower amplitude than the blue and red line. The position of each line are for the blue line $(l, b) = (104.62^\circ, 21.79^\circ)$, for the red line $(l, b) = (103.86^\circ, 21.79^\circ)$, for the green line $(l, b) = (103.52^\circ, 22.34^\circ)$ and for the black line $(l, b) = (104.46^\circ, 22.59^\circ)$. The extinction profile shows an even distribution of the ISM structures in the area but with smaller structural differences. Using more sightlines may reveal more signatures in the extinction profiles, but also not give any additional information of the cloud structures.

7.2.3 The spectral index in MBB thermal dust model

Since there is a strong correlation between polarised starlight in visual and submillimeter polarisation, we continue to derive the properties of intergalactic dust. By using the polarisation data from RoboPol, we create a template to model submillimeter polarisation from visual polarisation. We use the template to estimate the spectral index in the modified blackbody

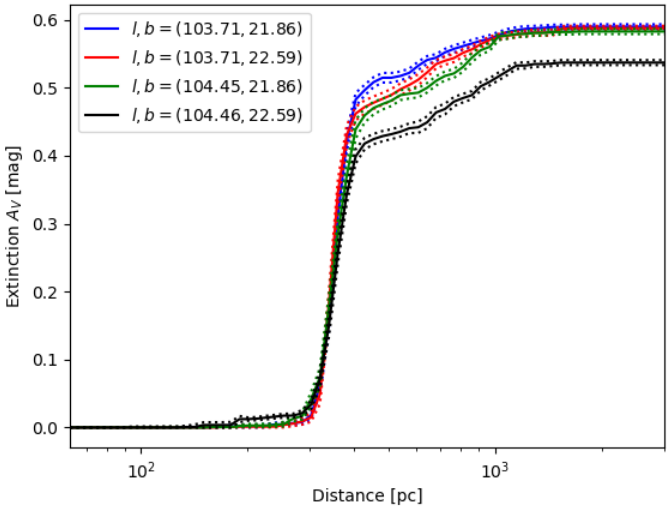

Figure 7.15: Line-of-sight extinction profile in the sky area the RoboPol observe. The solid lines are the four sightlines resulting from the extinction maps Green19 provide, and the dotted lines are the uncertainties. The x-axis is logarithmic to show better details at small distances.

model of thermal dust.

From the calculation of the spectral index for polarised thermal dust emission with a dust temperature of 19.6 K, we find $\beta_U^{217/353} = 1.563 \pm 0.007$ when considering the 217 to 353 GHz relation. For consistency, we calculate the spectral index for 143 to 353 GHz to $\beta_U^{143/353} = 1.666 \pm 0.011$. Table 7.2 show the values of β_U with the calculated uncertainties. Figure 7.16 show the distribution of sampled spectral indices for 217 to 353 GHz, the red line is the estimated β_U value and the dashed black lines are the 1σ lines from β_U. The calculated spectral index is not the mean of the distribution of samples, such that the mean of the histogram is not in the middle of the lines. We also compare the lower frequencies with the 353 GHz maps from Npipe and Sroll, where the second and third column of table 7.2 tabulates the representative spectral indices.

The Stokes Q-parameter give minimal contribution to the total polarisation. The scatters of both q_v and Q_s are around zero, which highly bias the spectral index computed from Q-polarisation. We neglect β_Q from the results since the estimated values are approximately zero and do not give any additional knowledge to the physics of the ISM. As we see in figure 7.17, the polarisation amplitude in Q at different frequencies are close to zero and give no significant spectral index.

We check the β for systematic effects by adding a shift in the polarisation angle. For shifts, $|\delta| \leq 5°$, see table 7.3, there is no significant change in β_U with all values within $1\sigma = \{0.01, 0.007\}$ from no rotation. Considering the systematic uncertainty of RoboPols measurement of polarisation angle of $\sim 1°$ (Ramaprakash et al. 2019), does not affect the

Table 7.2: List of the minimising factors α_i from equation (6.25) in the upper part and in the lower part the spectral index for a modified Blackbody spectrum, calculated from stellar polarisation of RoboPol and submillimeter polarisation intensity. The columns are for the Planck Legacy Archive (PLA) data files, and comparing with NPIPE and Sroll 353 GHz maps in the second and third column. The values of α and β are for Stokes U polarisation.

	PLA	Npipe	Sroll
$\alpha : 217 \rightarrow 353$	0.129 ± 0.002	0.126 ± 0.002	0.126 ± 0.002
$\alpha : 143 \rightarrow 353$	0.027 ± 0.001	0.036 ± 0.001	0.037 ± 0.001
$\beta : 217 \rightarrow 353$	1.563 ± 0.007	1.617 ± 0.007	1.608 ± 0.007
$\beta : 143 \rightarrow 353$	1.666 ± 0.011	1.697 ± 0.011	1.69 ± 0.01

Table 7.3: The effect of rotation on β. There is no significant change in the spectral index for rotation of $\delta \leq \pm 5^\circ$. We include the shift at $\delta = \pm 25^\circ$ since this is around $1\sigma = \{0.01, 0.007\}$ from no rotation.

δ [deg]	$\beta_U^{143/353}$	$\beta_U^{217/353}$
-25	1.673	1.557
-5	1.667	1.563
-4	1.666	1.563
-3	1.666	1.563
-2	1.666	1.563
-1	1.666	1.563
0	1.666	1.563
1	1.666	1.563
2	1.665	1.564
3	1.665	1.564
4	1.665	1.564
5	1.665	1.564
25	1.658	1.571

estimation on β. The numbers are also close to our results. Since we obtain no spectral index for the Q Stokes parameter, we use β_U as the spectral index for polarised dust intensity.

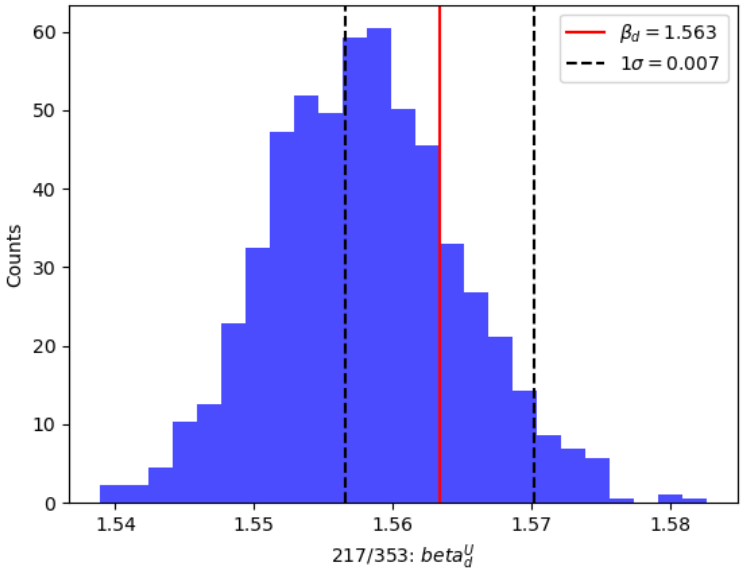

Figure 7.16: The distribution of sampled β_U values for 217 to 353 GHz, the red line is the estimated value of β_U and the dashed lines marks the 1σ lines

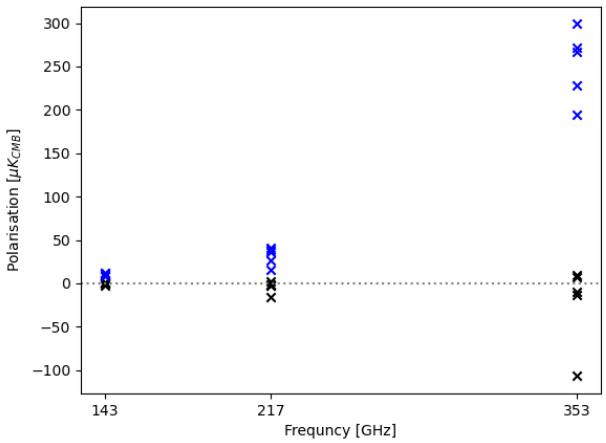

Figure 7.17: Plot showing magnitude difference between Q and U as a function of frequency. Stokes Q is the black scatters, and the blue scatters are for Stokes U. The scatters are five randomly chosen pixels, and the dotted grey line marks zero polarisation.

Chapter 8

Component separation combining optical and microwave astronomy

The plan now is to combine the optical observations with the data from Planck more thoroughly using MCMC sampling methods, like the Metropolis-Hastings algorithm and Gibbs-sampling, exploring both the connection to extinction and starlight polarisation. Because of the complexity of the ISM, MCMC sampling provides a useful way of exploring the probability distributions of the parameter-space describing the ISM. We will focus on properties related to polarisation using models on thermal dust and synchrotron radiation together with the CMB. The parameters describing thermal dust are transferable to the extinction of light as well. This chapter contains a description of how we implement the sampling routines using the Metropolis-Hastings algorithm and Gibbs sampling. Then describe details regarding modelling on constructed mock data and data from Planck. For these two cases, we express the likelihood and priors we use.

We have implemented a preliminary sampling routine as described in the following sections. Unfortunately, the limited amount of time prevented us from obtaining results and therefore left to future work.

By using Bayesian statistics we can probe the posterior distribution, $P(\theta|\mathbf{d})$, for each parameter using Bayes' theorem eq. (4.1). Where θ are the free parameters we need to fit, and $\mathbf{d}$ is the data from observations. We assume $\mathbf{d}$ is the sum of the signal, $\mathbf{s}(\theta)$, we want and the noise, $\mathbf{n}$, in the signal,

$$\mathbf{d} = \mathbf{s}(\theta) + \mathbf{n}, \tag{8.1}$$

where we assume the noise is Gaussian distributed as in (Planck Collab. X, 2016). The likelihood is then, $\mathcal{L}(\theta) = P(\mathbf{d}|\theta)$, and the prior, $P(\theta)$.

We solve component separation of the polarised foregrounds, thermal dust and synchrotron radiation together with the CMB signal, in the data provided by Planck using sampling and model the intensity of each foreground. We want to map the probability distribution of the parameters

in the model using Metropolis-Hastings and Gibbs-sampling. The model for the signal we use is,

$$\mathbf{s}(\theta, \nu) = I_{CMB} + I_{dust} + I_{sync} + n, \tag{8.2}$$

$$= \mathbf{A}_{CMB} \frac{\mathbf{x}^2 e^{\mathbf{x}}}{(e^{\mathbf{x}} - 1)^2} \frac{(e^{\mathbf{x}_0} - 1)^2}{\mathbf{x}_0^2 e^{\mathbf{x}_0}} \tag{8.3}$$

$$+ bA_{extinction} \left(\frac{\nu}{\nu_0}\right)^{\beta_d + 1} \frac{e^{\mathbf{x}_0} - 1}{e^{\mathbf{x}} - 1}$$

$$+ \mathbf{A}_s \left(\frac{\nu_0}{\nu}\right)^{\beta_s} + n, \tag{8.4}$$

where $x = h\nu/k_B T$, x_0 is at the reference frequency, ν_0, of the component at 100, 353 and 30 GHz respectively, and n is the Gaussian noise given as $\mathcal{N}(0, \sigma = 10)$. The bold font represents pixel dependence on the parameters. The model gives a jointly distributed parameter set $\theta = \{b, T_d(p), \beta_d(p), A_{CMB}(p), A_s(p), \beta_s(p)\}$, where the five last parameters depend on position in the sky, where p stands for pixel, and we assume b is independent on sky position. For the thermal dust parameters, b is a scaling factor between A_{dust} and $A_{extinction}$, such that $A_{dust} = bA_{extinction}$, where $A_{extinction}$ is a spatial template of extinction data. We use a uniform extinction template as a simple approximation. T_d is the dust temperature and β_d is the thermal dust spectral index. For CMB, A_{CMB} is the amplitude in the CMB model. And for synchrotron, A_s is the amplitude and β_s is the spectral index for synchrotron. We define $\mathbf{y}_p = \{T_d(p), \beta_d(p), A_{CMB}(p), A_s(p), \beta_s(p)\}$ for short notation. The initial motivation to use Gibbs sampling is because we can draw samples from the marginal distribution of the parameters.

8.1 The sampling algorithm

In this section, we outline the sampling routine created to solve the problems requiring MCMC simulations, involving the Metropolis-Hastings algorithm and Gibbs sampling. The model involves a set of six free parameters in, $\theta = \{b, \mathbf{y}_p\}$, where $\mathbf{y}_p$ contains the five free parameters fitted to each pixel in turn, while b fitted to every pixel simultaneously. To estimate the value of b, we first sample the values of the dust temperature and the spectral index. The Gibbs chain explaining the sampling steps, drawing b given $\mathbf{y}_p$ for all pixels and drawing for each pixel $\mathbf{y}_p$ given b, goes as for Gibb-step i,

$$\mathbf{y}_{i,p} \leftarrow P(\mathbf{y}_{i,p}|b_i) \tag{8.5}$$

$$b_i \leftarrow P(b_i|\mathbf{y}_{i,p}), \tag{8.6}$$

where $\leftarrow$ means drawing a sample from the distribution on the right-hand side. The first step is to initialise the sampling by drawing some random values of parameters we want to fit. We use the `multivariate_normal` function provided by the random class in Numpy (Oliphant, 2006), which

take an initial guess of the parameter values and a covariance matrix as input and draw values from the Gaussian distribution of the variables. We write the probability distribution as

$$P(b_i|\mathbf{y}_{i,p}) = \frac{1}{|\sqrt{2\pi\sigma_b^2}|}\exp\left\{-\frac{b_i^2}{2\sigma_b^2}\right\} \tag{8.7}$$

$$P(\mathbf{y}_{i,p}|b_i) = \frac{1}{|\sqrt{2\pi C_y}|}\exp\left\{-\frac{1}{2}\mathbf{y}_{i,p}C_y^{-1}\mathbf{y}_{i,p}^T\right\}, \tag{8.8}$$

where C_y, σ_b is the covariance matrix of $\mathbf{y}_{i,p}$ and the standard deviation of b_i respectively. Then we make an initial model based on the drawn parameters and calculate the initial log-likelihood and log-prior.

The structure of the algorithm is a loop covering the Gibbs samples and using the Metropolis-Hastings algorithm over the jointly distributed parameters in $\mathbf{y}_{i,p}$ and b_i. The algorithm goes as:

1. For Gibbs step i, for pixel p initialise the parameters in $\mathbf{y}_{i,p}$, and check that the all is positive. The log-prior is given as: $\sum_i P(\theta_i) = \sum_i -0.5((\theta_i^* - \theta_{0,i})/\sigma_i)^2$ with the θ^* as the proposed parameters and θ_0 as the "perfect model" parameters, σ is the uncertainties of the parameters.

2. Do the Metropolis-Hastings algorithm to sample $\mathbf{y}_{i,p}$, see 4.2.1, holding b_i constant. Which returns the last accepted parameters.

3. Initialise b_i and check the initial value to be positive.

4. Sample b_i using the Metropolis-Hastings Algorithm, see 4.2.1, while holding $\mathbf{y}_{i,p}$ constant.

5. Update the initial guess on the parameter estimations of $\mathbf{y}_{i,p}$, using $\theta_{0,new} = \theta_0 + \mathcal{N}(0, \sigma)$. Then go to step 1.

We use 100 Gibbs steps and 3000 iterations in the Metropolis-Hastings algorithm. The Planck data come with a resolution of $N_{side} = 2048$ giving $\sim$ 50 million pixels. To sample over that many pixels give a huge computational cost, so we downgrade the resolution to $N_{side} = 1$ giving twelve pixels. Further, the optimisation of the algorithm for fast computation is poor, e.g. for $N_{side} = 16$, the estimated computation time on is approximately 40 hours.

We update the covariance matrix from the accepted samples in the Metropolis-Hastings algorithm with a burn-in period of $N/2$ for $N = \{300, 600, 900\}$. The covariance matrix continues to the next Gibbs-step. We update the covariance matrix further due to the acceptance ratio for every 50 iterations in the Metropolis-Hastings algorithm. We do this by multiplying or dividing the covariance matrix by a scale factor equal to 2. The acceptance ratio is the number of accepted draws per iterations so far. We do not want the acceptance ratio too high nor too low, but between $[0.2, 0.5]$, divide if acceptance is too low, and multiply if acceptance is too high.

8.2 Sampling mock data intensity

To check the sampling routine, we create mock data point by using a constructed model for the microwave signal at different frequencies, containing intensity from CMB, thermal dust and synchrotron radiation and noise. We check if the sampler can sample parameters describing the data points at the same frequency bands as Planck (Planck Collab. I, 2011). The values of the likelihood and prior can be large or small, such that working with the logarithm of the likelihood (log-likelihood $p(d|m) \rightarrow \ln(p(d|m))$ and the prior (log-prior $p(m) \rightarrow \ln p(m)$) is more convenient. The log-likelihood of the model is given as,

$$\ln \mathcal{L}(\theta) = -\frac{1}{2} \sum_i \left[\frac{(\mathbf{d}_i - \mathbf{s}_i(\theta))^2}{\sigma^2} \right], \tag{8.9}$$

with σ as the standard deviation of the noise. We express the log-prior as,

$$\ln p(\theta) = \begin{cases} \sum_i^{N_{params}} \left[-\frac{(\theta_i - \mu_i)^2}{2\sigma_i^2} \right], & \forall \{\theta_i > 0\} \\ -\infty & \text{else,} \end{cases} \tag{8.10}$$

where N_{params} is the number of parameters drawn, μ_i is the "perfect model" parameters, θ_i is the drawn parameters, and σ_i is the uncertainty of the drawn parameters. Note, we have flipped the power-law in the synchrotron model, see eq. (2.4) and (Planck Collab. X, 2016). For the condition giving $\ln P(m) = -\infty$ we use numerically -50. Table 8.1 lists the values of the initial guess, "perfect model" and uncertainties for the proposed parameters. We use values inspired by Planck Collab. X (2016) with the initial guess values around the same order as the "perfect model" values.

Table 8.1: Table with the initial guess values of the parameters, the "perfect model" parameters and the guessed uncertainties of the parameters. In the relation $A_{dust} = bA_{extinction}$, $A_{extinction} = 10$.

	b	T_d	β_d	A_{CMB}	A_s	β_s
Initial guess	1.0	10.0	1.0	10.0	10.0	1.0
Perfect model	3.0	25.0	1.5	12.0	50.0	3.0
σ	0.2	5.0	0.3	4.0	5.0	0.2

8.3 Sampling Planck data

The next step is to include observation data from Planck instead of the constructed mock data used in the previous section, and sample over the free parameters describing the model (8.2). We use data from all the passbands of Planck. The 100 GHz band contain one pixel, at $N_{side} = 1$, with a value completely different from the other values ($\mathcal{O}(30)$ different).

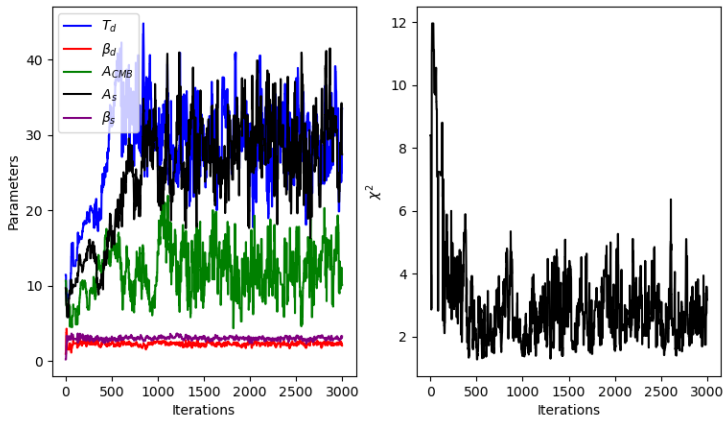

Figure 8.1: Example from the sampling inside the Metropolis-Hastings part of the Gibbs sampler. The left plot shows the samples of the pixel dependent parameters. The right plot shows the χ^2/n for the model given by the sampled parameters. The sampler converges after at least 1000 iterations.

We handle this by ignoring the specific pixel in the sampling. The units of the data are K_{CMB} and MJy/sr. It is more convenient to work with brightness temperature, such that we convert the units to, μK_{RJ}. In appendix A.2, we discuss the conversion of the units. We use 30 GHz and 353 GHz as a reference frequency for synchrotron radiation and thermal dust emission, corresponding to the reference bands used in Planck Collab. XII, (2014) and the polarisation reference bands in Planck Collab. X, (2016). For the CMB component, we use 100 GHz as the reference frequency. To find the best parameters, we calculate the maximum log-likelihood of the samples, for each pixel and the mean over pixels. The estimation of the uncertainties uses standard deviation for each pixel and error in the mean for the mean.

We check how the sampler work by plotting a sampling chain of the parameters in a pixel and a reduced $\chi^2 = -2 \ln \mathcal{L}/n$. Figure 8.1, shows in the left plot how the sampled parameters converge in a given pixel. The right figure shows the reduced χ^2, where n is the number of parameters for the pixel.

Chapter 9

Discussion, conclusion and future aspects

In this chapter, we discuss the results from each part individually presented in chapter 7 and compare with previous studies. Then we summarise our results in the conclusion section. At the end, we discuss the future of the field and talk about coming research.

9.1 Gaia extinction estimation

When discussing the extinction estimates, we start with the maps and compare them to similar studies. Then we discuss the line-of-sight extinction profiles. Lastly, we discuss the comparison to foreground components. Comparing the cumulative differential reddening of Green19 with the results of cumulative differential extinction at different distances, see figure 7.1, there are many similarities in the total integrated maps. Green19 map shows the same structures as mine, with a broad high amplitude area toward the galactic centre and a narrow belt up to 90° left. Further, the large fan from $\sim$ 90° to $\sim$ 210° are visible. The same regions is noticeable in the polarisation map of thermal dust from Planck Collab. X (2016), see figure 2.9.

When looking at different distances in figure 7.2, the 0 to 300 pc and 300 to 600 pc maps and Green19, 0 to 500 pc map, the same structures are apparent. The main patterns are visible with a substantial extinction/reddening section toward the centre of the galaxy, and a large cloud area from $\sim$ 90° to $\sim$ 210° left, i.e. the fan region. The 300 pc map shows these regions, such that the cloud begins at distances closer than 300 pc. Moving up to 1000 pc, we see many similarities when looking at our maps and Green19 map, with an extensive cloud region from 30° to 240° left. Between 1000 and 2000 pc, Green19 have only one map, while we have four maps covering the distance space in figure 7.2. To compare cumulative extinction between 1000 and 2000 pc, we make one additional map covering the distance-space. We see prominent parts along the galactic disc in all maps, with more substantial regions around the galactic centre

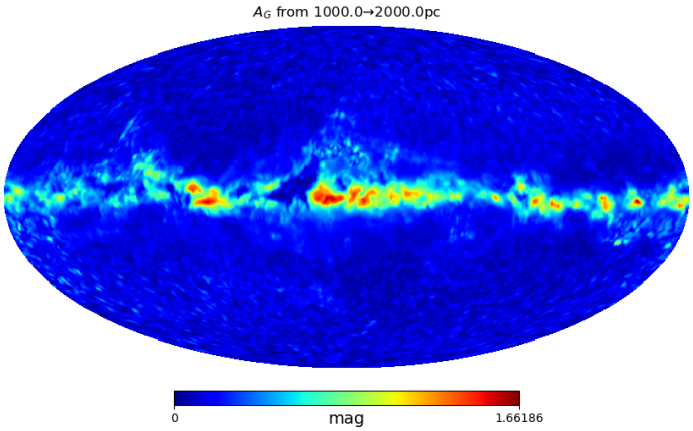

Figure 9.1: Cumulative extinction map from 1000 to 2000 pc.

and 90° left. Around 30° left for the centre there is an empty area, the same area is fainter in the map of Green19. In the right part of the map, some clouds are visible. For distances over 2000 pc, the maps are more different, but the galactic disc is visible in all maps. Both Green19 and us use the cumulative line-of-sight derivative of the median reddening or mean extinction in each pixel, respectively, $A(r_2)' = A(r_2) - A(r_1)$, under the construction of $A' \geq 0$. In the subtraction the extinction of closer maps, some pixels will get negative extinction estimates because of the large global uncertainty in the Gaia extinction estimates, we correct for this by setting the negative values to be zero. The large steps in the distance intervals reduce the noise of A_G from the mean estimation. If using smaller distance intervals, the maps will be noisier.

Lallement et al. (2019) provides three-dimensional differential extinction maps, covering a volume of $3000 \times 3000 \times 600$ pc around the Sun. Their maps are slices through the galactic plane in both z direction, i.e. perpendicular to the galactic plane, and in ϕ direction, the latter are slices at every tenth degree around the plane. Their maps illustrate the local bubble around the Sun with little dust to redden the starlight up to distances of 100 to 300 pc (Cox and Anderson, 1982). Further, we notice many of the same structures appear at the same distances, as shown in the extinction maps. Like for example, much extinction toward the galactic centre at $r < 500$ parsec and the structures from $\sim 90°$ to $\sim 180°$. But also empty regions from $l \sim 180°$ to $l \sim 300°$ for distances $r < 600$ pc. Toward the galactic centre, the maps of Lallement et al. (2019) show little extinction from 300 pc to 900 pc, supported by Green19 500 pc to 1000 pc map, my results showing weak extinction patterns in the same regions. There is a strong extinction pattern at $l \sim 270°$ from 600 pc to 1000 pc, which appears in both maps, figures 7.2c and 7.2d, and in the maps of Lallement et al. (2019), unfortunate Green19 does not cover this part of the sky.

The primary differences between Green19 and Lallement et al. (2019) maps and ours are the noise at large latitudes beyond the galactic disc, $|b| > 20°$. Further, the structures of the Local bubble is less apparent

in the 300 pc and 600 pc map, 7.2a and 7.2b, than in Lallement et al. (2019) and Green19. The 300 pc map contain noise covering eventual faint patterns. The data Green19 use have more sources and better photometry than Gaia DR2 regarding extinction, and their maps have higher resolution than mine, which increase the visibility of details in the neighbouring ISM structures become.

9.1.1 line-of-sight extinction estimates

In figure 7.3, the five first plots show the line-of-sight extinction of Gaia and from Green19 for five longitudes. The last plot in figure 7.3 show the sightlines of the previous plots on the total extinction map, $A_G(r \leq 3000\text{pc})$. These results show similarities in the shape of the curves and scatter points. In the conversion from the reddening of Green19 to extinction, we have used the *r*-band value in the extinction vector, see table 3.2, giving the amplitude closest to Gaia, even though the frequencies might not be the same.

In particular, one might notice the green line, $l = 110^\circ$, in figure 7.3d have high extinction and rise a lot within the first 500 pc because the location of the line is in the fan region. The profile will be in the bright area to the left in the maps in figure 7.2. The same area shows much reddening and differential extinction in both Green19 and Lallement et al. (2019) maps. It is interesting that the line-of-sight extinction curves of Gaia and Green19 are in agreement for the galactic plane sightlines, the red lines and scatters in figure 7.3. There is some deviation on amplitude, but they have still the same shape.

There is a clear connection between the amplitude of the line-of-sight curves in 7.3 and the extinction maps in 7.2. The line-of-sight curves in figures 7.3b, 7.3c and 7.3d show the wide fan from 90° to 200°, with the red lines and the green line in the 180° figure. The steep rise in amplitude in the four first plots of 7.3 (red lines) show there is much extinction at these areas, as shown in the close distance maps in 7.2. Further, the maps 7.2d and 7.2e confirms the rise in extinction between 1000 pc and 1500 pc in figure 7.3e.

The size of the sightlines, $5^\circ \times 5^\circ$, reduce the noise from the averaging over data, but the large line-of-sights may smooth out different structures. The lines from Gaia DR2 and Green19 are the averaging of the extinction estimates in the distance intervals of each sightline, because of the prominent uncertainties and possible negative numbers in the differential extinction. We could have differentiated the extinction estimates by using other differentiation methods like the two-point method or higher-order methods.

9.1.2 Comparing extinction with dust and CO

A trained eye notice similarities in the distribution of A_G in figure 7.1 and the dust intensity, and with CO line emission maps of Planck. Figure 7.4, shows the difference between dust and extinction. Here we see most areas are around zero, with large negative parts, fig. 7.4a, these parts

are normally at high latitudes. In particular, the galactic disc is less trivial, see figure 7.4a, where the difference varies a lot between dust domination at the galactic centre and extinction domination in the rest of the plane. The logarithmic map of the absolute residuals between dust and extinction in figure 7.4b highlight smaller variations outside the galactic plane. While at the galactic centre, the amount of dust dominates the extinction. Comparing figure 7.4 with figure 7.1, the strong extinction regions are the same as the minimum area in the residual map. However, the dust intensity in the galactic centre is stronger than the intensity of extinction.

When comparing CO and extinction, much of the same pattern appears, as in the dust comparison, see figure 7.6a and 7.6b. Where the galactic disc is either dominated by the extinction or by CO line emission, and the rest of the sky is less than zero and varies little. The logarithm of the absolute value of the residual maps show differences at high latitudes, fig. 7.6b. One might notice the area just above the galactic centre where the extinction is much stronger than the dust/CO intensity, giving significant differences along the galactic disc concerning the extinction. When looking at both figures 7.6 and fig. 7.1, the strong extinction areas are the minimum areas in fig. 7.6. At the galactic centre, the extinction is less suppressed than for dust.

Figure 5.5 show that the line fit for component values above $y_{lim} = \{7.5\text{MJy/sr}, 5\text{K}_{\text{RJ}}\text{km/s}\}$ (left and right respectively) are covering the galactic disc. Looking at figure 7.5 and 7.7, the data points contributing to the red line of the high values of dust and CO values are more spread out. The spread-out cause the large residual difference in the figures of 7.4 and 7.6. For the sky areas beyond the galactic disc, the scatters are less spread out and have smaller amplitude such that the residual differences are smaller when evaluating equation (5.12).

Since we have zoomed in on the primary group of data points in the figures 7.5 and 7.7, the black line of all data points lay above the primary group of points. There are significant differences in the CO map, the primary group of scatters got lower amplitude, and the high values are higher than in the dust map. As mentioned earlier, the extinction estimates of Gaia DR2 are noisy, giving considerable uncertainties in these estimated residuals. If using more precise extinction measurements, the comparison with dust intensity and CO line emission will be more precise.

Since we use two lines to describe the data, a second-order polynomial might be a better choice of model, $f(x) = ax^2 + bx + c$. As seen in the figures 7.5 and 7.7, the component intensity rise for higher extinction values. However, since there are clear differences between the values in and outside the galactic plane, a two-component model may be the best way to describe the data. A χ^2-test for both models will test if a two-component model or a second-degree polynomial gives the best description of the data. Further, we have not included uncertainties in the residual calculations, which may contribute to a better line fitting, e.g. using a similar χ^2 test as described in section 6.2.1. Further, since there is a distance limit in the extinction model at 3000 pc, we would expect

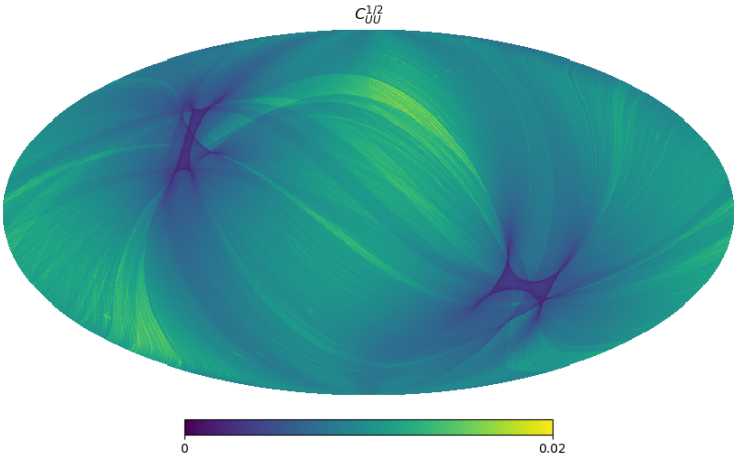

Figure 9.2: The uncertainty of Planck, U polarisation, tracing also the scanning strategy of Planck. The dark areas have smaller uncertainty since scanned several times. Units are in K^2_{CMB}.

differences compared to foreground maps which covering all distances, and thus larger residuals. Extrapolating the extinction model to greater distances may give smaller differences and tighter fit to thermal dust and CO.

9.2 On polarisation of stellar and thermal emission

The polarisation results show a strong correlation between starlight polarisation in visual and polarisation in submillimeter from thermal dust emission, with a Pearson correlation coefficient equal -0.963 for $N_{side} = 256$. The smoothing and low resolution of both the data from RoboPol and Planck increase the correlation coefficient because of the noise reduction.

Considering our method, which average over the stars in the pixel and distance. For example, a pixel containing two stars at different distances, $r = [0.5, 2]$ kpc, and $q = [0.01, 0.3]$, giving the mean polarisation at the mean distance between the stars. The distance averaging limits the 3D space of the polarisation maps. If the goal is to work with 3D structures of polarisation, a different approach is needed. E.g. to handle each star independently and assign the pixel-number to the star when comparing with submillimeter polarisation from the background (Skalidis and Pelgrims, 2019). This method is less dependent on the N_{side}, keeping the data points of the stars instead of proportional to the resolution, and also describe the polarisation in three dimensions.

From table 7.1 and the figures 7.10 and 7.11, the correlation slopes are a little steeper for the supplementary maps by around 0.1 MJy/sr. The difference is because of the different methods in producing the submillimeter polarisation maps. The spectral index estimation shows the same effect, where both NPIPE and Sroll data give a slightly higher β.

When comparing our findings to the results of Planck Collab. XII

(2018), my estimated slopes are more gradual, -4.531 ± 0.445MJy/sr, at $N_{side} = 256$, to -5.42 ± 0.05MJy/sr. We expected less steep slopes since we have not corrected for depolarisation of the beam, only corrected for extinction. However, when looking at our biased reproduction and figure 23 in their paper, the distribution of data points seems equal. The correction for extinction factor is larger than one and multiplied to the fractional polarisation giving a spread-out in the x-direction. Including the correction of extinction makes the slope less steep. The effect of the beam depolarisation will cause a spread out y-direction since Planck's beam-width is larger than the point source width of the star data, this factor is also larger than one and increase the steepness of the slope. When comparing stellar polarisation to polarisation of light from the background, there is a bias laying in the distance difference between the star and the background. We can correct for this bias by multiplying the starlight polarisation with the ratio between the total reddening and the reddening of the star, under the naïve assumption of a uniform distribution of reddening. To illustrate this, consider a star in the first bin in figure 5.2, and the CMB signal coming from the next bin, then the two sources experience different reddening. Figure 1 in Planck Collab. Int XXI (2015) nicely visualise the effect of different distances to sources, since the background-light travels through all the ISM, and the starlight only travels through parts of the ISM depending on the distance to the star.

Figure 9.2 shows the covariance elements of U polarisation from Planck. The areas with bright colours have large variance, and the dark areas have small variance. The two large dark patches are the celestial north and south pole. Figure 7.12c show the uncertainty given by the Planck data varies between the two data sets. When considering that the RoboPol data use an area of the sky where Planck have low variance, and the star data Planck Collab. XII (2018) used are from a large part of the sky with some regions having large variance and other parts low. The variance in uncertainties will give larger error bars for the Planck Collab. XII (2018) results than for the RoboPol results. Further, we have only corrected the uncertainties of the RoboPol data from biasing effects, such that is a bias in the error bars in figure 7.12c.

The line-of-sight extinction profile of the RoboPol sky area shows a significant increase from 300 to 400 pc. At distances over 400 pc, different amplitudes are showing an uneven distribution of the clouds. The sharp increase is around the same distance as the Low-Velocity Cloud examined by Panopoulou et al. (2019). Comparing with figure 7.15 there is also a distinct step in the extinction profile for the first cloud, but with smooth edges. The continuous increase from 500 to 1000 pc could mean there are smaller structures along the sightline paths. Panopoulou et al. (2019) also investigate a cloud further away in the same region, from 1200 pc to 2000 pc, extinction patterns from this cloud is not visible. Zucker et al. (2019) model the line-of-sight extinction profile as a step-function, by assuming sharp edges of the ISM clouds, when comparing the line-of-sight extinction profile in the RoboPol area this makes sense. The averaging over sky-patches smooths the extinction profiles. We think a smoothing of the

step function instead is a better description of the extinction profile. There are mathematically function describing this behaviour, like the Sigmoid function or smoothstep function. However, our thoughts need further investigation.

From table 7.2, the spectral index for 143 to 353 GHz is around 0.1 larger than the spectral index for 217 to 353 GHz. Comparing our results with the results of Planck Collab. XXII (2014) and Planck Collab. XI (2018) the spectral index is between the two Planck results, considering the $217 \rightarrow 353$ relation, the uncertainties are in the same order of magnitude, 0.01 to 0.02. The difference between the 2014 and 2018 results is because of correction of data systematics between Planck Collaborations second press release and third press release. The uncertainty difference may come from the difference in how much of the sky investigated between the different studies. Planck Collab. XI (2018) look at extensive parts of the sky with a mask covering where CO line emission is strong and calculate β_d from analysis of E- and B-modes, while we analyse a small part of the sky.

The effect of debiasing the stellar polarisation data with correction for extinction, eq. (6.19), is small for stars at distances over a certain distance. In figure 7.15, the effect of applying this ratio will for close stars be significant, but for stars far away the effect will be small, $E(B-V)^{\infty}/E(B-V)^{\star} \approx 1$. From figure 7.15, the limit where the ratio goes to 1 is over 1000 parsec, which is consistent with the extinction profiles in figure 7.3 for the sightlines above and below the galactic plane. For sightlines in the galactic plane, the emission-to-extinction ratio is crucial to include for all the stars. Since we only debias the starlight polarisation data with the extinction ratio, an underestimation of $R_{P/p}$ and the slopes of the Q_s, q_v and U_s, u_v may occur. Correcting for beam depolarisation in the submillimeter data will increase the polarisation values and thus make the slopes steeper. The beam depolarisation bias may affect the template and the calculation of the spectral index to an uncertain degree.

9.3 Conclusion

We present the results regarding extinction estimation in three dimensions using data taken from Gaia DR2 with comparison to relevant work, together with a sampling routine to estimate intensity. And the correlation between starlight polarisation and thermal dust polarisation.

Our 3D extinction estimates based on Gaia DR2 reflects the dust distribution up to 3000 pc from the sun. We created 3D maps of extinction from integrating differential extinction, as shown in figure 7.2. Even though the extinction estimates of Gaia DR2 contain much noise, they show the same structures as presented in Green19 and Lallement et al. (2019). Further, we show on large latitudes correspondence of extinction to both thermal dust and CO line emission in figure 7.4 and figure 7.6. The best fit parameters for dust is $a_2 = 5.903, a_3 = 49.63$ MJy/sr/mag, and for CO line emission $a_2 = 3.708, a_3 = 106.51 \mathrm{K_{RJ}km/s/mag}$, where a_2 is the best fit value for low intensity and a_3 is the best fit values for high intensity. The

more complex intensity pattern in the galactic plane demand better models. Comparing the line-of-sight extinction estimates from Green19 with the estimates of A_G, we see they mostly follow the same pattern. There are two primary reasons for deviations: first, the extinction estimate of Gaia DR2 A_G is not the same as the extinction estimate from Green19. The estimated $A_V = R(V)E(B-V)$ is giving the extinction at a different frequency than A_G. Second, the extinction estimates of Gaia DR2 contain much noise, $\sqrt{\langle A_G^2 \rangle} = 0.46$ (Arenou et al., 2018) for each estimate, contaminating further the line-of-sight estimate. Using the extinction estimates of Gaia DR2 correctly is important to achieve decent results.

The starlight polarisation angle is almost perpendicular to the sub-millimeter polarisation angle, $\Delta\psi_{s/v} = -3.391^\circ \pm 0.517^\circ$ at $N_{side} = 256$. The Pearson correlation coefficient between the star light polarisation of RoboPol and thermal dust polarisation of Planck at $N_{side} = 256$ are $R = -0.963$, and a $\chi^2 = 1.995$. The best-fit line of the joint distribution of $Q_s U_s, q_v u_v$ equals -4.535 ± 0.444 MJy/sr for the same N_{side}. The line-of-sight extinction in the RoboPol observation area, figure 7.15, show an increase in extinction from around 300 parsec to 400 parsec for the four sightlines. Figure 7.15 shows different structures in the clouds giving the amplitude and distance to cloud. My template estimates a spectral index, $\beta_{217-353} = 1.563 \pm 0.007$.

In this thesis, we have investigated how the ISM affects starlight by looking at the extinction of light in 3D space and polarisation. By comparing extinction with the foreground components of thermal dust and CO line emission, we gained a more profound knowledge on the absorbing properties of the ISM. The investigation of polarisation in a $1.5^\circ \times 1.5^\circ$ area of the sky produced excellent results on the spectral index of a modified blackbody model. It gives an improved understanding of the thermal dust and shows starlight polarisation can map the ISM and thus improve the current thermal dust models.

9.4 Looking into the future

For our results to improve, calculating the differential extinction more robustly and then estimate the cumulative extinction, similar to the method of Green19, will provide more details regarding where new clouds appear. To limit our self to only Gaia extinction estimates, either downgrading the maps from $N_{side} = 128 \rightarrow 16$ or smooth the maps may be used to reduce the noise. Smoothing over distance should be considered as well. Increasing the resolution of the interpolated extinction estimates and find better fits when comparing with dust and CO intensity would give better models.

Since the data Green19 use does not cover the full sky, and other analysis either covers less of the sky or does not go to large enough distances. A possibility to make better extinction maps of the full sky would be to use the extinction estimates of Gaia DR2 and Green19, then model A_G to fit the extinction estimate A_V of Green19 at the three-quarter of the sky covered by Green. Then use the $A_G \rightarrow A_V$ model in the last

quarter of the sky Green19 do not cover. The mapping of extinction and dust distribution is essential to produce precise estimated on optical depth to re-ionisation. Methods to fit $A_G \rightarrow A_V$ could be MCMC sampling or machine learning algorithms.

We need to check the polarisation results for possible biases in future work, both in improved correction for extinction and the possible effect of beam depolarisation. Further, by including the stellar distances in the correlation, looking at stars that are close and stars that are further away individually may give extra constraints on the ISM structure. The next goal within polarisation surveys is to extend the surveys to cover a large part of the sky. Both to map the magnetic field in the galaxy in three dimensions and to improve the foreground models for future CMB analysis. Since Compton scattering can polarise photons, measurements of polarisation is vital to estimate the optical depth to re-ionisation.

When updating the dust models, considering the many properties of the dust grains is essential. Since there is a connection between extinction and polarisation of light because of dust grains shape and alignment in the ISM, future work must combine the knowledge of the two to improve the foreground model of dust. Thus, polarisation and extinction from the ISM are valuable tracers of the magnetic field of the Milky Way.

The sampling routines involved in component separation must be improved to simulate the ISM completely. Ideally, the foreground modelling should consider the ISM distribution in 3D, such that sampling over how much extinction/dust amplitude there is in a particular direction and distance, to see how the light travels through the ISM. Moreover, extend the sampler to consider how the dust polarise the light passing by in the 3D distribution of dust.

The future of the field requires more precise observation and better data analysis, including usage of time-ordered data. The BeyondPlanck program aims to compute the cosmological parameters, angular power spectra and astrophysical component maps within one code using the raw data from observation by applying a single statistically coherent pipeline to analyse CMB data sets. These goals are vital in the quest of detecting primordial gravitational waves and probe the optical depth to re-ionisation. On the instrumental part, the liteBIRD satellite (not launched yet) will provide improved sensitivity, 1.8 μK arcmin (Hazumi et al. 2012), in the microwave regime. In 2021, the Pasiphae project is ready to investigate starlight polarisation on more extensive parts of the sky, giving new information on the polarisation and dust distribution.

Bibliography

1. Andrae R., Fouesneau M., Creevey O., et al. (2018) Gaia Data Release 2, First stellar parameters from Apsis, *Astronomy and Astrophysics*, 615, A8. DOI: https://doi.org/10.1051/0004-6361/201732516

2. Arenou F., Grenon M. and Gómez A. (1992) A tridimensional model of the galactic interstellar extinction. *Astronomy and Astrophysics*, 258, 104-111. https://ui.adsabs.harvard.edu/abs/1992A%26A...258..104A/abstract:

3. Banday A.J., Dickinson C., Davies R.D., Davis R.J. and Górsky K.M. (2003) Reappraising foreground contamination on the COBE-DMR data, *Astronomical Society*, 345, 897-911. http://adsabs.harvard.edu/full/2003MNRAS.345..897B

4. Bennett C.L., Larson D., Weiland J. L. et al. (2013) Nine-Year Wilkinson Microwave Anisotropy Probe (WMAP) Observations: Final Maps and Results, *The Astrophysical Journal*, 208(2), 20B. DOI: 10.1088/0067-0049/208/2/20,

5. Berry M., Ivezić Ž., Sesar B., et al. (2012) The Milky Way Tomography with Sloan Digital Sky Survey. IV. Dissecting Dust, *The Astrophysical Journal*, Vol. 757, Issue 2. DOI: 10.1088/0004-637X/757/2/166

6. Bessell M.S. (2005) Standard Photometric Systems, *Annual Review of Astronomy and Astrophysics*, 43, 293-336. DOI: 10.1146/annurev.astro.41.082801.100251

7. BeyondPlanck Collaboration (In Prep.) Beyond Planck I. Global Bayesian analysis of the Planck Low Frequency Instrument data, *Astronomy and Astrophysics* manuscript.

8. Brown A.G.A., Vallenari A., Prusti T. et al. (2018) Gaia Data release 2, Summary of the contents and survey properties, *Astronomy and Astrophysics*, 616, A1. DOI: https://doi.org/10.1051/0004-6361/201833051

9. Cardelli J.A., Clayton G.C. and Mathis J.S. (1989) The relationship between infrared, optical and ultraviolet extinction *The Astrophysical Journal*, 345, 245-256. http://adsabs.harvard.edu/full/1989ApJ...345..245C

10. Casella G. and Goerge E.I. (1992) Explaining the Gibbs sampler, *The American Statistician*, Vol 46, no3, 167-174. DOI: 10.2307/2685208

11. Chen B.Q., Schultheis M., Jiang B.W., et al. (2013) Three-dimesional interstellar extincion map toward the galactic bulge, *Astronomy and Astrophysics*, 550, A42. DOI: https://doi.org/10.1051/0004-6361/201219682

12. Chen B.Q., Huang Y., Yuan H.B., et al. (2018) Three dimensional interstellar dust reddening maps of the Galactic plane,*Astronomical Society*, 000, 1-13. arXiv:1807.02241v3

13. Clark C., Bianchi S., Bot C., et al. (2020) Unleashing the Potential Fust Emission as a Window onto Galaxy Evolution, *Astro2020 Sience White Paper*, no. 378. arXiv:1903.06810

14. Clarc S.E. and Hensley B.S. (2019) Mapping the Magnetic Interstellar Medium in Three Dimensions Over the Full Sky with Neutral Hydrogen, *American Astronomical Society*, 887, 2. DOI: 10.3847/1538-4357/ab5803

15. Cox D.P. and Anderson P.R. (1982) Extended Adiabatic blast waves and a model of the soft X-ray background, *The Astrophysical Journal*, 253, 268-289. DOI: 10.1086/159632

16. Danielsky C., Babusiaux C., Ruiz-Dern L., Saroretti P. and Arenou F. (2018) The empirical Gaia G-band extinction coefficient, *Astronomy and Astrophysics*, 614, A19. https://doi.org/10.1051/0004-6361/201732327

17. Demyk K., Meny C., Depecker C., et al. (2017) Low temperature MIR to submillimeter mass absorption coefficient of interstellar dust analogues, *Astronomy and Astrophysics*, 606, A50. DOI: https://doi.org/10.1051/0004-6361/201730944

18. de Oliveira-Costa A., Kogut A., Devlin M.J., et al. (1997) Galactic Microwave Emission at degree angular scales, *Astrophysical Journal, Letters*, 482, L17-L20. DOI: 10.1086/310684

19. Draine B.T. and Lazarian A. (1998) Diffuse Galactic emission from Spinning dust grains, *The Astrophysical Journal*, 494, L19–L22. DOI: 10.1086/311167

20. Drimmel R., Cabrera-Lavers A. and López-Corredoira M. (2018) A three-dimensional galactic exinction model, *Astronomy and Astrophysics*, 409, 205-215. DOI: 10.1051/0004-6361:20031070

21. Dhawan S., Brout D., Scolnic D., Goobar A., Riess A.G. and V. Miranda (2020) Cosmological model insensitivity of local H_0 from the Cepheid distance ladder, preprint. arXiv:2001.09260

22. Fialkov A. and Loeb A. (2013) The 21-cm Signal from the cosmological epoch of recombination, *Journal of Cosmology and Astroparticle Physics*, vol.2013. DOI: 10.1088/1475-7516/2013/11/066

23. Fitzpatric E.L. and Massa D. (2007) An Analysis of the shapes of interstellar extinction curves. V. The IR-through-UV curve morphology, *The Astrophysical Journal*, 663, 320-341. DOI: 10.1086/518158

24. Fixen D.J. (2009) The Temperature of the Cosmic Microwave Background, *The Astrophysical Journal*, 707, 916-920. DOI: 10.1088/0004-637x/707/2/916

25. Freedman W.L., Madore B.F., Hatt D., et al. (2019) The Carnegie-Chicago Hubble Program. VIII. An Independent Determination of the Hubble Constant Based on the Tip of the Red Giant Branch, *The Astrophysical Journal*, 882, 34. DOI: 10.3847/1538-4357/ab2f73

26. Freedman W.L., Madore B.F., Hoyt T., et al. (2020) Calibration of the Tip of the Red Giant Branch, *The Astrophysical Journal*, 891, 57. DOI: 10.3847/1538-4357/ab7339

27. Fuskeland U., Wehus I.K., Eriksen H.K., and Næss S.K. (2014) Spatial variations in the spectral index of polarized synchrotron emission in the 9 yr WMAP sky maps, **The Astrophysical Journal**, 790, 104. DOI: http://dx.doi.org/10.1088/0004-637X/790/2/104

28. Gatz D.F. and Smith L. (1995) The standard error of a weighted mean concentration - I. Bootstrapping vs other methods, *Atmospheric Environment*, 29, 11, 1185-1193. https://www.cs.tufts.edu/~nr/cs257/archive/donald-gatz/weighted-standard-error.pdf

29. Geyer C.J. (1992) Practical Markov Chain Monte Carlo, *Statisical Science*, Vol 7, No. 4, 473-511. DOI: 10.1214/ss/1177011137

30. Giovannini, M. (2017) Tensor to scalar ratio from single field magnetigenesis, *Physics Letters B*, 771, 482-486. DOI: https://doi.org/10.1016/j.physletb.2017.05.093

31. Górski K.M., Hivon E., Banday A.J., et al. (2005) HEALPix: A framework for High-resoluton discretization and fast analysis of data distributed on the sphere, *The Astrophysical Journal*, 622:759-771. DOI: 10.1086/427976

32. Górski K.M., Wandelt B.D., Hivon E., Hansen F.K., and Banday A.J. (2010) The HEALPix Primer, *NASA*. https://healpix.jpl.nasa.gov/pdf/intro.pdf

33. Green G.M., Schlafly E.F., Finkbeiner D. et al. Galactic Reddening in 3D from Stellar Photometry - An Improved Map, *Monthly Notices of the Royal Astronomical Society*, 478, 651–666. DOI: https://doi.org/10.1093/mnras/sty10081-17

34. Green G.M., Schlafly E. Zucker C., Speagle J.S. and Finkbeiner D.P. (2019) A 3D Dust map Based on Gaia, Pan-STARRS 1 and 2MASS, *The Astrophysical Journal*, Vol.887. DOI: 10.3847/1538-4357/ab5362

35. Guillet V., Fanciullo L., Verstraete L. et al (2018) Dust models compatible with Planck intensity and polarization data in translucent lines of sight, *Astronomy and Astrophysics*, 610, A16 DOI: 10.1051/0004-6361/201630271

36. Guth A.H. (1981) Inflationary universe: A possible solution to the horizon and flatness problems, *Phys. Rev. D*, vol.23, issue 2, 347–356. DOI: 10.1103/PhysRevD.23.347

37. Guth A.H. (2007) Eternal inflation and its implications, *Journal of Physics A: Mathematical and Theoretical*, 40, 25, 6811-6825. DOI: 10.1088/1751-8113/40/25/s25

38. Hazumi M., Borrill J., Chinone Y., et al. (2012) LiteBIRD: a small satellite for the study of B-mode polarization and inflation from cosmic background radiation detection, *Society of Photo-Optical Instrumentation Engineers (SPIE) Conference Series*, 8442. DOI: 10.1117/12.926743

39. Henslay B.S., Zhang, C. and Bock J.J. (2019) An Imprint of the Galactic Magnetic Field in the Diffuse Unpolarized Dust Emission, *The Astrophysical Journal*, 887 (2). DOI: 10.3847/1538-4357/ab5183

40. Hill A.S., Landecker T.L., Carretti E., Douglas K. and SunX.H. (2017) The Fan Region at 1.5 GHz – I. Polarized synchrotron emission extending beyond the Perseus Arm, *Monthly Notices of the Royal Astronomical Society*, 467, 4, 4631–4646. DOI: http://dx.doi.org/10.1093/mnras/stx389

41. Hinshaw G., Spergel D.N., Verde L., et al (2003) First Year Wilkinson Microwave Anisotropy Probe (WMAP) Observations: The Angular Power Spectrum, *The Astrophysical Journal*, 148, 135–159. DOI: 10.1086/377225

42. Hjort-Jensen M. (2015) *Computational Physics, Lecture Notes Fall 2016*. Oslo: Department of Physics, University of Oslo. Available at https://github.com/CompPhysics/ComputationalPhysics/tree/master/doc/Lectures (Accessed: June 14th 2020)

43. Hutsemékers D. (1998) Evidence of very large scale coherent orientation of quasar polaisation vectors, *Astronomy and Astrophysics*, 332, 410-428. https://ui.adsabs.harvard.edu/abs/1998A&A...332..410H

44. Johnson H.L. and Morgan W.W. (1953) Fundamental stellar photometry for standards of spectral type on the revised system of the Yerkes spectral Atlas *The Astrophysical Journal*, 117 (3), 313-352. DOI: 10.1086/145697

45. Jordi C., Gebran M., Carrasco J.M., et al. (2010) Gaia broad band phometry, *Astronomy and Astrophysics*, 523, A48. DOI: 10.1051/0004-6361/201015441

46. Kamionkowski M., Kosowsky A. and Stebbins A. (1997) Statistics of cosmic microwave background polarization, *The American Physical Society*, Vol.55, num.12, 7368-7388. DOI: https://doi.org/10.1103/PhysRevD.55.7368

47. Kamionkowski M., Kovetz E.D. (2016) The Quest for B modes from Inflationary Gravitational Waves, *Annual Review of Astronomy and Astrophysics*, 54, 227-269. DOI: https://doi.org/10.1146/annurev-astro-081915-023433

48. King O.G., Blinov D., Ramaprakash A.N., et al. (2014) The RoboPol pipeline and control system, *Monthly Notices of the Royal Astronomical Society*, 442, Issue 2, 1706–1717, DOI: https://doi.org/10.1093/mnras/stu176

49. Kogut A., Banday A.J., Bennett C.L. et al. (1996) High-Latitude Galactic Emission in the COBE Differential Microwave Radiometer 2 Year Sky Maps, *The Astrophysical Journal*, 460, 1-9. DOI: 10.1086/176947

50. Krauss L.M., Dodelson S. and Meyer S. (2010) Primordial Gravitational Waves and Cosmology, *Science*, 328(5981), 989-992. DOI: 10.1126/science.1179541

51. Krügel E. (2009) The influence of scattering on the extinction of stars, *Astronomy and Astrophysics*, 493, 385-397. DOI: https://doi.org/10.1051/0004-6361:200809976

52. Ku H.H. (1966) Notes on the use of Propagation of Error Formulas, *Journal of Research of the National Bureau of Standards*, Vol. 70C, No 4, 263-273. https://archive.org/details/jresv70Cn4p263/mode/2up

53. Kutner, M. (2003). Contents of the interstellar medium. In *Astronomy: A Physical Perspective* (pp. 237-262). Cambridge: Cambridge University Press. DOI: 10.1017/CBO9780511802195.018

54. Lallement R., Vergely J.L., Valette B., et al. (2014) 3D maps of the local ISM from inversion of individual color excess measurements, *Astronomy and Astrophysics*, 561, A91. DOI: 10.1051/0004-6361/201322032

55. Lallement R., Capitanio L., Ruiz-Dern L., et al. (2018) Three-dimensional maps of interstellar dust in the local arm using Gaia, 2MASS and APOGEE-DR14, *Astronomy and Astrophysics*, 616, A132. 2018. DOI: https://doi.org/10.1051/0004-6361/201832832

56. Lallement R., Babusiaux C., Vergely J.L., et al. (2019) Gaia-2MASS 3D maps of Galactic interstellar dust within 3kpc, *Astronomy and Astrophysics*, 625, A135. DOI: 10.1051/0004-6361/201834695

57. Leike R.H. and Enßlin T.A. (2019) Charting nearby dust clouds using Gaia data only, *Astronomy and Astrophysics*, 631, A32. DOI: https://doi.org/10.1051/0004-6361/201935093

58. Leinaas J.M. (2019) *Classical Mechanics and Electrodynamics*. Oslo, World Scientific. DOI: 10.1142/11245

59. Leitch E.M., Readhead A.C.S., Pearson T.J. and Myers S.T. (1997) An anomalus component of galactic emission, *The Astrophysical Journal, Letters*, 486(1), L23-L26. DOI: 10.1086/310823

60. Lenz D., Hensley B.S. and Dore O. (2017) A new, Large-scale map of Interstellar Reddening Derived from HI Emission, *The Astrophysical Journal*, Vol. 846(1). DOI: 10.3847/1538-4357/aa84af

61. Luri X., Brown A.G.A., Sarro L.M., et al. (2018) Gaia Data Release 2: Using Gaia parallaxes, *Astronomy and Astrophysics*, 616, A9. DOI: https://doi.org/10.1051/0004-6361/201832964

62. Marrese P.M, Marinoni S., Fabrizio M. and Altavilla G. (2019) Gaia Data Release 2: Cross-match with external catalogues, *Astronomy and Astrophysics*, 621, A144. DOI: https://doi.org/10.1051/0004-6361/201834142

63. Marshall D.J., Robin A.C., Reylé C., Schultheis M. and Picaud S. (2006) Modelling the galactic interstellar extinction distribution in three dimensions, *Astronomy ad Astrophysics*, 453, 635-651. DOI: https://doi.org/10.1051/0004-6361:20053842

64. Martin P.G. (2007) On Prediction the Polaiszation of Low Frequency Emission by Diffuse Interstellar dust, *EAS Publication series*, 23, 165-188. DOI: https://doi.org/10.1051/eas:2007011

65. Panopoulou G.V., Tassis K., Skalidis R., et al. (2018) Demonstration of Magnetic field Tomography with starlight polarisation towards a diffuse sightline of the ISM. 2018, *The Astrophysical Journal*, 872(1), 56. DOI: http://dx.doi.org/10.3847/1538-4357/aafdb2

66. Peebles P.J.E., Schramm D.N., Turner E.L. and R.G. Kron (1994) The Evolution of the Universe, *Scientific American*, 271, 29 - 33. https://www.scientificamerican.com/article/the-evolution-of-the-universe/

67. Riotto A. 2002. Inflation and the Theory of Cosmological Perturbations. *Summer School on Astroparticle Physics and Cosmology*. Available at: https://arxiv.org/pdf/hep-ph/0210162.pdf. (Accessed 06.06.2020).

68. Planck Collaboration I. (2011) The Planck mission, *Astronomy and Astrophysics*, 536, A1. DOI: https://doi.org/10.1051/0004-6361/201116464

69. Planck Collaboration XXIV. (2011) Dust in the diffuse interstellar medium and the Galactic halo *Astronomy and Astrophysics*, 536, A24. DOI: https://doi.org/10.1051/0004-6361/201116485

70. Planck Collaboration IX (2014) HFI spectral response *Astronomy and Astrophysics*, 571, A9. DOI: https://doi.org/10.1051/0004-6361/201321531

71. Planck Collaboration XI (2014) All-Sky model of the thermal dust emission, *Astronomy and Astrophysics*, 571, A11. 2014. DOI: https://doi.org/10.1051/0004-6361/201323195

72. Planck Collaboration XII (2014) Diffuse Component Separation, *Astronomy and Astrophysics*, 571, A12. DOI: https://doi.org/10.1051/0004-6361/201321580

73. Planck Collaboration XIII (2014) Galactic CO emission,*Astronomy and Astrophysics*, 571, A13. DOI: https://doi.org/10.1051/0004-6361/201321553

74. Planck Collaboration X (2016) Diffuse component separation: Foreground maps, *Astronomy and Astrophysics*, 594, A10. DOI: https://doi.org/10.1051/0004-6361/201525967

75. Planck Collaboration XI (2016) CMB power spectra, likelihoods, and robustness of parameters, *Astronomy and Astrophysics*, 594, A11. DOI: https://doi.org/10.1051/0004-6361/201526926

76. Planck Collaboration III (2018) High Frequency Instrument data processing and frequency maps, *Astronomy and Astrophysics*, preprint. arXiv:1807.06207

77. Planck Collaboration VI (2019) Cosmological Parameters, *Astronomy and Astrophysics*, preprint. arXiv:1807.06209

78. Planck Collaboration X (2018) Constraints on inflation, *Astronomy and Astrophysics*, preprint. arXiv:1807.06211

79. Planck Collaboration XI (2018) Polarized dust foregrounds, *Astronomy and Astrophysics*, preprint. DOI: https://doi.org/10.1051/0004-6361/201832618

80. Planck Collaboration XII (2018) Galactic astrophysics using polarized dust emission, *Astronomy and Astrophysics*, preprint. arXiv:1807.06212

81. ESA and the Planck Collaboration (2020) *Planck*. Available at https://www.cosmos.esa.int/web/planck/picture-gallery (Accessed 18.03.2020)

82. ESA and the Planck Collaboration (2019) *Planck*. Available at https://sci.esa.int/web/planck/-/60501-plancks-view-of-the-cosmic-microwave-background (Accessed 18.03.2020)

83. Planck Collaboration Int. XVII (2013) Emission of dust in the diffuse interstellar medium from the fra-infrared to microwave frequencies, *Astronomy and Astrophysics*, 566, A55. DOI: https://doi.org/10.1051/0004-6361/201323270

84. Planck Collaboration Int. XXI (2015) Comparison of polarized thermal dust from Galactic dust at 353 GHz with interstellar polarization in the visible, *Astronomy and Astrophysics*, 576, A106. DOI: https://doi.org/10.1051/0004-6361/201424087

85. Planck Collaboration Int. XXII (2015) Frequency dependence of thermal emission from Galactic dust in intensity and polarization, *Astronomy and Astrophysics*, 576, A107. DOI: https://doi.org/10.1051/0004-6361/201424088

86. Planck Collaboration Int. XLVI (2016) Reduction of large-scale systematic effects in HFI polarisation maps and estimation of th reionization optical depth, *Astronomy and Astrophysics*, 596, A107. DOI: https://doi.org/10.1051/0004-6361/201628890

87. Plaszczynski S., Montier L., Levrier F. and Tristram M. (2014) A novel estimator of the polarization from normally distributed Stokes parameters *Monthly Notices of the Royal Astronomical Society*, 439 (4), 4048-4056. DOI: https://doi.org/10.1093/mnras/stu270

88. Ramaprakash A.N., Rajarshi C.V, Das H.K., et al. (2019) RoboPol: a four-channel optical imaging polarimeter, *Monthly Notices of the Royal Astronomical Society*, Volume 485, Issue 2, p.2355-2366. 2019. DOI: 10.1093/mnras/stz557

89. Rutten R.J. (1988) *Introduction to astrophysical radiative transfer.* 4th edition. The Netherlands: Sterrekundig Instituut Utrecht. https://www.uio.no/studier/emner/matnat/astro/AST4310/h15/undervisningsmateriale/iart.pdf

90. Rybicki G.B. and Lightman A.P. (1979) *Radiative Processes in Astrophysics*, Weinheim, Germany: WILEY-VCH Verlag GmbH 62 Co. KGaA.

91. Cameron Reed B. (1998) The Composite Observational-Theoretical HR diagram *The Royal Astronomical Society of Canada*, 92, 36-37. https://ui.adsabs.harvard.edu/abs/1998JRASC..92...36R

92. Schlafly E.F., Green G., Finkbeiner D.P., et al. (2014) A large cataloge of accurate distances to molecular clouds from PS1 photometry, *The Astrophysical Journal*, 786 (1). DOI: 10.1088/0004-637x/786/1/29

93. Schlalfly E.F., Meisner A.M., Stutz A.M., et al. (2016) The Optical -Infrared extinction curve and its variation in the Milky Way, *The Astrophysical Journal*, 821 (2), DOI: 10.3847/0004-637X/821/2/78

94. Shultheis M., Zasowski G., Allende Prieto C., et al. (2018) Extinction maps towards the Milky Way Bulge: 2D and 3D test with APOGEE, *The Astronomical Journal*, 148(1). DOI: 10.1088/0004-6256/148/1/24

95. Skalidis R. and Pelgrims V. (2019) Local Bubble contribution to the 353 GHz dust polariased emission, *Astronomy and Astrophysics* 631, L11. DOI: https://doi.org/10.1051/0004-6361/201936547

96. Skrutskie M.F., Cutri R.M., Stiening R., et al. (2006) The two Micron All Sky Survey (2MASS) *The Astrophysical Journal*, 131, 1163-1183. DOI: 10.1086/498708

97. Stubbs C.W., Doherty P., Cramer C. Narayan G. and Brown Y.J. (2010) Precise throughput determination of the Pan-STARRS telescope and the Gigapixel Imager using a Calibrated Silicon Photidiode and a Tunable Laser: Initial results, *The Astrophysical Journal Supplement Series*, 191 (2), 376-388. Preprint. DOI: 10.1088/0067-0049/191/2/376

98. Tassis K., Ramaprakash A.N., Readhead A.C.S, et al. (2018) PASIPHAE: A Hight-Galactic-latitude, high-accuracy optopolarimetric survey. Preprint. arXiv:1810.05652

99. Thomessen, H. (2019) *Observing the CMB Sky with GreenPol, SPIDER and Planck*, Ph.D. thesis, University of Oslo.

100. Tonry J.L., Stubbs C.W., Lykke K.R., et al. (2012) The Pan-STARRS1 Photometric System, *The Astrophysical Journal,* Volume 750, Issue 2. DOI: 10.1088/0004-637X/750/2/99

101. Umiltà C., Cardoso J.F., Benabed K. and Le Jeune M. (2019) The CMB angular power spectrum via component separation: a study on Planck data, *Astronomy and Astrophysics*, 624, A67. DOI: 10.1051/0004-6361/201833758

102. van de Schoot R., Kaplan D., Denissen J., et al. (2013) A gentel Introduction to Bayesian Analysis: Applications to Deveolpment Research, *Society for Research in Child Develpment, Inc.*, Vol. 00 (0), 1-19. DOI: https://doi.org/10.1111/cdev.12169

103. Vergely J.L., Freire Ferrero R., Siebert A. and Valette B. (2001) NaI and HI 3D density distribution in the solar neighbourhood, *Astronomy and Astrophysics*, 366, 1016-1034. DOI: https://doi.org/10.1051/0004-6361:20010006

104. Vergely J.L., Valette B., Lallement R. and Raimond S. (2010) Spatial distribution of interstellar dust in the Sun's vicinity, comparing with neutral sodium bearing gas, *Astronomy and Astrophysics*, 518, A31. DOI: https://doi.org/10.1051/0004-6361/200913962

105. Walker M.J. (1954) Matrix Calculus and the Stokes Parameters of Polarized Radiation, *American Journal of Physics*, 22, 170. 1954. DOI: 10.1119/1.1933670

106. Walsh B. (2004) Markov Chain Monte Carlo and Gibbs sampling. *Lecture Notes for EEB 581, version 26*. Available from: http://nitro.biosci.arizona.edu/courses/EEB581-2004/handouts/Gibbs.pdf

107. Wang S. and Chen X. (2019) The Optical to Mid Infrared Extinction Law Based on the APOGEE, gaia DR2, Pan-STARRS 1 SDSS, APASS, 2MASS and WISE surveys, *The Astrophysical Journal*, 877, 116. DOI: 10.3847/1538-4357/ab1c61

108. Weiler M. (2018) Revised Gaia Data Realeas 2 passbands, *Astronomy and Astrophysics*, 617, A138. DOI: https://doi.org/10.1051/0004-6361/201833462

109. Wong K.C., Suyu S.H., Chen G.C. -F. (2020) H0LiCOW XIII. A 2.4% measurement of H_0 from lensed quasars: 5.3σ tension between early and late-Universe probes, *MNRAS*, preprint. arXiv:1907.04869

110. Yuan W., Riess A.G., Macri L.M., Casertano S. and Scolnic D.M. (2019) Consistent Calibration of the Tip of the Red Giant Branch in the Large Magellanic Cloud on the Hubble Space Telescope Photometric System and a Redetermination of the Hubble Constant, *The Astrophysical Journal*, 886, 61. DOI: 10.3847/1538-4357/ab4bc9

111. Zucker C., Schlafly E.F., Speagle J.S., et al. (2018) Mapping distances across the Perseus molecular cloud using CO observations, stellar photometry, and gaia DR2 parallax measurements, *The Astrophysical Journal*, 869, 83. DOI: 10.3847/1538-4357/aae97c

This work made use of programming packages in Python, their citation are listed below. Websites for their documentation are in the listing as well.

1. John D. Hunter. (2007) Matplotlib: A 2D Graphics Environment, *Computing in Science and Engineering*, 9, 90-95. https://matplotlib.org/

2. Robitaille T.P., Tollerud E.J., Perry Greenfield P., et al. (2013) Astropy: A community Python package for astronomy, *Astronomy and Astrophysics*, 558, A33. DOI: https://doi.org/10.1051/0004-6361/201322068, http://www.astropy.org

3. Travis E. Oliphant (2006) *A guide to NumPy*, USA: Trelgol Publishing, https://archive.org/details/NumPyBook/mode/2up, https://docs.scipy.org/doc/numpy/

4. Van Rossum, G. and Drake Jr, F.L., (1995). *Python reference manual*, Centrum voor Wiskunde en Informatica Amsterdam. https://docs.python.org/3/reference/

5. Virtanen P., Gommers R., Oliphant T.E., et al. (2020) SciPy 1.0: Fundamental Algorithms for Scientific Computing in Python, *Nature Methods* 17, 261–272. DOI: https://doi.org/10.1038/s41592-019-0686-2, https://docs.scipy.org/doc/scipy/

Appendix A

Appendix

In this Appendix, we give some background to the additional methods and tools used in making the results. The first part comprises a description of HEALPix. The third part describes unit conversion, used in CMB analysis, and the fourth section describe smoothing.

A.1 HEALPix

In this paragraph, we explain some properties of HEALPix (Hierarchical Equal Area isoLatitude Pixelisation of a 2-sphere), since the maps provided by Planck Collaboration comes in HEALPix coordinates and the pixelisation is easy to handle.

The construction of a HEALPix map is such that the area of each pixel is equal. Further, it is easy to scale up and down the resolution of the maps and to do local operations on the map. The resolution of the map is given by the resolution parameter N_{side} which goes as $\sim 2^n$ for $n = 0, 1, 2, ...$ The connection between the N_{side} and the number of pixel is $N_{pix} = 12 \times N_{side}^2$. Moving up or down a N_{side} gives exactly four times more or fewer pixels. In the HEALPix pixel system, there are two ways of numbering the pixels, Ring and Nested. Ringed ordering structures the pixels such that the pixel-number increase from north to south around each ring of pixels, this ordering is efficient when working with Fourier transformations and spherical harmonics. The Nested pixel ordering, order the pixels into twelve tree structures, one for each base-resolution pixel. This ordering is efficient when dealing with computations with neighbouring pixels (Górski et al. 2005). One thing to note is that spherical coordinates in the pixelisation system in HEALPix starts at the north pole. At the same time, IAU convention stars at the equator, this means the latitude coordinates in HEALPix is $\theta = 90^\circ - \delta$, where θ is the angle from the north pole (latitude in HEALPix coordinates) and δ is the angle from the equator (latitude in IAU). This gives $\theta \in [0, \pi]$ while $\delta \in [-\pi/2, \pi/2]$.

For polarisation, the sign of the Stokes parameter U changes since the HEALPix line-of-sight goes from the observer to the source. While in the

IAU convention, the line-of-sight points from the source to the observer. The calculation of the polarisation angle ψ goes from the south direction instead of the north direction (Górski et al. 2005).

A.2 Unit convertion

In the CMB analysis, there are three primary units in work; K_{CMB} which is nice in plots and figures, K_{RJ} is Rayleigh-Jeans brightness temperature and MJy/sr which give most physical insight. Since different maps might come in different units, smooth conversions between units are necessary. In Planck Collab. IX, 2013 there is a detailed outline of this. We summarise what we have used in the thesis.

In general, a unit conversion coefficient is obtained by the relation,

$$U_{i,j} = \frac{\mathrm{d}X_i}{\mathrm{d}X_j} = \frac{\int \tau(\nu)\frac{\mathrm{d}I_\nu}{\mathrm{d}X_j}d\nu}{\int \tau(\nu)\frac{\mathrm{d}I_\nu}{\mathrm{d}X_i}d\nu}, \tag{A.1}$$

where $\tau(\nu)$ is the spectral transmission achieved from the bandpass spectra, $\frac{\mathrm{d}I_\nu}{\mathrm{d}X_i}$ is the derivative of the intensity regarding temperature in a given unit. For the subscripts (i, j), i represent the new unit and j represent the old unit. To convert from MJy/sr to K_{CMB} we have,

$$U(\mathrm{MJy/sr} \to \mathrm{K_{CMB}}) = \frac{\int \tau(\nu) b'_\nu d\nu}{\int \tau(\nu)(\nu_c/\nu)d\nu} \times 10^{-20} \quad \left[\frac{\mathrm{K_{CMB}}}{\mathrm{MJy/sr}}\right]. \tag{A.2}$$

Here ν_c/ν comes from the fact $\nu \mathrm{d}I_\nu =$ constant, and b'_ν is the derivative of the Planck function evaluated at $T_{CMB} = 2.7255$ K, and is,

$$\begin{aligned} b'_\nu &= \left.\frac{\partial B_\nu(T,\nu)}{\partial T}\right|_{T_{CMB}} \\ &= \left[\frac{2h\nu^3}{c^2(\exp[h\nu/(k_B T)]) - 1)}\right]\left(\frac{\exp[h\nu/(k_B T)]}{\exp[h\nu/(k_B T)] - 1}\right) \\ &\times \left(\frac{h\nu}{k_B T^2}\right)\Bigg|_{T_{CMB}} \quad \left[\frac{\mathrm{W}}{\mathrm{m^2 srHzK}}\right]. \end{aligned} \tag{A.3}$$

To convert from $K_{RJ} \to K_{CMB}$ the unit conversion coefficient is

$$U(\mathrm{K_{RJ}} \to \mathrm{K_{CMB}}) = \frac{\int \tau(\nu)(2\nu^2 k_B/c^2)d\nu}{\int \tau(\nu) b'_\nu d\nu} \quad \left[\frac{\mathrm{K_{CMB}}}{\mathrm{K_{RJ}}}\right]. \tag{A.4}$$

Further, in table 5-7 in PlanckCollab. IX, 2013 lists different unit conversion factors for different frequency bands. Table A.1 lists our calculated unit conversion factors from $\mathrm{K_{CMB}}$ and MJy/sr to $^-\mathrm{K_{RJ}}$.

A.3 Smoothing of maps

A way of reducing noise in data is to apply smoothing. Healpy[1] provides a smoothing-function for full-sky maps (Górski et al. 2005). The full-sky

[1] Healpy is the HEALPix Python package.

Table A.1: Conversion of units from K_{CMB} and MJy/sr to μK_{RJ} based on the passband of Planck.

frequency [GHz]	$K_{CMB} \rightarrow \mu K_{RJ}$	MJy/sr $\rightarrow \mu K_{RJ}$
30	0.9782324×10^6	
44	0.9505684×10^6	
70	0.8758034×10^6	
100	0.6260411×10^6	
143	0.3221962×10^6	
217	0.1642173×10^6	
353	0.0235809×10^6	
545		$5.1131054 \times 10^{15} \times 10^{-20} \times 10^6$
857		$3.2019239 \times 10^{15} \times 10^{-20} \times 10^6$

maps are in spherical harmonics. The smoothing resolution, r, is the full width half maximum, $FWHM$,

$$FWHM = \frac{\sqrt{r^2 - r_{beam}^2}}{60}, \tag{A.5}$$

where $r_{beam} = 5$ arc-minutes is the resolution of the beam in arc-minutes for high frequencies defined by the instruments on Planck (Planck Collab. I, 2011), the division by 60 is to get degrees. Further, we convert the $FWHM$ to radians. We apply another smoothing-function for the stellar polarisation maps, these maps are in real-space from the stellar positions. For the smoothed value in pixel p, we have,

$$m(p) = \frac{\sum_i^{N_{points}} m_i \exp\left\{-\frac{x_i^2}{2s^2}\right\}}{\exp\left\{-\frac{x_i^2}{2s^2}\right\}}, \tag{A.6}$$

where s and x_i given as,

$$s = \frac{r}{60}\frac{1}{\sqrt{8\ln 2}}, \tag{A.7}$$

$$x_i = \sqrt{(\phi_i - \phi)^2 + (\theta_i - \theta)^2}, \tag{A.8}$$

r is the smoothing resolution in arc-minutes, such that s gives the $FWHM$ smoothing. x_i is the angular distance between pixel i, with coordinates $\{\phi_i, \theta_i\}$, and the other pixels, with ϕ and θ as the longitude and latitude coordinates of the other pixels.